UNIVERSITY OF OKLAHOMA

GRADUATE COLLEGE

USING A LOW-ORDER MODEL TO DETECT AND CHARACTERIZE INTENSE VORTICES IN MULTIPLE-DOPPLER RADAR DATA

A DISSERTATION

SUBMITTED TO THE GRADUATE FACULTY

in partial fulfillment of the requirements for the

Degree of

DOCTOR OF PHILOSOPHY

By

COREY KEITH POTVIN
Norman, Oklahoma
2010

Downloaded from SHAREOK. Persistent Handle URL: https://hdl.handle.net/11244/319004

USING A LOW-ORDER MODEL TO DETECT AND CHARACTERIZE INTENSE VORTICES IN MULTIPLE-DOPPLER RADAR DATA

A DISSERTATION APPROVED FOR THE
SCHOOL OF METEOROLOGY

BY

_____
Dr. Alan Shapiro, Chair

_____
Dr. Ming Xue

_____
Dr. Tian-You Yu

_____
Dr. Evgeni Fedorovich

_____
Dr. John Albert

© Copyright by COREY KEITH POTVIN 2010
All Rights Reserved.

ACKNOWLEDGMENTS

My decision to pursue a graduate degree was largely inspired by my wife, Jacquelyn, who has been very patient during the last six years, and by my participation in the 2003 National Weather Center Research Experiences for Undergraduates (REU) program, which confirmed my interest in formal scientific investigation and writing. I am deeply grateful to my advisor, Alan Shapiro, for his exceptional guidance and friendship throughout both my M.S. and Ph.D. studies. I also appreciate the time and effort invested by the other members of my Ph.D. committee: Tian-You Yu, Ming Xue, Evgeni Fedorovich, and John Albert. Finally, I'd like to thank my family for their enduring encouragement and support, and my friends and colleagues for all the laughter and stimulating discussions.

Table of Contents

List of Tables viii

List of Figures x

Abstract xiv

Chapter 1: Introduction 1

1.1 Background and Motivation 1

1.2 Previous Wind Retrieval Techniques 6

1.2.1 Traditional single-Doppler analysis 6

1.2.2 Traditional dual-Doppler analysis 8

1.2.3 Advection correction techniques 11

1.2.4 Variational methods 13

1.2.5 Vortex detection and characterization techniques 16

1.3 Overview of New Technique 19

Chapter 2: Description of Technique 23

2.1 Low-Order Model 23

2.2 Cost Function Computation and Minimization 26

2.3 Selection of Analysis Domains 28

2.4 Retrieval Procedure 31

2.5 Detection Criteria 33

Chapter 3: Observing System Simulation Experiments 37

3.1 Radar Emulation 37

3.2 ARPS Simulation 39

3.3 Radar Scanning Strategy 43

3.4 First Guess Parameter Values 44

3.5 Analytical Experiment Results 45

3.5.1 Sensitivity to first guess vortex center 45

3.5.2 Sensitivity to observational error 47

3.5.3 Vortex parameter non-uniqueness 47
3.5.4 Broadscale translation parameter non-uniqueness 48
3.5.5 Vortex translation parameter non-uniqueness 49
3.6 ARPS Experiment Results 51
3.6.1 Retrieval results 51
3.6.2 Sensitivity to sampling strategy 58
3.6.3 Application of detection criteria 60
3.7 Summary of OSSE Results 63
Chapter 4: Experiments with Real Radar Data 65
4.1 WSR-88D/TDWR Observations of 8 May 2003 OKC Tornado 65
4.1.1 Description of dataset 65
4.1.2 Experimental Details 66
4.1.3 Retrieval Results 68
4.2 SMART Radar Observations of 29 May 2004 Geary, OK Tornado 70
4.2.1 Description of Dataset 70
4.2.2 Retrieval Results 72
4.3 DOW Observations of 5 June 2001 Attica, KS Tornado 82
4.3.1 Description of Dataset 82
4.3.2 Retrieval Results 82
4.4 IP-1 Observations of 10 February 2009 Low-Level Mesocyclone 94
4.4.1 Description of dataset 94
4.4.2 Retrieval results 95
4.4.3 Discussion 105
4.5 IP-1 Observations of 14 May 2009 Anadarko, OK Tornado 107
4.5.1 Description of dataset 107
4.5.2 Retrieval results 110
4.5.3 Discussion 112

4.6 Retrieving Larger-Scale Vortices 117
4.6.1 Mesocyclone retrieval methodology 117
4.6.2 Dual-Doppler Retrievals 118
4.6.3 Single-Doppler Retrievals 127
4.6.4 Discussion 134
4.7 Sensitivity to First Guess Parameter Values 135
4.8 Summary of Real Data Experiments 140
Chapter 5: Real-Time Implementation in CASA Radar Networks 143
5.1 Optimizing POD, FAR and Computational Time 143
5.2 Role in Adaptive Scanning 146
5.3 Vortex Translation Estimation 147
5.4 Velocity Contamination and Aliasing 149
Chapter 6: Summary and Conclusions 150
References 152
Appendix: Derivation of Low-Order Model 159

LIST OF TABLES

Table 1.1. CASA radar and radome specifications for IP-1 (Brotzge et al. 2010). 5

Table 2.1. Description of low-order model parameters. 25

Table 3.1. True values of low-order model parameters used in analytical retrievals, and the retrieved values from a set of eight retrievals (EXP1) and one single retrieval (EXP2). 38

Table 3.2. Experiments with different sampling strategies. Each experiment set consists of 14 experiments corresponding to different start times. 58

Table 3.3. Number of tornado detections (out of nine retrievals) made in each of the ARPS experiments. 62

Table 4.1. Selected characteristics of the KOKC and KTLX radars..... 66

Table 4.2. Number of tornado detections (out of nine retrievals) made in each of the 8 May 2003 experiments..... 68

Table 4.3. Means of retrieved vortex characteristics for each set of 29 May 2004 retrievals from SMART-Radar data. Sample sizes (n) are given below each time. 73

Table 4.4. Standard deviations of retrieved vortex characteristics for each set of 29 May 2004 retrievals from SMART-Radar data. Asterisked values indicate standard deviations that have been recomputed upon removing an extreme outlier. 74

Table 4.5. Means of retrieved tornado characteristics for selected sets of 5 June 2001 retrievals from DOW radar data. Sample sizes (n) are given below each time. 85

Table 4.6. Standard deviations of retrieved tornado characteristics for selected sets of 5 June 2001 retrievals from DOW radar data. Sample sizes (n) are given below each time. 85

Table 4.7. Means of retrieved tornado characteristics for 5 June 2001 0035 Z retrievals at three different heights. Sample sizes (n) are given below each time. 86

Table 4.8. Means and standard deviations of retrieved LLM characteristics for 2107 Z 10 February 2009 retrievals from CASA IP-1 data. 96

Table 4.9. Means and standard deviations of retrieved LLM characteristics for 2110 Z 10 February 2009 retrievals from CASA IP-1 data (spurious velocities filtered). 98

Table 4.10. Mean retrieved tornado characteristics for three sets of 14 May 2009 retrievals from CASA IP-1 data. 111

Table 4.11. Standard deviations of retrieved tornado characteristics for three sets of 14 May 2009 retrievals from CASA IP-1 data. 112

Table 4.12. Mean retrieved mesocyclone characteristics for three sets of 14 May 2009 mesocyclone-mode retrievals from CASA IP-1 data..... 120

Table 4.13. Mean retrieved tornado characteristics for five sets of 29 May 2004 mesocyclone-mode retrievals from SMART-Radar data. 120

Table 4.14. Same as Table 4.13 except for retrievals using data from SR1 only. 128

Table 4.15. Same as Table 4.13 except for retrievals using data from SR2 only. 128

Table 4.16. Same as Table 4.12 except for retrievals using only data from KCYR. 129

Table 4.17. Same as Table 4.12 except for retrievals using only data from KSAO. 130

Table 4.18. Sets of first guess parameter values used in sensitivity tests with 5 June 2001 dual-DOW dataset. Broadscale parameter first guesses were modified in tests BS1 and BS2; vortex parameter first guesses were modified in tests V1, V2, V3 and V4; and both broadscale and vortex parameter first guesses were modified in tests BSV1 and BSV2. Asterisks denote values that are unchanged from their default values. 138

Table 4.19. Means of retrieved vortex characteristics for 0028 Z experiments using different sets of first guess model parameter values. Sample sizes (n) are given below each time. Italicized rows indicate groups of retrievals in which the non-tornadic vortex was retrieved. 139

Table 4.20. Means of retrieved vortex characteristics for 0031 Z first guess experiments using halved scaling factors for the vortex center parameters. Sample sizes (n) are given below each time. 140

LIST OF FIGURES

Figure 1.1. WSR-88D coverage at 1 km AGL (Maddox et al. 2002). 2

Figure 1.2. POD (left) and FAR (right) for tornado warnings issued within a tornado watch (red), severe thunderstorm watch (blue) or outside of a watch (black). From Keene et al. (2009). 3

Figure 1.3. CASA radar testbed (IP-1) domain. 5

Figure 2.1. Schematic illustrating the procedure for selecting the wind retrieval domains. The algorithm searches for regions within the multiple-Doppler radar domain that satisfy prescribed radial velocity and (optionally) reflectivity criteria. Within each identified region, retrievals are performed over a grid of circular domains whose centers serve as the first guesses for the vortex location(s). 31

Figure 2.2. Tangential velocity profiles for two very different MCRVs. The black dots represent the centers of hypothetical radar probe volumes separated in space by 200 m. Since radar moments are weighted probe-volume averages, these two vortices would appear much more similar in the level-II radial velocity data. 34

Figure 2.3. Verification of n, R_n. 36

Figure 3.1. ARPS reflectivity field (dBZ) at z = 108 m AGL and t = 290 s. 42

Figure 3.2. Horizontal wind field in and around ARPS-simulated tornado at z = 108 m and t = 290 s. Only vectors at every fourth grid point are displayed. 42

Figure 3.3. Radar-vortex geometry and analysis domain. 44

Figure 3.4. Plot of $J(x_0, y_0)$ with remaining model parameters set equal to their first guesses. Contour units are 10^6 m^2 s^{-2}. 46

Figure 3.5. $J(u_b, v_b)$ with perfect first guess for remaining parameters. 48

Figure 3.6. $J(u_v, v_v)$ (10^6 m^2 s^{-2}) for an analytical vortex with true (u_v, v_v) = (10, 10) m s^{-1}. Remaining parameters are set to their true values. 50

Figure 3.7. ARPS (left) and selected retrieved (right) wind field at t = 110 s. Plot circumscribes analysis domain used for this retrieval. Only every fourth vector plotted for readability. 55

Figure 3.8. Emulated radial velocity observations input to retrieval algorithm for retrieval domain shown in Fig. 3.7. (left) V_r from radar at x = -15 km, y= -15 km; (right) V_r from radar at x = 25 km, y = -15 km. 55

Figure 3.9. As in Fig. 3.7 but for the period from 200s to 260 s. 56

Figure 3.10. As in Fig. 3.7 but for a different FG vortex center. 56

Figure 3.11. Illustration of two-step retrieval procedure, valid at t = 410 s: (a) ARPS wind field, (b) retrieved broadscale flow, (c) the vector difference (a)-(b), and (d) total retrieved flow. 57

Figure 3.12. ARPS-estimated tornado path (solid) and retrieved vortex path (dotted) for the period from 170 s to 500 s. 62

Figure 4.1. Location of the 8 May 2003 tornado damage path (F0+) relative to KTLX and KOKC. Dots indicate the tornado locations retrieved by the technique. 69

Figure 4.2. KTLX (top panels) and KOKC (bottom panels) observed (left panels) vs. retrieved (right panels) radial velocities. 70

Figure 4.3. Clockwise from top left: observed, residual (observed minus retrieved broadscale), retrieved vortex, and retrieved total radial velocity fields at 0022 Z for (a) SR1 and (b) SR2. The axes indicate x- and y-displacements from the radar. 77

Figure 4.4. Same as Fig. 4.3 except at 0027 Z. 78

Figure 4.5. Same as Fig. 4.3 except at 0033 Z. 79

Figure 4.6. Same as Fig. 4.3 except at 0038 Z. 80

Figure 4.7. Same as Fig. 4.3 except at 0052 Z. 81

Figure 4.8. Clockwise from top left: observed, residual (observed minus retrieved broadscale), retrieved vortex, and retrieved total radial velocity fields at 0028 Z for DOW radars located (a) east and (b) north-northeast of the analysis domain. The axes indicate x- and y-displacements from the radar. 87

Figure 4.9. Same as Fig. 4.8 except for a different FG vortex center. 88

Figure 4.10. Same as Fig. 4.8 except at 0031 Z. 89

Figure 4.11. Same as Fig. 4.8 except at 0032 Z. 90

Figure 4.12. Clockwise from top left: observed, residual (observed minus retrieved broadscale), retrieved vortex, and retrieved total radial velocity fields at 0035 Z for DOW

radars located (a) east and (b) north-northeast of the analysis domain. The axes indicate *x*- and *y*-displacements from the radar. Elevation angles of (a) 1.4° and (b) 0.5° used... 91

Figure 4.13. Same as Fig. 4.12 except using elevation angles of (a) 4.1° and (b) 1.3°. . 92

Figure 4.14. Same as Fig. 4.12 except using elevation angles of (a) 7.5° and (b) 2.0°. . 93

Figure 4.15. (left) Composite reflectivity field within KCYR-KSAO domain at 2107 Z, and (right) zoomed-in view valid at same time over region outlined by white box in top panel with overlaid dual-Doppler analysis (courtesy of V. Chandrasekar). 95

Figure 4.16. Clockwise from top left: observed, residual (observed minus retrieved broadscale), retrieved vortex, and retrieved total radial velocity fields for the retrieval closest to the ensemble mean at 2107 Z for (a) KCYR and (b) KSAO. The axes indicate x- and y-displacements from the radar..... 100

Figure 4.17. Same as Fig. 4.16 except for a spurious retrieval at 2110 Z..... 101

Figure 4.18. Same as Fig. 4.16 except for a retrieval of a weak vortex at 2111 Z. 102

Figure 4.19. Same as Fig. 4.17 but after filtering spurious velocities. 103

Figure 4.20. Same as Fig. 4.19 but for a false vortex detection..... 104

Figure 4.21. Observed KCYR radial velocity field at 2111 Z. 105

Figure 4.22. KSAO edited radial velocity (top) and reflectivity (bottom) at 0232 Z. .. 109

Figure 4.23 KSAO unedited radial velocity at 0232 Z. 110

Figure 4.24. Clockwise from top left: observed, residual (observed minus retrieved broadscale), retrieved vortex, and retrieved total radial velocity fields for the retrieval closest to the ensemble mean at 0232 Z for (a) KCYR and (b) KSAO. The axes indicate x- and y-displacements from the radar..... 114

Figure 4.25. Same as Fig. 4.24 except at 0233 Z. 115

Figure 4.26. Same as Fig. 4.24 except at 0234 Z. 116

Figure 4.27. Same as Fig. 4.24 except for mesocyclone-mode retrievals..... 121

Figure 4.28. Same as Fig. 4.27 except at 0233 Z. 122

Figure 4.29. Same as Fig. 4.27 except at 0234 Z. 123

Figure 4.30. Same as Fig. 4.4 except for mesocyclone-mode retrievals..... 124

Figure 4.31. Same as Fig. 4.30 except at 0038 Z. 125

Figure 4.32. Same as Fig. 4.30 except at 0052 Z. 126

Figure 4.33. Unsuccessful 0022 Z 29 May 2004 mesocyclone-mode retrieval using data from SR2 only. 130

Figure 4.34. Same as Fig. 4.30 but for retrievals using data from SR1 only. 131

Figure 4.35. Same as Fig. 4.31 but for retrievals using data from SR1 only. 131

Figure 4.36. Same as Fig. 4.32 but for retrievals using data from SR1 only. 132

Figure 4.37. Same as Fig. 4.27 but for retrievals using data from KSAO only. 132

Figure 4.38. Same as Fig. 4.28 but for retrievals using data from KSAO only. 133

Figure 4.39. Same as Fig. 4.29 but for retrievals using data from KSAO only. 133

Figure 5.1. Depiction of one possible set of relationships between the vortex detection algorithm and the rest of the MCC. 147

Figure A.1. Cartesian and cylindrical (vortex) coordinate systems defining model broadscale and vortex flows, respectively at $t = 0$. The vortex is initially located at x_0, y_0. 162

ABSTRACT

A new multiple-Doppler radar analysis technique is presented for the objective detection and characterization of intense vortices. The technique consists of fitting radial wind data from two or more radars to a simple analytical model of a vortex and its near-environment. The model combines a uniform flow, linear shear flow, linear divergence flow (all of which comprise a broadscale flow), and modified combined Rankine vortex. The vortex and its environment are allowed to translate. A cost-function accounting for the discrepancy between the model and observed radial winds is evaluated over space and time so that observations can be used at the actual times and locations they were acquired. The parameters in the low-order model are determined by minimizing this cost function.

The development of the method is initially guided by emulated radial velocity observations of analytical vortices. A high-resolution Advanced Regional Prediction System (ARPS) simulation of a supercellular tornado is then used to generate more realistic pseudo-observations. Finally, the technique is tested using real dual-Doppler tornado and mesocyclone observations from a variety of radar platforms including Weather Surveillance Radar - 1988 Doppler (WSR-88D), Terminal Doppler Weather Radar (TDWR), Shared Mobile Atmospheric Research and Teaching Radar (SMART-R), and Doppler on Wheels (DOW). The technique shows skill in detecting intense vortices and, when the vortex is well-resolved, in retrieving key model parameters including vortex location, translational velocity, radius and maximum tangential wind speed. In cases where the vortex is not well-resolved, additional vortex characteristics computed

from the retrieved model parameters and verified against radial velocity observations can still provide useful information about vortex size and strength.

CHAPTER 1: INTRODUCTION

1.1 Background and Motivation

Tornadoes and other severe thunderstorm hazards (defined by the U.S. National Weather Service as hail 1" or greater in diameter or straight-line winds of 58 miles per hour or greater; NOAA 2010) pose serious risks to life and property throughout the United States. Annual tornado deaths in the U.S. averaged 49 over the period 1994-2003 (NOAA 2006), and yearly damages often reach into the hundreds of millions of dollars. Annual hail damages average nearly one billion dollars. Consequently, the development of robust techniques to detect mesocyclones (more than 90 % of which produce severe weather; Stumpf et al. 1998) and tornadoes in real-time is a major focus of severe weather research for operational applications in the U.S. Several factors limit the success of such techniques. A significant portion of the lower troposphere, within which tornadoes and low-level mesocyclones occur, is unobserved by the current Weather Surveillance Radar- 1988 Doppler (WSR-88D) network (Maddox et al. 2002; Fig. 1.1). This lack of coverage is primarily due to the large spacing, about 230 km, between radars and the increase of radar beam height above ground with range due to both the non-zero beam elevation and earth curvature. The resulting nearly complete lack of overlapping operational radar coverage at low levels hinders the application of multiple-Doppler data analysis techniques. The degradation of azimuthal resolution with distance from the radar limits our ability to observe fine-scale features of significant circulations that do occur within the WSR-88D domain. Finally, the kinematic structure of intense

atmospheric vortices and their surrounding flow is often highly complex and variable from case to case, making it difficult to devise robust detection criteria.



Figure 1.1. WSR-88D coverage at 1 km AGL (Maddox et al. 2002).

Due to the above limitations to the current operational radar network, forecasters are often forced to make tornado warning decisions in the absence of low-level, high-resolution radial velocity data. As a result, a high probability of detection (POD) necessarily comes at the expense of a high false alarm rate (FAR). Moreover, National Weather Service POD and FAR scores have reached a plateau in recent years and thus appear to be near their optimal values for the current national radar network (Fig. 1.2). Without increases in low-level radar coverage and/or observational resolution, it is unlikely that radar-based tornado warnings will significantly improve.

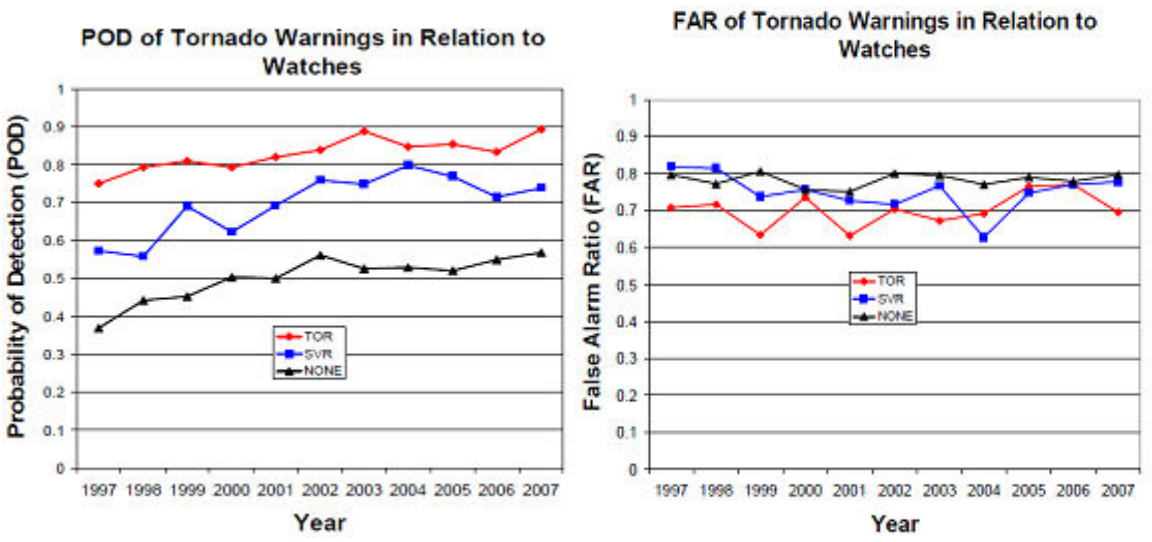

Figure 1.2. POD (left) and FAR (right) for tornado warnings issued within a tornado watch (red), severe thunderstorm watch (blue) or outside of a watch (black). From Keene et al. (2009).

This realization has served as one of the major impetuses for a relatively new paradigm in operational radar systems: networks of low-cost, gap-filling radars which are densely-spaced in order to maximize low-level (overlapping) coverage and observational resolution. In 2003, the National Science Foundation founded the Collaborative Adaptive Sensing of the Atmosphere (CASA; McLaughlin et al. 2009) Engineering Research Center. Since then, a test bed of four CASA radars named IP-1 (Integrated Project One; Brotzge et al. 2010, Junyent et al. 2010) has been deployed in Oklahoma (Fig. 1.3; Table 1.1). These X-band radars are spaced ~25 km apart and are designed to adaptively scan the atmosphere based on user needs and priorities as well as radar-detected meteorological features such as thunderstorms and regions of rotation. The dynamic scanning strategy combined with rapid rotation rates (typically ~24° s^{-1}) increases the temporal resolution with which significant weather features can be observed. The range resolution (~100 m) is also significantly improved over the WSR-

88D network. The half-power beamwidth (1.8°) is wider than that of the WSR-88D network, however, this is more than compensated by azimuthal oversampling (0.5° or 1.0°) and the proximity of the radars to each other. Finally, CASA-like networks provide a large amount of low-level multiple-Doppler coverage. All of these features make CASA-like radar networks well-suited to filling near-surface gaps in existing networks. Densely-spaced X-band radar networks are now also operating in Japan (Maesaka et al. 2007), Denmark (Pedersen et al. 2007) and France (Diss et al. 2009). As regional high-resolution, multiple-Doppler networks become more common, it will be increasingly important to develop wind retrieval and detection techniques that utilize the extra velocity information provided by such networks. In addition, as the volume of meteorological data available to forecasters in realtime continues to increase, so too will the need for automated detection algorithms that help forecasters to identify supercellular and tornadic thunderstorms, particularly when situational awareness is low (Brotzge and Erickson 2010) or during severe weather outbreaks.

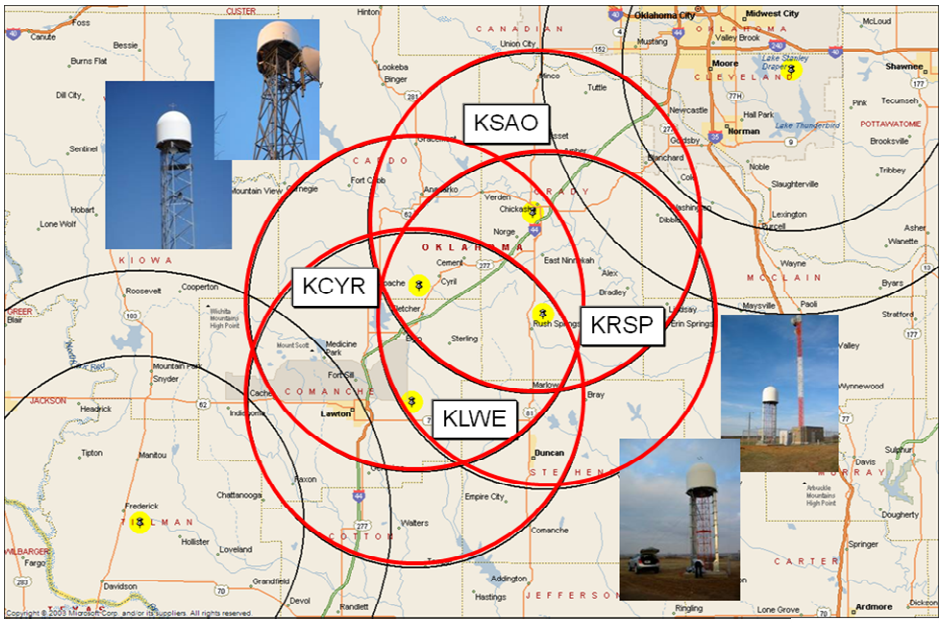

Figure 1.3. CASA radar testbed (IP-1) domain.

	CASA	WSR-88D
Frequency	X band (9.41 GHz)	S band (2.9 GHz)
Peak power output	25 kW	750 kW
3-dB beamwidth	1.8°	0.92°
Antenna diameter	1.2 m (4 ft)	8.5 m (28 ft)
Dual polarization	Yes	No
Clutter suppression	Real-time Gaussian model adaptive processing (GMAP)	GMAP
Ambiguity mitigation	Yes	Staggered pulse repetition time (PRT) upgrade planned for 2011
Range	30 km	460 km for reflectivity; 230 km for velocity, spectrum width
Range sampling	100 m	250 m
Data spacing	1° azimuth *x*	1.0° azimuth *x*
	1° elevation *x*	0.5° elevation *x*
	100 m × 60 s	250 m × 300 s (in 2007)
3-dB sample volume (m)	471 × 471 × 100 at 15-km range	1847 × 1847 × 250 at 115-km range
Domain with low-level radar coverage (%)*		
At 500 m	100	15
At 1 km	100	40
At 2 km	100	100

* Radar coverage percentages were estimated assuming an idealized network of radars with no terrain. A radar spacing of 35 km was assumed for CASA and a radar spacing of 225 km spacing for the WSR-88D (Brotzge et al. 2009).

Table 1.1. CASA radar and radome specifications for IP-1 (Brotzge et al. 2010).

1.2 Previous Wind Retrieval Techniques

A variety of techniques have been developed to retrieve kinematic, dynamic and thermodynamic properties of the atmosphere using data from one or more Doppler radars. These techniques have been used to study a range of weather phenomena ranging from slowly-varying flows in clear air to thunderstorms to tropical cyclones. Many of these methods make use of data from a single Doppler radar, while others combine information from two or more Doppler radars with overlapping domains. Brief descriptions of these techniques as well as important results of studies which have used these procedures are discussed herein.

1.2.1 Traditional single-Doppler analysis

Single-Doppler wind retrieval techniques have been developed to contend with the large regions of non-overlapping radar domain in the current WSR-88D network as well as radar networks in other countries. The simplest single-Doppler retrieval techniques assume a linear spatial model for the velocity field. Regression analysis is then used to produce the best fit between the model parameters and the observed radial wind field.

The first linear model method to be proposed was the velocity-azimuth display (VAD) technique (Lhermitte and Atlas 1962). This method was initially used to retrieve the mean horizontal wind velocity from radial wind data around horizontal circles centered on the radar. It was later modified to retrieve other parameters such as stretching and shearing deformation and convergence (Caton 1963; Browning and Wexler 1968).

Caya and Zawadzki (1992) demonstrated that VAD analysis parameters have little physical meaning for cases where the observed wind field deviates significantly from the linear model. They therefore proposed a nonlinear VAD model which simultaneously uses data from an entire volume scan. This approach, however, is limited to a specific class of non-linearities.

Easterbrook (1975) explored the advantages of fitting data to a linear model over a conical sector as opposed to along a circle (as in the original VAD technique). This approach was successful in extracting additional information about the wind field, but was still sensitive to vertical motions, wind shear and non-linear flow. Waldteufel and Corbin (1979) extended this idea to a volume of data. Their method, Volume Velocity Processing (VVP), simultaneously processes data from multiple conical radar scans. These scans should therefore occur over a small enough time period such that the observed wind field is approximately steady state. It is also assumed that horizontal gradients of vertical velocity are much smaller than vertical gradients of horizontal wind. The radial wind data is fit to the linear flow model using a least squares procedure.

VVP offers a number of advantages over its predecessors. It allows the divergence terms and therefore vertical velocity (computed by integrating the continuity equation) to be completely recovered. Since vertical velocity can be retrieved, higher radar elevation angles can be used. Retrieval of the vertical derivatives of the three velocity components provides a means for checking the validity of the required assumption that the horizontal winds vary linearly in the horizontal plane. VVP is also less sensitive to small-scale irregularities in the wind field.

A major limitation of the VVP method is that aliasing between retrieved wind parameters can occur if the size of the analysis sub-volume (extent in range, azimuth or elevation angle) is too small. This is because discrimination between parameters is dependent upon their variation with the radar viewing angle. This effect increases as the independent variables in the VVP regression become more collinear due, for example, to large gaps in data coverage or the neglect of important wind parameters in the model (Boccippio 1995). Another limitation of the method is the inability to directly retrieve vertical vorticity (although it can be inferred indirectly by considering wind estimates on different sectors).

Caya et al. (2002) extended the VVP procedure to include anelastic mass conservation as well as translation of the model wind field. The latter addition allows for the vorticity and thus the full linear wind field to be retrieved. This method also produces better flow retrievals since the wind field can be observed from different viewing angles with time.

1.2.2 Traditional dual-Doppler analysis

Dual-Doppler retrieval techniques take advantage of the additional information gained by sampling a wind field from multiple radar perspectives. The mass conservation equation is often applied as a weak or strong constraint. Dual-Doppler analyses are generally more reliable than single-Doppler methods, studies of which often use dual-Doppler analyzed winds for ground truth. Dual-Doppler wind analyses have proven vital in progressing our understanding of and ability to model the boundary layer and severe convection (Shapiro and Mewes 1999).

Modern day dual-Doppler analysis began with Armijo's (1969) derivation of the unique solution for a velocity field exactly satisfying the anelastic mass conservation equation (strong constraint) as well as the radial winds observed by two or three Doppler radars. The Armijo (1969) technique is generally not directly applied in practice for two major reasons. First, the integrand for the PDE for *w* is a quasi-horizontal mass flux divergence, and so biased errors in the divergence field can accumulate during the integration and lead to serious errors in the vertical velocity solution. Second, errors in the boundary condition(s) for *w* are often large (since the bottom of the dual-Doppler domain is typically well above the ground) and so can also significantly contaminate the vertical velocity retrieval. Early dual-Doppler investigations sought to mitigate these two problems.

In order to address the first problem, O'Brien (1970) introduced a technique in which provisional horizontal divergence estimates are variationally adjusted to exactly satisfy anelastic mass conservation and vertical velocity boundary conditions at the top and bottom of the domain. This method produced more physically-realistic estimates of w throughout the domain than when no corrections were applied to the divergence field. Ray et al. (1975) smoothed the quasi-horizontal wind field prior to integrating for *w* in order to reduce biased errors in the divergence field. Many other studies have used downward (rather than upward) integration of the mass continuity equation to obtain *w* since this results in horizontal divergence errors being distributed to lower levels, where the feedback between errors in w and horizontal divergence is weaker. However, this may not be a desirable approach if the wind field at lower levels is of greatest interest or if no reliable upper boundary condition on *w* is available.

A common ad hoc approach to the second (boundary condition) problem is to assume $w = 0$ at the ground and that the horizontal divergence below the lowest radial wind data level is some fraction of the divergence at the lowest data level (e.g. Brandes 1977). Chong and Testud (1983) used a variational technique to adjust an initial boundary condition on w at the ground such that the mean vertical velocity there is zero and the "mathematical regularity" of the vertical velocity field is maximized. This method was found to produce similar errors to the downward integration approach but with the advantage that a quasi-realistic boundary condition on w at the ground is preserved. In Mewes and Shapiro (2002), the anelastic vertical vorticity and mass conservation equations are used as weak constraints to derive a pair of coupled equations for the vertical velocity boundary conditions w_{top} and w_{bottom}. Using this method, a set of dual-Doppler estimates for u, v and w and the provisional boundary condition $w_{top} = 0$ can be used to solve for w_{bottom}, which in turn can be used to update the solution for w_{top}, and so on until convergence.

Dual-Doppler techniques have proven to be extremely useful tools for studying the evolution of air motions within severe thunderstorms. Ray et al. (1975) used dual-Doppler wind retrievals to identify major circulations and updrafts within a tornadic storm. Ray et al. (1981), using reflectivity and retrieved wind fields for several tornadic supercells, was able to describe the typical evolution of the updrafts, downdrafts, gust fronts, and reflectivity structures (such as the hook echo and weak echo region) within such storms. Brandes (1981) used dual-Doppler observations to construct the three-dimensional wind field and parcel trajectories of a tornadic thunderstorm in order to examine the interaction between the storm flow, tornado parent circulation, and the

tornado itself. Brandes (1984) used a similar approach to examine mesocyclone evolution and vertical vorticity generation mechanisms in tornadic storms. More recently, Markowski et al. (2008) used pseudo-dual-Doppler data to compute vortex lines within several mesocyclones in order to explore possible vorticity generation mechanisms within supercells. Wurman et al. (2007) used very high-resolution observations from two Doppler on Wheels (DOW; Wurman et al. 1997) radars to analyze the vorticity budget terms in and near a tornado.

1.2.3 Advection correction techniques

Many studies have used radar-measured scalar quantities such as reflectivity to estimate (or improve estimates of) the air velocity field. Zawadzki (1973) used cross-correlations of precipitation patterns over successive times to estimate storm motion. Rinehart (1979) refined this technique into the Tracking Radar Echo by Correlation (TREC) method in order to examine flow in precipitating clouds. An alternative to maximizing correlation values is to minimize the total derivative of reflectivity. The advection velocity may also be estimated subjectively, for example, by visually tracking reflectivity echoes (e.g. Heymsfield 1978).

In all of these approaches, it is more accurate to say that advection velocities, not wind velocities, are retrieved. This is because the translational velocity of a pattern (e.g. reflectivity field associated with a thunderstorm) can deviate significantly from the wind velocity. Fortunately, estimates of the advection velocity field can nevertheless be valuable to the retrieval of the air velocity field. Most Doppler analysis techniques treat input radial velocity data as simultaneous. In reality, observations taken within a single volume scan may be separated by between one (e.g. sector-scanning mobile radars) and

five (e.g. WSR-88D radars performing full volume scans) minutes, resulting in large errors in interpolation and local derivative calculations. Some techniques therefore recast the analysis onto a moving reference frame (or frames) which approximate(s) the translation of reflectivity or radial velocity fields over the time window of the analysis. The advection velocity retrieval methods employed by these advection correction techniques typically invoke Taylor's frozen turbulence hypothesis (Taylor 1938), which assumes that a field (in this case, the 3-D wind field) is advected by the mean flow and does not evolve with time. The advection velocity is often assumed to be constant over the analysis domain.

The most well-known objective advection velocity retrieval technique is that of Gal-Chen (1982). The derivation of Gal-Chen's technique begins with a transformation of variables to a moving Galilean reference frame:

$$\begin{aligned} x' &= x - U\left(t - t_0\right), \quad u' = u - U, \\ y' &= y - V\left(t - t_0\right), \quad v' = v - V, \\ z' &= z, \quad w' = w, \quad t' = t, \end{aligned}$$

where U and V are constants (to be retrieved) describing the translational velocity of the reference frame, and unprimed quantities are defined on the moving reference frame. Gal-Chen pointed out that it is prudent to use radial velocity data for the retrieval since reflectivity fields tend to be more unsteady (and therefore more severely violate the frozen turbulence hypothesis). Of course, radial wind observations will differ between the stationary and moving reference frames even for a steady 3-D wind field since the orientation of the radial (with respect to the radar) vector changes with time. However, Gal-Chen demonstrated that, for a steady total wind field,

$$\frac{\partial^2}{\partial t'^2}(rV_r) = 0$$

in the moving frame. This expression was then transformed into the space-time coordinates of the fixed reference frame and reformulated as a cost function (with U and V as control variables) to be minimized. In this way, it is possible to objectively retrieve the advection velocity (U, V) by imposing frozen turbulence as a weak constraint on the radial wind field.

1.2.4 Variational methods

Many of the newer wind retrieval methods use variational approaches in which some or all of the model constraints are imposed in the weak (least-squares error) sense. A cost function accounting for the discrepancy between the model-predicted and observed variables is minimized by varying the model parameters, which are either initial or time-averaged quantities. Four-dimensional variational (4D-VAR) techniques often use an adjoint model to predict some of the variables in the model. Very sophisticated 4D-VAR methods may use a full numerical model to iteratively adjust the initial model parameters to observations and background wind fields over a time window (Sun et al. 1991; Kapitza 1991; Sun and Crook 1994, 2001). Owing to their complexity, such approaches are computationally expensive. A major advantage of 4D-VAR techniques is that observations can be processed at the time they occur, thereby eliminating error due to temporal interpolation as in traditional dual-Doppler analysis. Both 3D-VAR and 4D-VAR methods can also be used to incorporate multiple-Doppler data into the retrieval (e.g. Gao et al. 2004; Xue et al. 2007).

It is becoming increasingly common in variational Doppler analysis for constraints to be imposed exclusively in the weak sense. This approach has two major advantages. First, it allows constraints to be weighted differently from one another in the analysis. Thus, the wind retrieval can be made less sensitive to constraints that are more likely to be violated (due to, e.g., dynamical approximations or computational errors). Second, imposing only weak constraints gives one the option of using a standard minimization technique (e.g. conjugate-gradient) to determine the model parameters, thus bypassing the need to solve a set of Euler-Lagrange equations. This approach facilitates the inclusion of additional constraints in cases where it is easier to modify the adjoint model than to re-derive a set of Euler-Lagrange equations. It also removes the need to specify boundary conditions on *w* or to compute vertical integrals of horizontal divergence to determine *w* within the domain (however, dynamical constraints typically include derivatives of *u* and *v*, and so retrieval of the vertical velocity field is still sensitive to errors in the horizontal wind field). Of course, in cases where a set of well-known boundary conditions are available, it may still be desirable to impose them.

The following is a typical example of the cost function *J* used in 3D-VAR Doppler analysis, taken from Gao et al. (1999):

$$
\begin{aligned}
J &= J_O + J_B + J_D + J_S, \\
J_O &= \frac{1}{2}\sum_{m,n} \lambda_{m,n} \left(CV_r^{m,n} - V_{r_{obs}}^{m,n} \right)^2, \\
J_B &= \frac{1}{2}\left[\sum_{i,j,k} \lambda_{ub} \left(u - u_b \right)^2 + \sum_{i,j,k} \lambda_{vb} \left(v - v_b \right)^2 + \sum_{i,j,k} \lambda_{wb} \left(w - w_b \right)^2 \right], \\
J_D &= \frac{1}{2}\sum_{i,j,k} \lambda_D \left(\frac{\partial \bar{\rho} u}{\partial x} + \frac{\partial \bar{\rho} v}{\partial y} + \frac{\partial \bar{\rho} w}{\partial z} \right)^2, \\
J_S &= \frac{1}{2}\left[\sum_{i,j,k} \lambda_{us} \left(\nabla^2 u \right)^2 + \sum_{i,j,k} \lambda_{vs} \left(\nabla^2 v \right)^2 + \sum_{i,j,k} \lambda_{ws} \left(\nabla^2 w \right)^2 \right].
\end{aligned}
$$

Here, J_O, J_B, J_D *and* J_S are observational, background, mass conservation and smoothness constraints, respectively. C is an operator which interpolates analyzed radial winds to the observational space. J_O accumulates the squared differences between analyzed and observed radial winds over all observations (subscript m) for each radar (subscript n). J_B sums squared differences between the analyzed and background wind components over the analysis domain (i,j,k). J_D is the squared 3-D mass divergence over all analysis points using a pre-specified air density profile [$\bar{\rho} = \bar{\rho}(z)$]. Finally, J_S sums the 3-D spatial Laplacians of the three wind components over the domain. The penalty coefficients λ are used to weight more important or less error-prone constraints more heavily in the analysis. Gao et al. (1999) found that their results were not unduly sensitive to the choices for λ.

In order to minimize J, it is necessary to derive the gradients of J with respect to each of the control variables u(i, j, k), v(i, j, k) and w(i, j, k). The resulting adjoint equations are used by the minimization routine to compute the N-dimensional gradient of J, where N is the number of analysis points (typically i × j × k) multiplied by the number of control variables (in this case, three). Since it is not necessary to derive explicit solutions for the wind field using this variational approach (the solution is obtained by minimizing J), it is much simpler to include additional constraints in the analysis. However, if the new constraint is very complex, updating the adjoint equations can be a painstaking, albeit straightforward, task. This is especially true in cases where prognostic equations are included in the analysis (e.g. Sun and Crook 1996). Including too many control variables in the analysis increases the risk for multiple minima in J (solution non-

uniqueness), but this can be mitigated to some degree by the use of a smoothing or background constraint (Mewes and Shapiro 2002).

1.2.5 Vortex detection and characterization techniques

Since the implementation of the WSR-88D network, several algorithms have been developed to aid forecasters in identifying intense small- and meso-scale atmospheric circulations. The NSSL (National Severe Storms Laboratory) Mesocyclone Detection Algorithm (MDA; Stumpf et al. 1998) was designed to alert forecasters to the presence of supercell thunderstorms, which produce a large portion of all the tornadoes in the United States. The 88D TVS (Tornado Vortex Signature) algorithm (Mitchell et al. 1998) identifies circulations containing a region of radial wind shear (between velocity extrema) exceeding a certain threshold over 2 or more elevation angles as tornadic. Two major limitations of the 88D TVS method are 1) detections require the presence of a mesocyclone (identified by the MDA), whereas some tornadoes are not associated with supercells, and 2) the POD is < 5 % using the standard shear threshold of .002 s-1 (Mitchell 1995). Such a stringent threshold is necessary in order to avoid an unreasonably high FAR.

The NSSL TDA (Tornado Detection Algorithm) was developed to overcome these and other limitations of the 88 TVS algorithm (Mitchell et al. 1998). In this technique, radial shear is only calculated over azimuthally adjacent radar probe volumes (gate-to-gate) since most tornadic circulations do not extend over more than a few WSR-88D gates. Multiple shear thresholds are used in order to identify circulations on multiple scales. Circulations must exhibit vertical continuity to be counted as detections, and do not require the presence of a mesocyclone. Features can be tracked and, using linear

extrapolation, their future paths predicted. Unfortunately, this algorithm, though a major improvement over the 88D TVS method, is still reliant upon thresholds, the optimal values of which are largely situation-dependent and therefore unpredictable. Thus, unacceptably high FARs or low PODs may still occur with this technique, limiting its utility to the tornado warning process.

A number of vortex detection techniques have been developed which are less reliant upon gate-to-gate shear thresholds. The linear least squares derivative (LLSD) technique estimates the derivatives of the radial wind by least-squares fitting Doppler velocity observations to a linear spatial model (Smith and Elmore 2004). This method produces more accurate estimates of shear than methods which rely upon point-to-point velocity measurements. Fuzzy-logic approaches (e.g., Wang et al. 2007) acknowledge the typically large overlap between the probability distribution functions of parameters used in vortex detection techniques, as opposed to binary methods which use rigid thresholds to make detection decisions. Liu et al. (2007) proposed a preliminary tornado detection algorithm based on multi-scale wavelet analysis of radial velocity data. Finally, neural network methods have been developed which show skill in identifying precursor circulations for tornadogenesis (Marzban and Stumpf 1996). This approach also allows the level of confidence in the predicted outcome (tornado or non-tornado) to be computed.

Several techniques have been developed which fit radial velocity data to a vortex model in order to recover key characteristics of the vortex flow. Such retrieval methods were originally limited to airborne single-Doppler, dual-Doppler (Gamache et al. 1991) or pseudo-dual-Doppler (PDD, Marks and Houze 1984) analyses of tropical cyclones

(TCs). The latter technique is actually a single-Doppler method whereby data are collected by a single radar mounted aircraft flying two successive paths around the storm. The two flight legs are chosen such that the radar view angle is very different between the two trajectories, thus simulating a dual-Doppler analysis.

The PDD technique has two major limitations. First, it assumes the TC is in a steady state for the 1-2 h period required for data collection. Second, Lee et al. (1994) assert that the method cannot be applied in real-time since it requires too much time to construct the three-dimensional wind fields. The Velocity Track Display (VTD; Lee et al. 1994) method was therefore developed to extract circulation properties of TCs in real-time and with a minimum of human interaction. Data are collected by a single airborne Doppler radar during two flight legs. After each flight leg, a harmonic analysis is performed to decompose Doppler winds on constant radius (from the TC center), constant altitude rings into the tangential, mean radial and mean cross-track components of the horizontal flow. The analysis output can then be transmitted to forecast centers within minutes for use in tropical model initialization. Lee at al. (1994) performed a VTD analysis on Hurricane Gloria (1985) and found that the retrieved wind field was very consistent with a PDD analysis and with previous observations of TC's. The retrieval successfully depicted the asymmetric nature of the storm's kinematic structure. Thus, VTD was shown to be a capable method for examining circulation properties of the inner cores of TCs.

Several improvements to the original VTD technique have been devised within the last two decades. The Extended VTD (EVTD; Roux and Marks 1996) technique allows for the wavenumber 0 and 1 components of the radial wind to be recovered,

whereas the VTD method is only capable of retrieving the symmetric mean radial wind. Furthermore, the estimated storm center is allowed to vary with altitude, and the large gradients between rings of the tangential and radial wind components that can occur in VTD analysis are mitigated. These improvements are accomplished by simultaneously considering data collected during successive flight legs in the analysis, and by analyzing data at all rings simultaneously for each level.

The Ground-Based VTD (GBVTD; Lee et al. 1999) method was proposed in order to increase understanding of the evolution and wind structure of landfalling TCs. In this technique, a single Doppler radar is situated at the ground, thereby requiring a new geometrical formulation of the problem. As with the VTD method, the asymmetric component of the radial wind is not recoverable. This method has been used to decompose the wind fields of vortices other than tropical cyclones. Lee and Wurman (2005) used GBVTD to examine the three-dimensional structure of a tornado sampled by a Doppler-on-Wheels radar. Liou et al. (2006) extended the GBVTD method to overlapping data coverage from two radars (Extended GBVTD, or EGBVTD). This allowed for the radial wind component to be retrieved up to wavenumber 1 structure (as with EVTD), and also improved the accuracy of the recovered tangential wind. This technique was also capable of recovering more of the vortex wind field than traditional dual-Doppler analysis when data are missing.

1.3 Overview of New Technique

In the new technique presented herein, radial wind observations from two or more close-proximity Doppler radars with overlapping domains are fit to an analytical low-order model of a vortex and near-environment. The model control parameters include

vortex location, size, intensity, and translation velocity. This method is designed to capitalize upon the increased observational density and overlapping coverage of a CASA-like radar network to detect small-scale vortices (primarily tornadoes and tornado parent vortices, i.e. low-level and mid-level mesocyclones) and also to provide vortex characteristic estimates which may improve tornado nowcasting. This capability distinguishes this approach from traditional dual-Doppler analysis as well as many other real-time vortex detection algorithms, which do not constrain the retrieved wind field with a spatial vortex model and thus are not designed to explicitly retrieve vortex characteristics. The vortex parameters are obtained by minimizing a cost function which measures the discrepancy between the observed and model radial wind fields over an analysis space (volume) and time window. By taking the translation of the system into account, the radar data can be used at their actual locations and times of acquisition.

The technique presented herein belongs to the same class of retrieval techniques as the VTD methods, and is most similar to EGBVTD. As in EGBVTD, radial wind observations from two or more close-proximity Doppler radars with overlapping domains are fit to an analytical model of a vortex and its near-environment. However, there are some important differences between the two techniques which reflect their different purposes. In the present technique, the vortex center coordinates are model control variables, not fixed as in VTD. Thus, precise *a priori* knowledge of the vortex center location is not required for the new technique to be successful. This is desirable since center-finding algorithms (e.g. Lee et al. 2000) may be unreliable in cases where the vortex is poorly-resolved. Another difference is that the vortex portion of the model used herein is axisymmetric and considered valid over the entire analysis domain, while in

EGBVTD, the wavenumber 1 components of the radial and tangential vortex winds are recovered, and winds are analyzed on constant altitude, constant range rings. Thus, vortex wind fields (not the total wind field, which is the sum of the vortex and environmental flows) retrieved using the present technique have lower-order structure than those obtained using EGBVTD and the other VTD variants. This does not constitute a major limitation to the technique since tornadoes and low-level mesocyclones are generally not sufficiently resolved by operational radars for fine-scale features in their retrieved wind fields to be reliable.

The ability of this technique to provide estimates of operationally-useful vortex characteristics such as size and strength constitutes a major advantage over existing operational detection algorithms for several reasons. First, such estimates may allow for the development of more robust detection criteria than those used in shear-based methods since they are typically derived using more (sometimes many more) data points than are radial shear calculations. Second, the availability of vortex characteristic estimates to forecasters may be beneficial both when a tornado has already been detected (nowcasting) and when a low-level mesocyclone capable of producing a tornado is present (forecasting), particularly during outbreak events when storms must be triaged. Finally, vortex characteristics derived from this technique for a large number of real-world cases could be used to develop climatologies as well as to examine possible relationships between tornado parent vortices and tornado behavior and genesis. The results of such efforts could in turn be used to improve tornado forecasts.

The remainder of the dissertation is organized as follows. The details of the methodology of the technique are described in Chapter 2. Preliminary tests of the

technique using analytically-generated vortices and a high-resolution Advanced Regional Prediction System (ARPS; Xue et al. 2001) simulation of a tornado are presented in Chapter 3. Tests of the technique using real Doppler observations of intense vortices are discussed in Chapter 4. Important considerations for real-time implementation of the technique are discussed in Chapter 5. A summary and plans for future work are given in Chapter 6.

CHAPTER 2: DESCRIPTION OF TECHNIQUE

2.1 Low-Order Model

The low-order model used in this study is comprised of four idealized flow fields: a uniform flow, linear shear flow and linear divergence flow (together comprising the "broadscale" flow), and a modified combined Rankine vortex (MCRV). The use of the MCRV model is supported qualitatively by high-resolution mobile radar observations of tornadoes whose azimuthally-averaged tangential winds roughly followed this profile (Wurman and Gill 2000; Bluestein et al. 2003; Lee and Wurman 2005). The vortex and the horizontal broadscale fields are allowed to translate. A total of 19 parameters (Table 2.1) characterize the wind field in the low-order model. These parameters are considered constant over a single 4D retrieval domain. Thus, the low-order model will be violated in cases where the observed wind field rapidly evolves in time. Although the current low-order model is independent of height, the ARPS model fields used in the later tests do vary with height, and so provide a stringent test of the current model formulation. The height-independence of the low-order model is unlikely to be a major limitation since the technique is designed primarily to detect and retrieve convective vortices within the lower troposphere, which can be well-sampled (particularly in CASA-like radar networks) using relatively shallow (< 10°) elevation angles.

The broadscale portion of the model is described by

$$V_x = a + b(y - v_t t) + c\,(x - u_t t) + gz,$$
$$V_y = d + e(x - u_t t) + f\,(y - v_t t) + hz,$$

and the azimuthal velocity field v_θ and radial velocity field v_r of the MCRV are given by:

$$v_\theta = \begin{cases} \dfrac{r}{R} V_T, & r < R, \\ \dfrac{R^\alpha}{r^\alpha} V_T, & r \geq R, \end{cases} \qquad v_r = \begin{cases} \dfrac{r}{R} V_R, & r < R, \\ \dfrac{R^\beta}{r^\beta} V_R, & r \geq R, \end{cases}$$

where

$$r = \sqrt{(x - x_0 - u_v t)^2 + (y - y_0 - v_v t)^2} \,,$$

is the distance of a given (x, y) coordinate from the center of the vortex at time t. The complete derivation of the low-order model is given in the Appendix. There it is shown that the Doppler radar velocity, V_r^{mod}, is given by:

$$\begin{aligned} V_r^{mod} &= \cos\phi_n \sin\theta_n \left[a + b(y - v_b t) + c(x - u_b t) + gz + \frac{V_R}{R}(x - x_0 - u_v t) - \frac{V_T}{R}(y - y_0 - v_v t) \right] + \\ &\quad \cos\phi_n \cos\theta_n \left[d + e(x - u_b t) + f(y - v_b t) + hz + \frac{V_R}{R}(y - y_0 - v_v t) + \frac{V_T}{R}(x - x_0 - u_v t) \right] \\ &\quad r < R, \\ &= \cos\phi_n \sin\theta_n \left[a + b(y - v_b t) + c(x - u_b t) + gz + \frac{R^\beta V_R (x - x_0 - u_v t)}{r^{\beta+1}} - \frac{R^\alpha V_T (y - y_0 - v_v t)}{r^{\alpha+1}} \right] + \\ &\quad \cos\phi_n \cos\theta_n \left[d + e(x - u_b t) + f(y - v_b t) + hz + \frac{R^\beta V_R (y - y_0 - v_v t)}{r^{\beta+1}} + \frac{R^\alpha V_T (x - x_0 - u_v t)}{r^{\alpha+1}} \right] \\ &\quad r \geq R. \end{aligned} \tag{1}$$

where θ_n and ϕ_n are the azimuth and elevation angles, respectively, of the nth radar (θ_n is measured clockwise from the north). In some of the analytical experiments presented below, a cylindrical approximation to the true spherical geometry was used. This approximation is justified by the small elevation angle (0.5°) used in these experiments.

Experiments with the analytical and ARPS-simulated wind fields used a slightly simpler version of the low-order model presented above. The vortex and broadscale translational velocity were set equal to one another. Also, vertical shear was not accounted for. However, due to the small elevation angles and analysis subvolumes used

in those experiments, there was likely little aliasing of vertical shear into the horizontal in the ARPS experiments (and none in the analytical experiments).

Parameter	Description
a, d ($m\ s^{-1}$)	Uniform flow velocity
b, e (s^{-1})	Horizontal shear amplitudes
c, f (s^{-1})	Horizontal divergence amplitudes
g, h (s^{-1})	Vertical shear amplitudes (real data experiments)
R (m)	Vortex radius of maximum wind
V_R , V_T ($m\ s^{-1}$)	Maximum radial, tangential winds
x_0 , y_0 (m)	Vortex center location
u_t , v_t ($m\ s^{-1}$)	System translational velocity (analytical experiments)
u_b , v_b ($m\ s^{-1}$)	Broadscale translational velocity (ARPS and real data experiments)
u_v , v_v ($m\ s^{-1}$)	Vortex translational velocity (ARPS and real data experiments)
α, β	Vortex wind decay

Table 2.1. Description of low-order model parameters.

2.2 Cost Function Computation and Minimization

In order to retrieve the low-order model parameters, we seek to minimize the (squared) discrepancies between the observed and model-predicted radial wind fields summed over the spatial-temporal domains of the radars. By taking the translation of the broadscale flow and vortex into account, discrepancy calculations for the radial wind model can be performed at the same locations and times as the observations, thus bypassing the need for temporal interpolation, moving reference frames or other ad hoc procedures.

Since radar resolution volumes increase in size with distance from the radar, Doppler velocity observations become representative of winds over a larger region as range increases. A range-weighting factor, r_n/r_{mean}, is introduced to account for this. In reality, radar resolution volumes increase as the square of range (spherical coordinate probe volumes), but in the experiments with analytical and numerically-simulated data, resolution volumes are considered to be flat (cylindrical coordinate probe areas). However, it has been verified in other experiments (not shown) that the results are very similar regardless of which of these weighting functions is used. In experiments with real data, the proper range-weighting factor, r_n^2/r^2_{mean}, is used.

The cost function J accounting for the discrepancies between the observed and model-predicted radial wind fields can thus be expressed as

$$J \equiv \sum_{n=1}^{N} \sum_{m=1}^{M} \sum_{\phi} \sum_{\theta} \sum_{r_n} \left[\frac{r_n}{r_{mean}} (V_r^{obs} - V_r^{mod})^2 \right], \tag{2}$$

where N is the number of radars, M is the number of volume scans (temporal sum), r_n is the radial distance of an observation point from the nth radar (the range-weighting factor

is appropriately modified in experiments with real data as described above), θ is the azimuthal angle and ϕ is the elevation angle. J provides a useful way to quantitatively compare the accuracy of retrievals for different experiments, and, when appropriately normalized, yields the mean model error per radar grid point. In most of the retrieval experiments herein, only a single PPI (from a single volume scan) is used from each radar. This approach decreases the potential for violations of the low-order model, particularly when a vortex is rapidly evolving or exhibiting significant vertical variation in position, size or strength.

The cost function J is minimized to retrieve the set of parameter values producing the least squares error in the model wind (best fit between model and observed winds). In view of (2) and the location of the model parameters in (1), the minimization problem is highly non-linear. Conjugate gradient minimization methods have proven useful for such problems. The minimization algorithm used in this study is the Polak-Ribiere (1969) method, a robust and efficient variant of the Fletcher and Reeves (1964) algorithm. In both methods, the search direction is reset to that of steepest descent (with all previous direction and gradient information being discarded) every p iterations, where p is the number of model parameters.

In the analytical and ARPS experiments presented herein, the minimization algorithm was modified such that certain key model parameters are reset to their initial values if they exceed specified bounds. In particular, x_0, y_0 are reset whenever the provisional vortex center comes within a distance R (radius of maximum wind) of the edge of the analysis domain due to the existence of spurious minima in J near the domain boundaries (Chapter 3.5.1). In addition, R is constrained to be larger than 10 m since

vortices smaller than this are unlikely to be resolved by even a CASA-like radar network, and since negative values of R are physically impossible but could be obtained computationally.

As with other minimization techniques, multiple minima in J can prevent the desired minimum (which in some cases is not the global minimum) from being reached. Multiple minima in the current problem can result from the intrinsic non-linearity of the problem, as well as from areas of missing data and departures of the observed wind field from the model. The threat of multiple minima increases as the surface of the cost function becomes more elliptical. In order to reduce the ellipticity of J and thus increase the convergence rate of the minimization algorithm, the first guess vector is scaled such that the gradients of J with respect to each of the parameters become closer in magnitude (as in Wang et al. 1997). To accomplish this, the scaling factors are set equal to physically realistic values of each of the parameters. Experiments (not shown) have indicated that the technique is not unduly sensitive to the selection of scaling factors for physically reasonable ranges of these factors.

2.3 Selection of Analysis Domains

Using enough analysis domains to cover the entire dual-Doppler domain would, in the absence of a high performance computing cluster, require too much time for the technique to be applied operationally in the near future. Therefore, in tests with real data, retrievals are performed only in regions identified as likely containing intense vortices. The process by which these regions are selected begins by identifying all pairs of azimuthally-adjacent radar gates (in both radar domains) which satisfy a set of criteria. Since the typical resolution and quality of velocity data can differ significantly between

different radar platforms, the optimum domain-selection criteria will likewise vary. However, in all of the real-data experiments described herein, the following set of criteria was successful: (1) the azimuthal distance between the two gates is < 1 km; (2) the radial velocity difference or the azimuthal shear of radial velocity calculated between the two radar gates exceeds a prescribed threshold; (3) radial wind speed and (optionally) reflectivity exceed prescribed thresholds in at least one radar gate (8 May 2003 experiments) or within 3 km of the centroid of the gate pair (remaining real-data experiments); (4) at least 75 % of the radial velocity magnitudes within 3 km of each gate exceed 1 m s^{-1}; and (5) < 20 % of the velocity data is missing within both 500 m and 1000 m of each of the gates. Criterion 1 is designed to restrict the vortex retrievals/detections to smaller-scale vortices such as tornadoes and low-level mesocyclones. Criteria 2 and 3 are intended to filter vortices that are not strong enough to be significant to forecasters. The reflectivity threshold in criterion 3 reduces the false alarm rate outside of convective storms. Criterion 4 follows from the observation that spurious radial wind data are more common in weak-velocity regions of the IP-1 fields. Criterion 5 was partly motivated by analytical experiments in which velocity data gaps produced spurious minima in J (Section 3.5.1). Again, these preliminary criteria are based on tests from a limited number of cases (not all of them from IP-1) and so may be modified in the future. It is currently unknown whether the analysis domain selection criteria are (or can be modified to be) sufficiently robust to simultaneously maintain a low number of retrieval domains and a high probability of detection over a wide range of scenarios. If a large number of retrievals are sometimes needed, then parallel processing

(one processor for each set of analysis domains) could be used to produce acceptable computational wall clock times.

For each pair of radar gates satisfying the domain-selection criteria, the centroid of the two gates is stored. Since vortices always exhibit azimuthal shear signatures in the velocity fields of both radars, all centroids which are located within 2 km of another centroid in the other radar's domain are retained. All such points are then spatially grouped into clusters (since there may be multiple proximate points associated with the same vortex) whose centroids are calculated and stored. Each centroid corresponds to the center of a region over which the retrieval technique will be applied. A horizontal grid of nine first guesses for the vortex center (each serving as the center of an analysis domain over which the retrieval is applied) is subsequently calculated and input to the retrieval routine (Fig. 2.1). The spacing between the vortex center first guesses is 500 m in both directions. The use of multiple first guesses for the vortex center makes provision for the presence of multiple vortices or of minima in J that are unassociated with vortices.

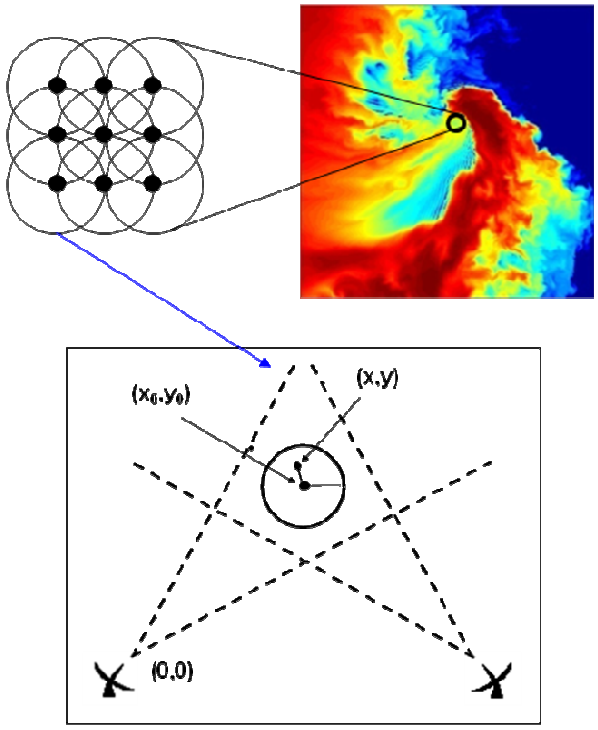

Figure 2.1. Schematic illustrating the procedure for selecting the wind retrieval domains. The algorithm searches for regions within the multiple-Doppler radar domain that satisfy prescribed radial velocity and (optionally) reflectivity criteria. Within each identified region, retrievals are performed over a grid of circular domains whose centers serve as the first guesses for the vortex location(s).

2.4 Retrieval Procedure

Unfortunately, the global minimum in J does not always correspond to the desired solution. This situation can occur when a tornado or other intense, small-scale vortex is embedded within a larger vortex or vortex-like circulation, such as a mesocyclone. In such cases, the larger circulation, by virtue of its larger "footprint", may fit the low-order model better than the smaller vortex, thus preventing the latter from being detected. In order to address this problem, the minimization procedure was initially split into two steps. In step 1, the vortex model parameters are fixed at zero (except for R since this would introduce a "division by zero" computational issue), and the broadscale parameters

are retrieved. In step 2, the radial components of the wind field retrieved in step 1 are subtracted from the observed radial wind fields, and the retrieval is then repeated on the residual wind field. Since the flow retrieved in step 1 (and subtracted in step 2) is much more representative of the broadscale flow than of the tornadic flow, the tornadic component of the original flow dominates the residual field to be retrieved in step 2, thus improving the vortex retrieval and increasing the probability of detection. In addition, to make the retrieval more sensitive to the tornadic flow relative to the (presumably weaker) broadscale flow in step 2, the cost at each observation point is multiplied by the square of the observed wind.

In experiments with real observations (except for the 8 May 2003 tornado retrievals described in Section 4.1), the retrieval procedure was expanded from two to four steps in order to allow the location and size of the analysis domain to be adjusted according to a preliminary vortex retrieval. This modification was motivated by the fact that the analysis domain will occasionally be much larger than the vortex being retrieved. In such cases, a smaller analysis domain would be desirable since it would allow the vortex to be more salient in the wind field.

The first two steps of the four-step retrieval procedure are the same as described above. At the end of step #2, if the retrieved $|V_T|$ exceeds a threshold (defined in Section 2.5), the retrieval proceeds to step #3; otherwise, the retrieval terminates and no vortex detection is made. Steps #3 and #4 are identical to steps #1 and #2 except the analysis domain is modified according to the size and location of the vortex retrieved in step #2. The new analysis domain is centered on the retrieved vortex location valid midway through the period over which the retrieval is performed. The analysis domain is also

resized such that the distance between its edge and the nearest point on the retrieved vortex core at the end of the retrieval period is 500 m. The analysis domain used in steps #3 and #4 is thus designed to be as small as possible while still encompassing the stronger vortex winds. If the modified analysis domain would be larger than the default domain, the modified analysis domain radius is set equal to the default domain radius. The technique also ensures that the modified analysis domain is large enough to include 3 or more radials from each radar.

If the V_T retrieved in step # 4 exceeds a threshold value, a set of detection criteria (described in Section 2.5) is used to determine whether an intense vortex has been detected. Otherwise, no information is output and the retrieval procedure restarts at the next first guess vortex center.

2.5 Detection Criteria

One of the most important considerations in developing appropriate detection criteria for this technique was the vortex parameter solution non-uniqueness that occurs when the actual vortex core is small relative to the observational resolution. In these cases, the combination of the limited observational resolution and ellipticity (flatness) in J owing to the mathematical nature of the vortex (MCRV) model can create numerous local minima. In particular, this problem frequently results in significant underestimation (overestimation) of R and overestimation (underestimation) of V_T. This is because, on the scale of the observational resolution, a strong, narrow (poorly-resolved) vortex resembles a weaker, wider (well-resolved) vortex and vice versa (Fig. 2.2). Large errors in the retrieved vortex model parameters can therefore result, as demonstrated in Section 3.5.3.

It would therefore be dangerous to unconditionally use these parameters to distinguish between intense and weak vortices.

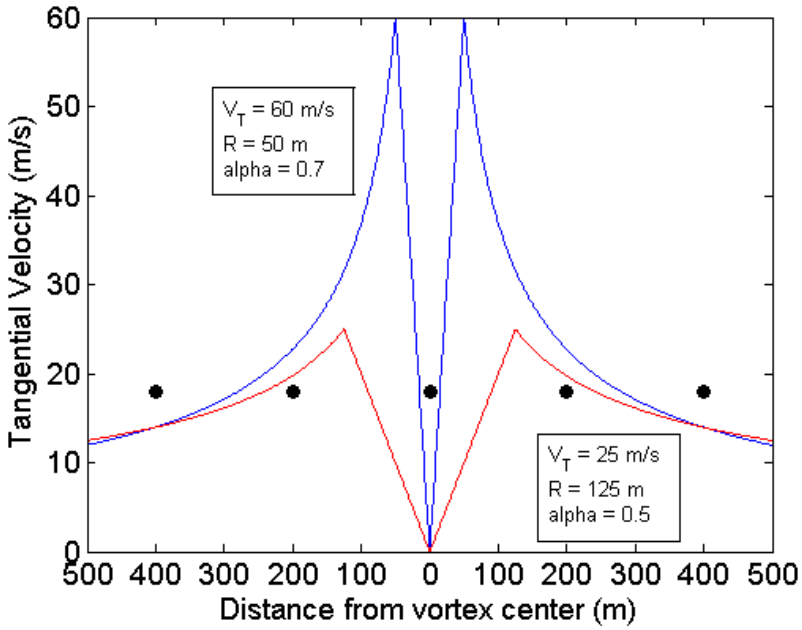

Figure 2.2. Tangential velocity profiles for two very different MCRVs. The black dots represent the centers of hypothetical radar probe volumes separated in space by 200 m. Since radar moments are weighted probe-volume averages, these two vortices would appear much more similar in the level-II radial velocity data.

The approach used in the final version of the technique is to identify and utilize retrieved vortex characteristics that are verified by the velocity observations. If the V_T retrieved in step #4 exceeds a threshold, V_{det}, then the outer (i.e. outside the vortex core) radius of V_{det} m s^{-1} tangential vortex wind, R_{det}, is calculated. Also calculated are the vortex radii of n m s^{-1} tangential vortex wind, R_n, for a series of values starting with V_{det} (default: V_{det}, V_{det}+5, …, V_{det}+25). The tangential (relative to the retrieved vortex center) components of the residual radial winds (calculated in retrieval step # 3 and treated as vectors here), V_{obs}', are also computed (Fig. 2.3). For each value of n, all the V_{obs}' that exceed n and that are located within R_{det} of the vortex center are identified. If there exists

at least one pair of such V_{obs}' that are separated from one another by > 90° relative to the vortex center, then the value of n is output to the user (this minimum angular separation criterion helps prevent regions of strong linear shear from being identified as strong vortices). If the maximum n meeting these criteria, V_T^{res}, exceeds V_{det}, then the vortex is tentatively classified as a detection. This approach is inherently conservative since the radial (residual) winds from which the V_{obs}' are calculated are themselves only components of the total velocities, meaning that the V_{obs}' and thus V_T^{res} will generally be underestimates. The threshold that the provisional V_T must exceed at the end of step # 2 of the retrieval procedure is the smaller of V_{det} and 10 m s^{-1}.

Preliminary detections are subsequently subjected to a set of criteria designed to filter spurious retrievals. If ≥ 25 % of the velocity data located within R_n of the retrieved vortex center are missing, or if the portion of the retrieved vortex with $V_\theta > n$ extends outside of the analysis domain, the retrieval is rejected since data edges often give rise to local minima. The retrieval is also rejected if the root-mean-square (rms) error (difference between observed and retrieved radial velocity) computed within R_{det} of the retrieved vortex exceeds the rms observed velocity over that same area for one or both radars. This criterion is crucial since retrievals that provide a poor match to the observed wind field can nevertheless be associated with local minima in the typically highly complex cost function surface, particularly when spurious velocity data are present (see Section 4.4.3).

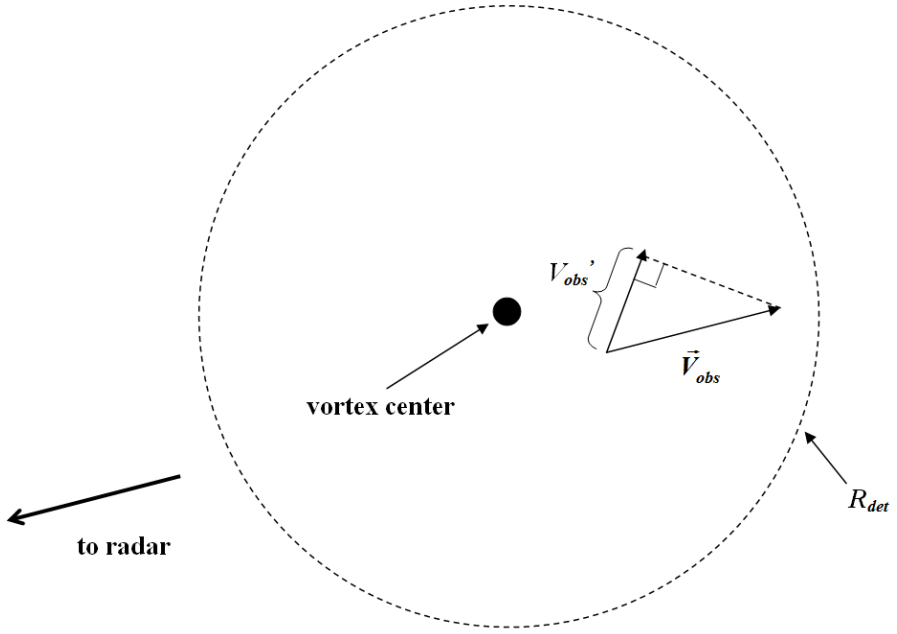

Figure 2.3. Verification of n, R_n.

CHAPTER 3: OBSERVING SYSTEM SIMULATION EXPERIMENTS

3.1 Radar Emulation

The low-order technique was initially tested with two kinds of idealized wind fields: (i) analytically-generated vortices with surrounding broadscale flow, and (ii) ARPS-simulated wind observations of a tornado-like vortex and its near-environment. Analytical data were calculated from the low-order model equations, and thus represent an overly-optimistic (identical twin) framework. However, significant random errors (described below) were added to the analytical radial wind data in order to partially mitigate this problem. Table 3.1 lists the model parameter values used to generate the input wind field in the analytical retrieval experiments. Both the idealized nature of the input wind field and the ability to specify the true wind parameter values facilitated testing of the algorithm code and identification of potential problems inherent to the technique. In contrast, the ARPS-simulated tornado is not constrained by the low-order model and therefore poses a greater challenge to the technique. On the other hand, there is some subjectivity in determining the "true" values of model parameters corresponding to the ARPS vortices; this is not a major concern for reasons discussed later. Data in the ARPS experiments are trilinearly-interpolated from the ARPS grid to the radar domain. Since the latter domain is generally coarser than the ARPS domain, the radial wind field sampled by the algorithm loses some of the finer features in the ARPS wind field, particularly at larger ranges from the radar.

Parameter	Description	True Value	EXP1 Mean Retrieved Value	EXP1 Standard Deviation	EXP2 Retrieved Value
a ($m\ s^{-1}$)	Uniform flow	10	9.4	0.7	11.6
d ($m\ s^{-1}$)		10	9.4	0.4	11.2
b (s^{-1})	Shear amplitudes	.002	.0023	.0004	.0012
e (s^{-1})		.002	.0021	.0004	.0024
c (s^{-1})	Divergence amplitudes	.0015	.0019	.0002	.0010
f (s^{-1})		.002	.0024	.0004	.0014
R (m)	Radius of max wind	200	202	11	309
V_R ($m\ s^{-1}$)	Max radial, tangential wind	-10	-9.9	1.0	-9.4
V_T ($m\ s^{-1}$)		50	48.3	1.4	38.6
x_0 (m)	Vortex center	5000	4997	9	5003
y_0 (m)		5000	4998	10	4997
u_t ($m\ s^{-1}$)	Translational velocity	-10	-9.9	1.8	-10.1
v_t ($m\ s^{-1}$)		-10	-10.0	1.6	-9.9
α	Vortex wind decay	0.7	.687	.056	0.75
β		0.4	.374	.135	0.78

Table 3.1. True values of low-order model parameters used in analytical retrievals, and the retrieved values from a set of eight retrievals (EXP1) and one single retrieval (EXP2).

To simulate weighted averaging of actual radar moment data within a resolution volume, simple range- and beam-weighting functions (no power weighting) are applied to a distribution of hypothetical scatterers within each resolution volume in both the analytical and ARPS experiments. The range weight at a given point within the resolution volume is defined by a trapezoid function with value of unity between 20 m

and 80 m along the beam and linearly decreasing to zero at the edges of the resolution volume (range resolution = 100 m). This weighting function is similar to one used to emulate a WSR-88D range pattern (Wood et al. 2004). The azimuthal weight is given by

$$W_{az} = exp\left[-8 ln 2 (\frac{\theta - \theta_0}{\theta_B})^2 \right],$$

where θ_0 is the azimuth of the center of the beam and θ_B is the half-power beamwidth, which is set to 2° in most of the ARPS experiments (to be consistent with the half-power beamwidth of current CASA radars) and to 1° in the analytical experiments (to verify the code is free of error). The scanning strategy used in these experiments is further discussed in Chapter 3.3.

In most of the analytical experiments, Gaussian random errors [generated using the Box and Muller (1958) method] were added to the volume-averaged observations, with the first standard deviation of the percent error distribution lying between -30 % and 30 %, and the portions of the distribution beyond +/- 50 % being truncated at +/- 50 %. These large input errors represent serious contamination of the otherwise "optimistic" test data. No error was added to V_r observations in the ARPS experiments described below because (i) the ARPS data do not have to satisfy the low-order model (indeed, significant asymmetries not accounted for in the low-order model are evident in the ARPS fields) and (ii) the ARPS data are themselves "noisy" on the grid-scale.

3.2 ARPS Simulation

The numerically-simulated supercell/tornado data used to test the algorithm were generated in a very high-resolution run of the ARPS model (case considered in Xue et al.

2007). The model thunderstorm was initiated by a thermal bubble placed in a homogeneous environment defined by a sounding proximate to the 20 May 1977 Del City, Oklahoma supercell storm. Computations were performed over a 48 km × 48 km domain with 50 m horizontal grid spacing and a stretched vertical grid spacing increasing from 20 m at the surface to about 80 m at 1 km AGL to 380 m at 16 km AGL. The simulation used in this study was performed with a 25 m horizontal grid spacing over a 30 min period centered on the time at which the 50 m grid tornado was most intense (the initial condition for the 25 m run consists of data interpolated from the 50 m grid simulation). Time-splitting was used to integrate acoustic waves on a finer temporal scale than used for the other processes. The integration was performed with large and small time steps of 0.125 s and 0.04 s, respectively. Subgrid-scale turbulence was assumed to be isotropic, and the 1.5-order TKE turbulent mixing formulation by Moeng and Wyngaard (1989) was used. The Kessler-type warm rain microphysics was used. Due to the large storage requirement (over 100 MB) for each volume of data over the sub-domain used in the retrieval experiments, output data were only made available to the algorithm at 10 s intervals. The data used in the retrieval experiments begin ~13,200 s into the simulation (600 s after the initialization of the 25 m simulation). All references to time are relative to this 13,200 s simulation time. The integration proceeded in a translating reference frame chosen to maintain the parent storm near the domain center throughout the duration of the simulation.

Figure 3.1 shows the reflectivity field (derived from rainwater mixing ratio) at the initial time (t = 290 s after the beginning of the dataset) of some of the retrieval experiments. The tornado center appears to be collocated with the minimum in the near-

surface pressure field at x = 3925 m, y = 4425 m (not shown). This places the tornado along the leading edge of the hook echo signature, as is commonly observed. The tornado vortex is surrounded by a reflectivity ring. A close-up view of the wind vectors in the tornado-like vortex (hereafter referred to as a "tornado") and the broader, weaker circulation in which it is embedded is presented in Fig. 3.2. The degree to which the simulated tornado resembles actual tornadoes at fine scales is not of major concern here since any differences would be barely discernable in the (relatively coarse) emulated radial velocity data. Instead, the ARPS dataset is used to test the retrieval method for a complex asymmetric flow with vortices that have a similar scale to observed tornadoes and that in many cases are near the limits of observation resolution.

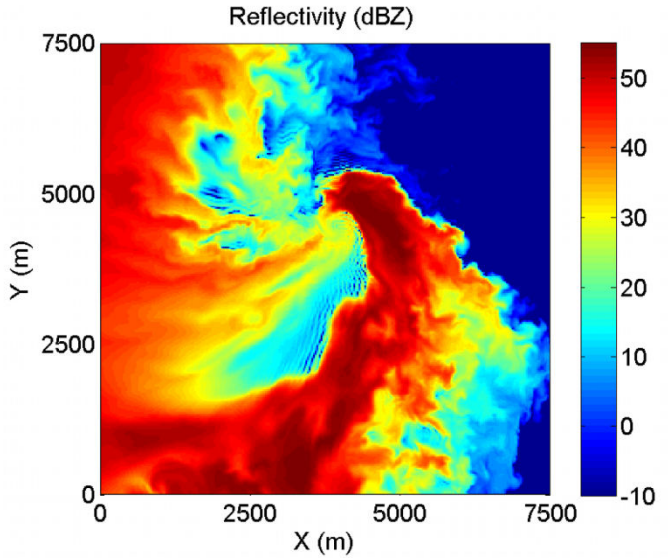

Figure 3.1. ARPS reflectivity field (dBZ) at z = 108 m AGL and t = 290 s.

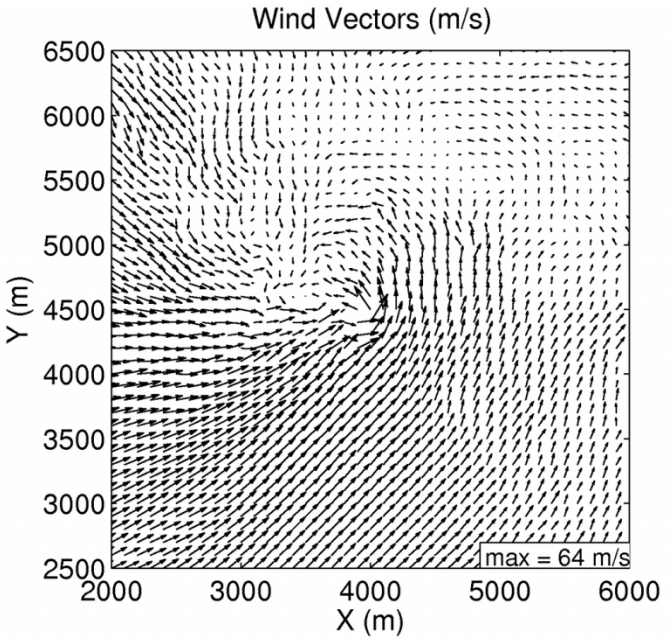

Figure 3.2. Horizontal wind field in and around ARPS-simulated tornado at z = 108 m and t = 290 s. Only vectors at every fourth grid point are displayed.

3.3 Radar Scanning Strategy

The radar-vortex geometrical configuration used in the majority of the Observing System Simulation Experiments (OSSEs) is depicted in Fig. 3.3. Two radars performing 90° sector scans at a tilt of 0.5° are positioned to give a cross-beam angle of ~ 90° at the location of the vortex. In experiments with the ARPS simulation, the tornado is located roughly 28 km from both radars, which are separated by 40 km (representative of a CASA radar network). In contrast, in the analytical experiments, a radar-vortex distance of only ~7 km was used. This admittedly optimistic configuration was adopted to facilitate verification of the code and identification of any obvious defects in the basic formulation. In the ARPS experiments, wind data are simultaneously valid over the spatial domain at each model time step and so each individual radar sector scan is assumed instantaneous. In the analytical experiments, each 0.5° sector scan takes 3.6 s to complete. Unless stated otherwise, a return period of 30 s between three consecutive sector scans is used in the analytical experiments, giving a temporal domain of 70.8 s. A return period of 60 s between two consecutive sector scans is used in the majority of the ARPS experiments. Such short return periods are possible with CASA radar systems because they are designed to dynamically adapt their scanning strategy to the type(s) of weather present in the network (e.g. sector-scanning an intense low-level circulation). The radars sample at 100 m range intervals and every 0.5° or 1.0° in azimuth. The beamwidth was set to 1.0° in the analytical experiments and in one set of ARPS experiments; a beamwidth of 2.0° was used in the remaining ARPS experiments.

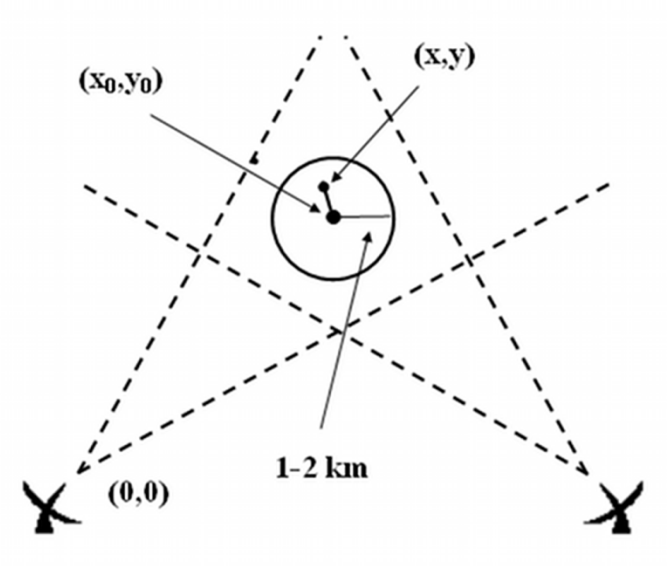

Figure 3.3. Radar-vortex geometry and analysis domain.

3.4 First Guess Parameter Values

In the analytical experiments, first guess (FG) errors were typically set to +50 % of the true parameter values (see Table 3.1). The exception was the FG vortex center error, which was typically set to a value in the range of 0.5 km – 1.84 km.

In the experiments with ARPS data, the first guess for most parameters was set to zero. First guesses of 100 m, 0.7 and 0.7 were used for R, α and β, respectively. A 500 m grid of nine FG vortex centers (each corresponding to a separate retrieval) was centered on the estimated ARPS tornado center, which was assumed to be collocated with the minimum in the horizontal pressure field near the height of the observations.

3.5 Analytical Experiment Results

3.5.1 Sensitivity to first guess vortex center

In order to assess the impact of error in the first guess for the vortex center, eight retrievals were performed with analytical data using FG vortex center values with errors of 1.4 km or 1.84 km (+50 % FG errors were used for the remaining parameters; see Table 3.1 for the true parameter values). It is important to note that in the analytical experiments, only observations taken within a circular 2 km radius domain centered on the FG vortex center were used. All four retrievals with 1.4 km error converged to a solution very close to truth. However, in the retrievals with the 1.84 km error in FG vortex center, the provisional vortex center exited the analysis domain during the minimization procedure. The failure of the algorithm to converge to the desired solution was likely due in part to the relatively low values of J when the provisional vortex center is near the edge of the analysis domain. The tendency for J to decrease near the edge of the analysis domain in these experiments is due to the fact that the misfit between the observed wind field and an erroneously positioned model vortex is smaller when more of the model vortex wind field is outside the analysis domain.

An example of the impact of the data boundary is depicted in the plot of $J(x_0, y_0)$ for the case where the true vortex location is (5000 m, 5000 m), the FG vortex location is (3700 m, 3700 m), and the remaining parameters are set to their FG values (Fig. 3.4). During this particular retrieval, the provisional vortex center migrated toward the middle of the lower edge of the plot, which might be expected given the topography of J. Failure to retrieve the vortex center prevented the retrieval of the remaining vortex parameters.

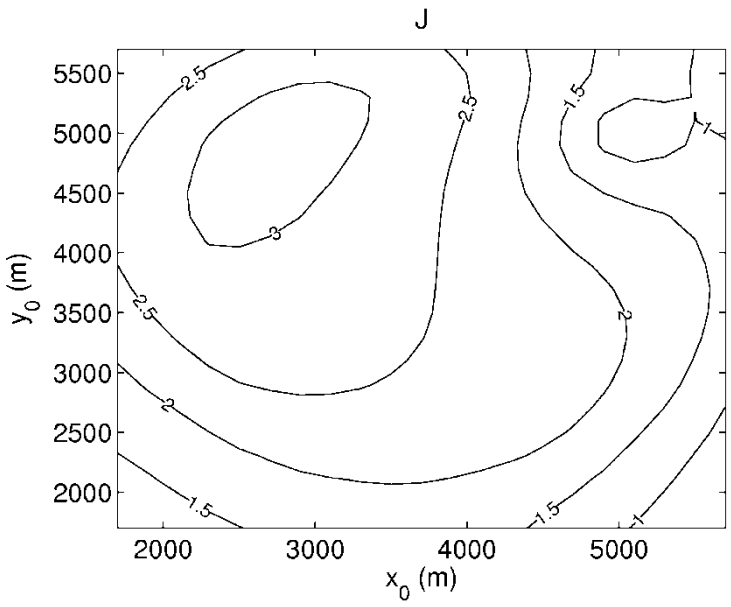

Figure 3.4. Plot of $J(x_0, y_0)$ with remaining model parameters set equal to their first guesses. Contour units are 10^6 m^2 s^{-2}.

The potential for a provisional vortex center to diverge from the desired solution (and possibly leave the analysis domain or converge to a spurious minimum) increases with the error in the FG vortex center. As discussed in Chapter 2, multiple minima in J may also occur when a vortex is near a large area of missing data, or when the low-order model is violated. Dual-Doppler analyses (Wurman et al. 2007a, 2007b) and numerical simulations (Wicker and Wilhelmson 1995; Xue et al. 2007) of tornadic storms indicate that the near-tornado wind field can be highly complex in nature, often consisting of other, non-tornadic vortices. Multiple first guesses for the vortex center were therefore used in the ARPS and real-data experiments in order to maximize the probability of identifying all intense vortices present. The FG values of the remaining low-order model parameters are not varied since the success of the algorithm is much less sensitive to errors in these parameters (e.g. Table 3.1).

3.5.2 Sensitivity to observational error

A set of eight experiments (EXP1) was performed in which different realizations of Gaussian random errors were added to the emulated radial wind observations. The FG vortex center error was set to 1.4 km, and +50 % errors were added to the remaining model parameters. Table 3.1 lists the mean and standard deviation of the set of retrieved values for each parameter. The agreement between the retrieved and true parameter values is generally very good, indicating that the technique is not unduly sensitive to random observational error or to errors in the first guess parameter values.

3.5.3 Vortex parameter non-uniqueness

In order to assess the capability of the algorithm in a less optimum radar-vortex geometrical configuration, a set of four retrieval experiments (EXP2) was performed using a beamwidth of 2.0° (with 1.0° oversampling) and a radar-vortex distance of ~28 km as in the ARPS experiments (to be described later). The four-fold increase in the radar-vortex distance (compared to EXP1) is associated with a four-fold coarsening of the azimuthal resolution. The vortex core (region of solid-body rotation) is consequently not resolved in the emulated radial velocity observations in this set of tests. The FG error in each retrieval was 500 m for the vortex center and +50% for the remaining model parameters. A perfect observation set was used to isolate the effects of coarser resolution. Tests redone with observational error produced similar results (not shown) to those described below. The true and mean retrieved parameter values are listed in Table 3.1. Significant errors occurred in R, V_T, and β (up to 61 %, 26 % and 97 %, respectively). These errors are not surprising since the model parameters describing the

structure of the vortex wind field cannot be reliably retrieved if the vortex core is poorly resolved (Chapter 2.5). On the other hand, in cases where the inner structure of the tornado is well-resolved (e.g. EXP1), vortex parameter non-uniqueness does not occur.

3.5.4 Broadscale translation parameter non-uniqueness

Experiments with analytically-generated data were performed to see if the broadscale translation components (u_b, v_b) could be retrieved separately from the vortex translation components (u_v, v_v). Figure 3.5 shows a plot of $J(u_b, v_b)$ for the case where the remaining model parameters are set to their true values and no error is added to the radial wind observations. The global minimum in J, corresponding to the correct solution (u_b, v_b) = (10, 10) m s^{-1}, is embedded within a highly eccentric elliptical region of $J(u_b, v_b)$.

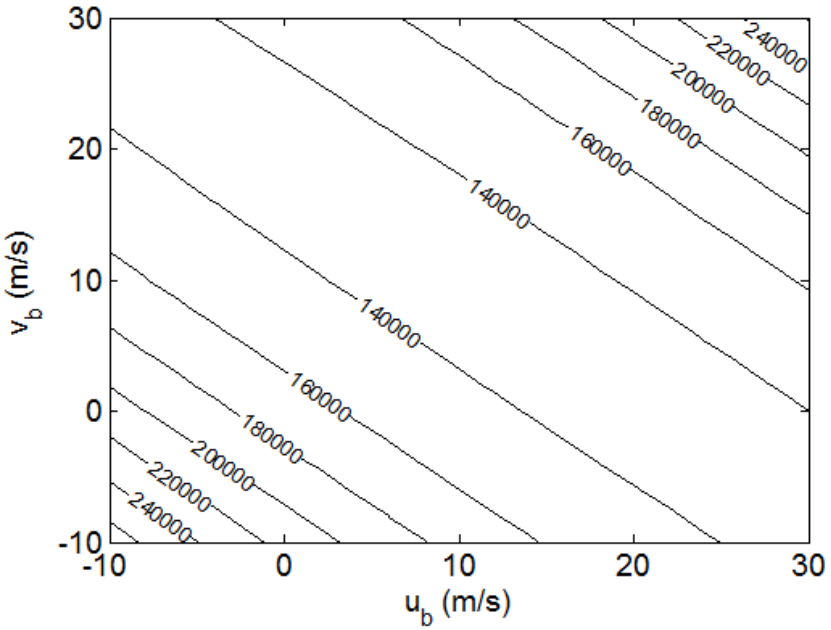

Figure 3.5. $J(u_b, v_b)$ with perfect first guess for remaining parameters.

The non-uniqueness in the broadscale translation parameters (u_b, v_b) can be explained by reformulating the low-order model in terms of (u_b, v_b) as $cu_b + bv_b = M$, eu_b

$+ fv_b = N$, where M and N contain the remaining variables in the radial wind equations. From linear algebra, we know there could be multiple solutions for (u_b, v_b) if the determinant of this system vanishes: that is, if $cf - be = 0$. Similarly, if the determinant is very small, there are many values of (u_b, v_b) which approximate the true solution (the problem is ill-posed), resulting in a $J(u_b, v_b)$ that is nearly flat close to the true solution. In initial experiments with (u_b, v_b), the selected values of *b, c, e,* and *f* resulted in a very small determinant. Plots of $J(u_b, v_b)$ (not shown) for sets of parameter values resulting in larger determinants were consequently less elliptical, however, significant errors still occurred in u_b and v_b. Similar results were obtained with the ARPS-simulated wind field using estimates for the "true" model parameter values.

Since a large number of potential solutions for (u_b, v_b) may exist in practice, these parameters were not retrieved in the analytical and ARPS experiments. Fortunately, experiments with and without these variables (not shown) revealed that their omission had little negative impact on the retrieval of the remaining vortex and broadscale parameters. The broadscale translation parameters were retrieved in the experiments with real data but were not examined or used.

3.5.5 Vortex translation parameter non-uniqueness

In preliminary experiments with real data, the vortex translation parameters were often the most difficult vortex parameters to retrieve. In cases where the distance traveled by the vortex during the retrieval period is small relative to the observational resolution, the intrinsic uncertainty in the vortex center creates a large flat region around the global minimum in $J(u_v, v_v)$. This is illustrated in Figure 3.6 for an analytically-generated vortex and background wind field. Flat regions in J tend to be problematic

since they are more prone to containing local minima (common causes of which were listed above), thereby making the retrieved minimum more sensitive to the first guess.

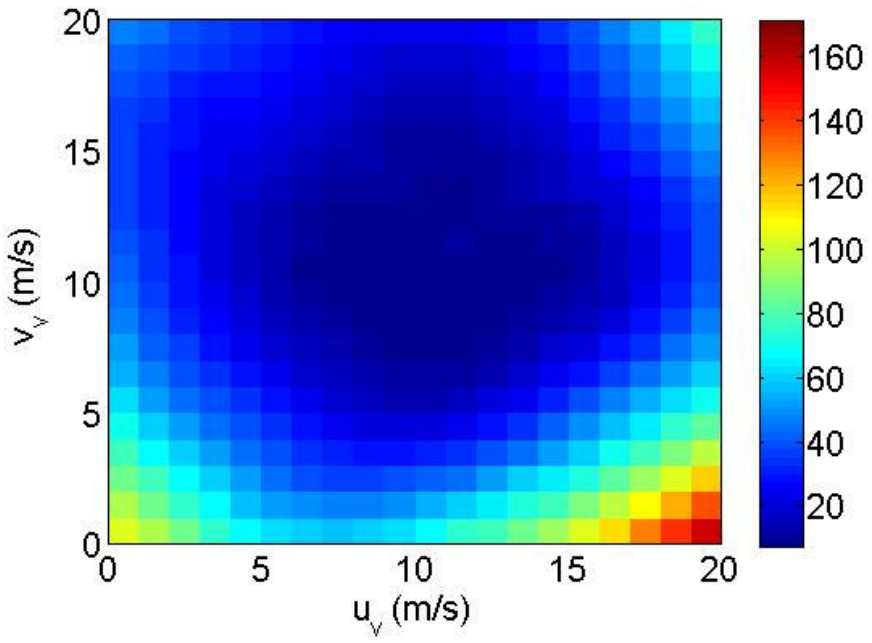

Figure 3.6. $J(u_v, v_v)$ (10^6 m^2 s^{-2}) for an analytical vortex with true $(u_v, v_v) = (10, 10)$ m s^{-1}. Remaining parameters are set to their true values.

Much more significant errors in the retrieved vortex translation parameters, as well as in the vortex location itself, can occur when multiple regions of azimuthal radial wind shear (including one or more vortices) exist within the analysis domain. In these cases, the retrieved vortex locations valid at the times of each radar scan may in reality correspond to two different features (two different vortices or one vortex and one shear zone). This can result in large errors in (u_v, v_v) and, if the feature "detected" in the first radar scan is not the vortex "detected" in the second radar scan, in (x_0, y_0) as well. The larger the errors in the first guess vortex location and translation velocity, the greater the

probability of the technique mistakenly identifying two separate shear features as a single vortex.

In order to improve the retrieval of the vortex translation and location parameters, particularly in the situation just described, a series of steps was taken to obtain a better first guess for (u_v, v_v) and (x_0, y_0) in the real-data experiments (excluding the 8 May 2003 experiments). First, before the wind retrieval is performed, the Gal-Chen (1982) advection retrieval method is applied to the reflectivity field within a circular domain (radius = 10 km) centered on the original analysis domain. Reflectivity data from the current and immediately previous scans of the nearest radar are used; the elevation angle is the same as that used in the wind retrieval. The retrieved reflectivity pattern translational velocity is then used as the first guess for the vortex translational velocity in step #2 of the retrieval procedure. At the end of step #2, J is calculated on a 4D grid of u_v, v_v, x_0 and y_0 values centered on the retrieved solution. The set of (u_v, v_v, x_0 and y_0) values with the smallest J is used as the first guess for these parameters in retrieval step #4. Ideally, this improved first guess will increase the probability that the minimization procedure converges to the desired solution.

3.6 ARPS Experiment Results

3.6.1 Retrieval results

Since the sounding velocity had been subtracted from the ARPS simulation in order to keep the parent storm near the center of the computational domain, the simulated tornado moved very slowly (< 5 m s^{-1}) relative to the two emulated radars during initial retrieval experiments**.** This significantly limited the capability of the technique in the

cases when the tornado was poorly sampled and when only two or three volume scans from each radar were used. Presumably this is because a slow-moving tornado which is poorly sampled by the first volume scan will also be poorly sampled throughout the remaining retrieval period. In order to legitimately increase the rate of change of the two radar-tornado viewing angles, the emulated radars were made to translate at a velocity opposite to that which had been subtracted from the ARPS simulation. The subtracted velocity was then added back onto the ARPS wind data for kinematical consistency. The translation velocity of the observed wind field (including the tornado) relative to the radars' reference frame was thus increased to approximately 20 m s^{-1}. This framework is equivalent to one with stationary radars and a data field which translates at the original velocity (before subtraction of storm motion). While this approach was justifiable in these preliminary tests, it should of course be kept in mind that a poorly sampled, slowly-moving tornado may well remain undetected during real operations.

Fourteen consecutive retrievals were considered with the ARPS data. The retrievals were applied at 30 s intervals over 60 s observation periods (characteristic return period for lowest elevation angle for CASA radars) spanning a total window of 7.5 min. Each observation period consisted of 2 instantaneous radar scans separated by 60 s. For each observation period, a retrieval was performed for each of nine FG vortex centers arranged in a two-dimensional grid (spacing = 500 m) centered near the true tornado center. Only observations within a circular 1.5 km radius domain centered on each FG vortex center were used. Retrieved wind fields were plotted and compared to the corresponding ARPS fields to determine how well the technique is able to recover the wind field in and near the tornado. However, quantitative comparison between retrieved

and expected (based on subjective inspection of the ARPS wind field) values for the vortex parameters (other than vortex center; see below) was not attempted. There were two reasons why such an evaluation was not undertaken. First, since no mathematically rigorous definition of a tornado exists (see Lugt 1979 for an explanation of the difficulties inherent to defining vortices in general), there is no straightforward objective means of separating "tornadic" flow from "non-tornadic" flow in a complex wind field. Second, the ARPS-simulated tornado does not exactly match the MCRV model and so it would be impossible to assign "true" values to the vortex parameters in these retrievals even if the tornadic flow could somehow be distinguished from the rest of the wind field. Retrieved values of the vortex center (x_0, y_0) could be more confidently assessed based on the ARPS pressure field, as explained in Chapter 3.6.3.

During the 7.5 min period over which the series of 14 retrievals was performed, the ARPS-simulated tornado becomes increasingly intense and distinct from the surrounding flow, though a large portion of the flow surrounding the tornado is nearly as strong as the flow within the tornado vortex core during at least the first half of the test period. The ARPS wind field is considerably more complex than the analytical wind field previously input to the technique, and thus provides a more stringent test of the method. In particular, multiple small-scale vortices are evident at various times in the simulation.

In each of the retrieval periods, at least one of the nine different first-guess retrievals places a tornado-like vortex near the location of the simulated tornado. The result of one such retrieval for the period 110 s – 170 s, during which the ARPS tornado was relatively small, is shown in Fig. 3.7. The retrieved vortex (V_T = 19 m s^{-1}) is located

near the simulated tornado, even though the tornado is only weakly resolved in the emulated Doppler velocity field (Fig. 3.8). In the 200 s – 260 s retrieval experiment, the technique correctly detects both the tornado (not shown) and (using a different first guess vortex center) a vortex-like circulation west of the tornado, even though this latter feature is not very prominent in the ARPS wind field (Fig. 3.9). These results indicate the technique is able to identify intense vortices only subtly evident in radial velocity data. It also highlights the desirability of using multiple first guesses to characterize all vortices within the analysis domain. However, the technique also sometimes retrieves an intense vortex where none is actually present. One of these cases is shown in Fig. 3.10. The location of the retrieved vortex suggests that the local minimum to which the retrieval converged may have resulted from the proximity of the data boundary [this problem was encountered in tests with analytical data (Chapter 3.5.1)]. The same is true for the other three spurious vortices retrieved in these experiments (not shown), all of whose wind fields were potentially significantly truncated by the edge of the analysis domain. Fortunately, tornado-strength winds (if present) associated with these vortices existed over scales that are small relative to the observational resolution (i.e. unresolved features), thereby allowing them to be easily rejected by a simple set of detection criteria (Chapter 3.6.3).

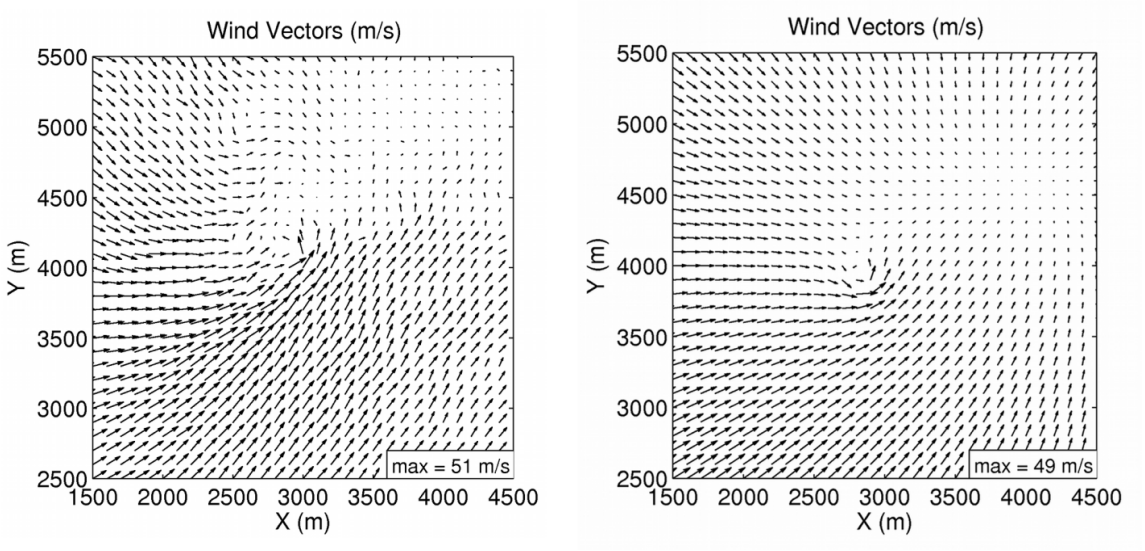

Figure 3.7. ARPS (left) and selected retrieved (right) wind field at t = 110 s. Plot circumscribes analysis domain used for this retrieval. Only every fourth vector plotted for readability.

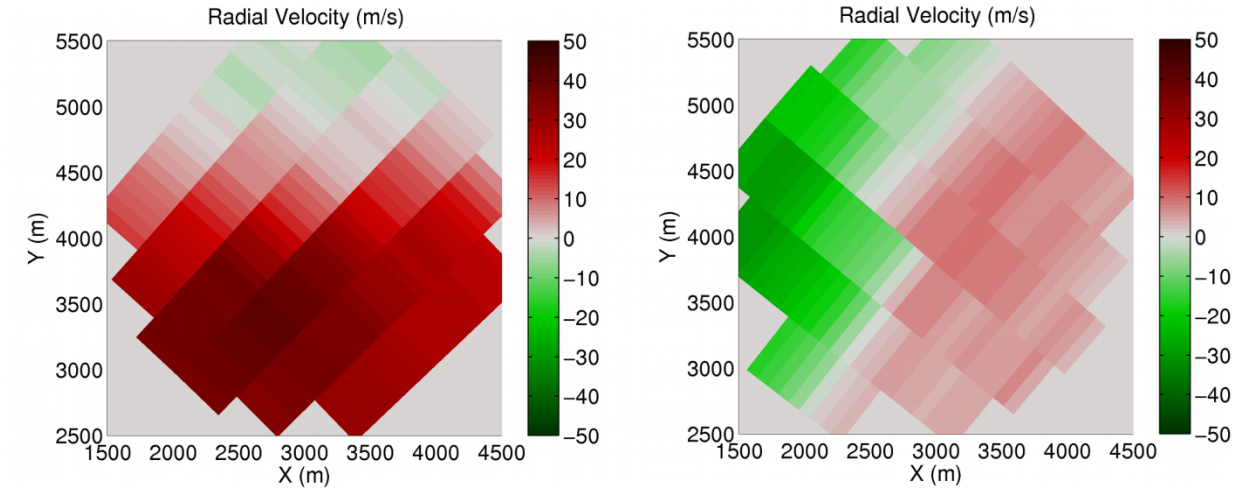

Figure 3.8. Emulated radial velocity observations input to retrieval algorithm for retrieval domain shown in Fig. 3.7. (left) V_r from radar at x = -15 km, y= -15 km; (right) V_r from radar at x = 25 km, y = -15 km.

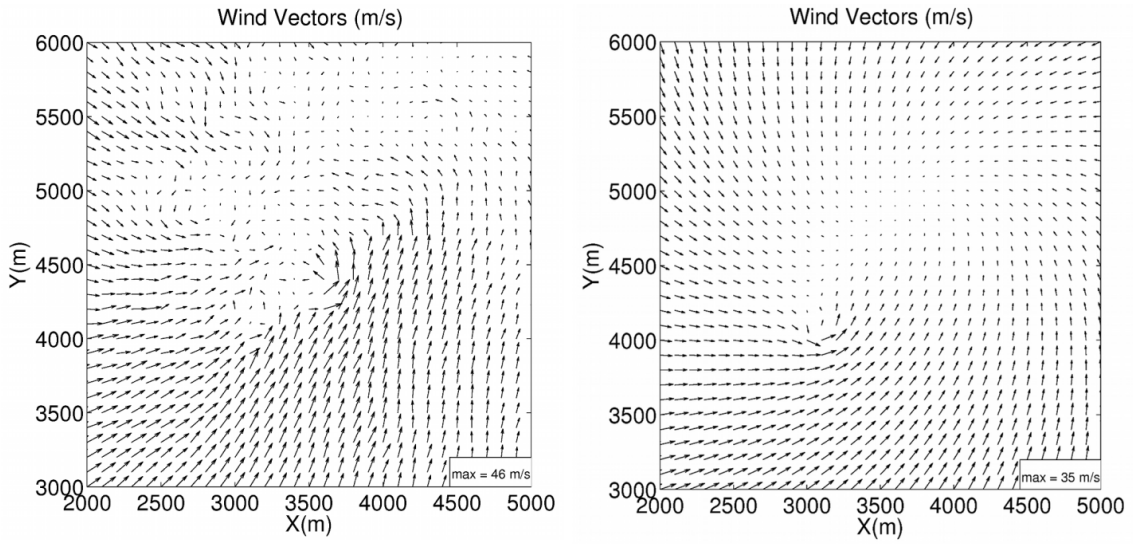

Figure 3.9. As in Fig. 3.7 but for the period from 200s to 260 s.

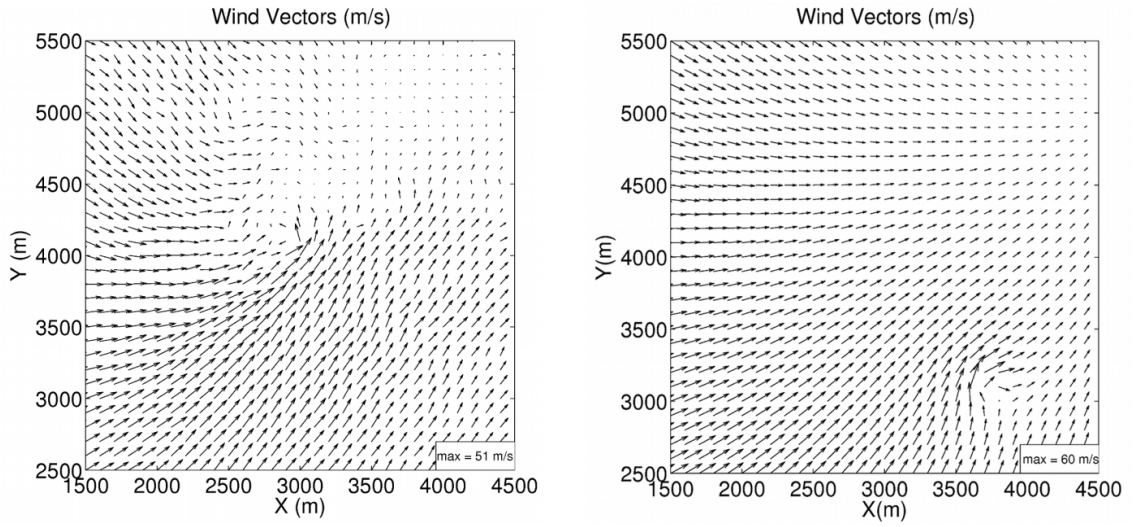

Figure 3.10. As in Fig. 3.7 but for a different FG vortex center.

In the majority of cases where the retrieved vortex is nearly collocated with the ARPS tornado, the retrieved vortex is visually similar to the ARPS tornado on scales ≥ 100 m (those visible in the figures). At later times in the simulation, the larger size of the tornado allows for much of its structure to be recovered. A representative case is shown in Fig. 3.11, along with an illustration of the two-step retrieval procedure used in the

analytical and ARPS experiments. Though the relatively coarse observing resolution precludes reliable retrieval of the tornado inner core in these tests, the technique exhibits skill in retrieving the tornado wind field on radar-grid scales.

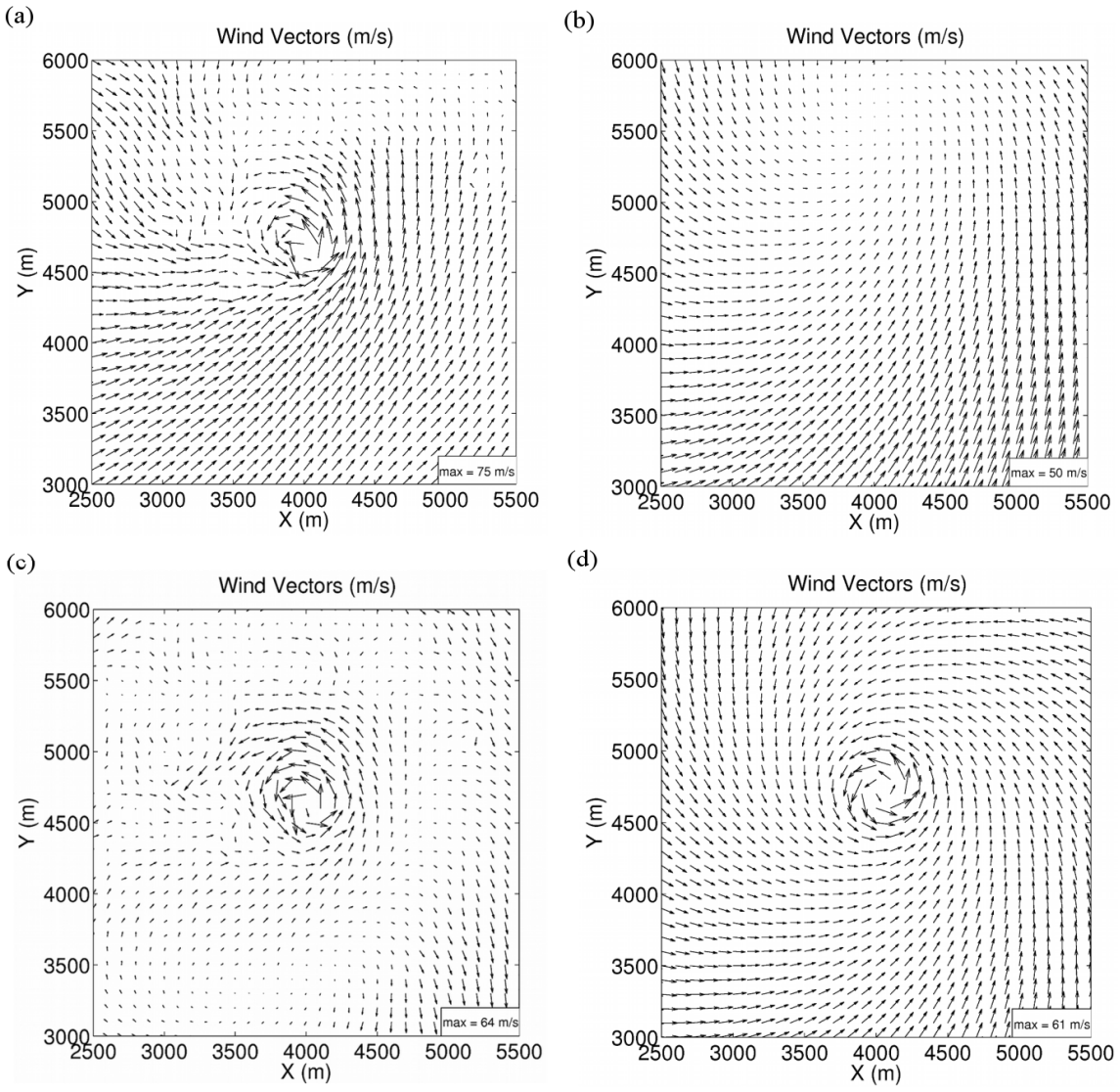

Figure 3.11. Illustration of two-step retrieval procedure, valid at t = 410 s: (a) ARPS wind field, (b) retrieved broadscale flow, (c) the vector difference (a)-(b), and (d) total retrieved flow.

3.6.2 Sensitivity to sampling strategy

Seven sets of 14 experiments were performed to determine the effects of using different analysis domain sizes and radar sampling strategies (Table 3.2). Each set of retrievals used the same starting times and first guess parameter values as in the experiments described in Chapter 3.6.1.

Experiment Set	Analysis Domain Radius	# Radar Scans	Interval Between Scans	Beamwidth/ Sampling Interval	Cross-beam angle	Gate spacing
1	2 km	2	60 s	2°/1°	90 °	100 m
2	1.5 km	3	60 s	2°/1°	90 °	100 m
3	1.5 km	3	20 s	2°/1°	90 °	100 m
4	1.5 km	2	60 s	2°/0.5°	90 °	100 m
5	1.5 km	2	60 s	1°/1°	90 °	100 m
6	1.5 km	2	60 s	2°/1°	45 °	100 m
7	1.5 km	2	60 s	2°/1°	90 °	25 m

Table 3.2. Experiments with different sampling strategies. Each experiment set consists of 14 experiments corresponding to different start times.

Increasing the analysis domain radius from 1.5 km to 2 km reduced the number of successful retrievals (intense vortex retrieved close to ARPS tornado), especially at earlier times when the tornado was weaker. This degradation in the quality of retrievals is likely due to increased violation of the low-order model at larger scales. There are two major reasons for this. First, non-linearity in the broadscale flow is more apparent on larger scales, increasing the potential for errors in the retrieved flow in step 1 of the

algorithm which can then translate into additional errors in the retrieved flow in step 2. Second, larger spatial domains are likely to contain more non-tornadic vortex-like circulations. Of course, an analysis domain which is very small may not encompass enough of the tornado circulation. The use of a 1.5 km domain was a good compromise in these experiments. However, no single domain size will be appropriate in all scenarios, which is why a resizable analysis domain is used in the four-step retrieval procedure adopted in most of the real-data experiments.

Experiments using three rather than two scans from each radar generally led to poorer results at earlier times. This is not surprising since the ARPS tornado evolves rapidly with time while the low-order model assumes that vortex characteristics (except for location) are constant. Observations over a longer period of time are thus more likely to violate the model. In practice, another important benefit of using fewer radar scans would be the reduction in the data collection time required before the technique could be applied and any dangerous vortices detected. Using three scans did not significantly impact the technique's performance in the later periods when the tornado was larger, stronger and not evolving as rapidly.

Using four scans separated by only 20 s (compared to 60 s in the previous experiment) produced slightly improved retrievals for the earlier periods, but did not produce noticeably better results when the tornado was larger and more intense. Surprisingly, decreasing the beamwidth, azimuthal sampling interval or range resolution also did not noticeably improve the retrievals. This suggests that the greater limitation to the technique in the ARPS-data experiments was imposed by the simplicity of the low-

order model (failure to capture the complexity of the ARPS-simulated tornado structure), and not by the coarseness of the observations.

Decreasing the radar cross-beam angle to 45° while keeping the radar-tornado distances roughly the same significantly reduced the number of retrievals (within each set of experiments with different first guess vortex locations) in which an intense vortex was recovered very near the location of the tornado. However, at least one successful retrieval was obtained for each retrieval period except for 140 s – 200 s, indicating that less ideal cross-beam angles may not unduly hinder the technique if multiple first guesses are used.

3.6.3 Application of detection criteria

In cases where the ARPS tornado was large relative to the radar grid scale, both the inner core and outer region of the vortex were well-retrieved by the technique (e.g. Fig. 3.11). These results suggest that the technique yields reasonable estimates of R and V_T when the tornado is well-resolved. As described in Chapter 2.5, in real-data tests, whether the vortex is sufficiently well-resolved for these parameters to be reliable is determined through validation with the observed radial velocity field. In the ARPS experiments, however, a less rigorous detection criterion was used. In order for a detection to be made, the retrieved vortex radius of tangential 35 m s^{-1} wind,

$$R_{35} = R\left(\frac{V_T}{35\,\mathrm{ms}^{-1}}\right)^{1/\alpha},$$

was required to exceed 100 m. The above formula is valid outside of the vortex core (region of solid body rotation). The 100 m threshold is simply the smaller of the two radar sampling intervals (in this case, 100 m in range and ~500 m in azimuth). It is most

appropriate in cases where the cross-beam angle is nearly 90°, since observations are consequently spaced every 100 m in two roughly perpendicular directions. This condition is satisfied in all of the experiments in this section.

For each of the fourteen retrieval periods, retrieved vortices which did not pass this detection criterion were discarded. The mean retrieved vortex center was then calculated from the vortices which did pass the detection criterion for each period. The mean retrieved vortex path was then compared to the ARPS tornado path as determined from the minimum in the ARPS pressure field near the height where observations were taken.

Using the R_{35} detection criterion, all of the retrieved vortices for the two earliest retrieval periods (110 s – 170 s and 140 s – 200 s) were rejected. Visual inspection of the 25 m ARPS wind vector plots (not shown) during these early time periods showed that the ARPS tornado would be irresolvable on the observation grid (R < 75 m). Fortunately, the tornado was correctly detected in each of the remaining twelve retrieval periods. In the majority of these cases, the tornado was detected in several of the nine retrievals, indicating the technique was not unduly sensitive to error in the first guess vortex center (Table 3.3). Moreover, no spurious vortices (such as the one depicted in Fig. 3.10) passed the detection criterion during these times. For these twelve retrieval periods, the retrieved tornado path closely matches the ARPS pressure-estimated path (Fig. 3.12). The average (over the twelve retrieval periods) displacement between the two paths is only ~120 m, an encouraging result given the observational resolution in these experiments.

Retrieval Period	Number of Detections
170 s – 230 s	1
200 s – 260 s	2
230 s – 290 s	5
260 s – 320 s	3
290 s – 350 s	3
320 s – 380 s	6
350 s – 410 s	6
380 s – 440 s	6
410 s – 470 s	7
440 s – 500 s	7
470 s – 530 s	6
500 s – 560 s	6

Table 3.3. Number of tornado detections (out of nine retrievals) made in each of the ARPS experiments.

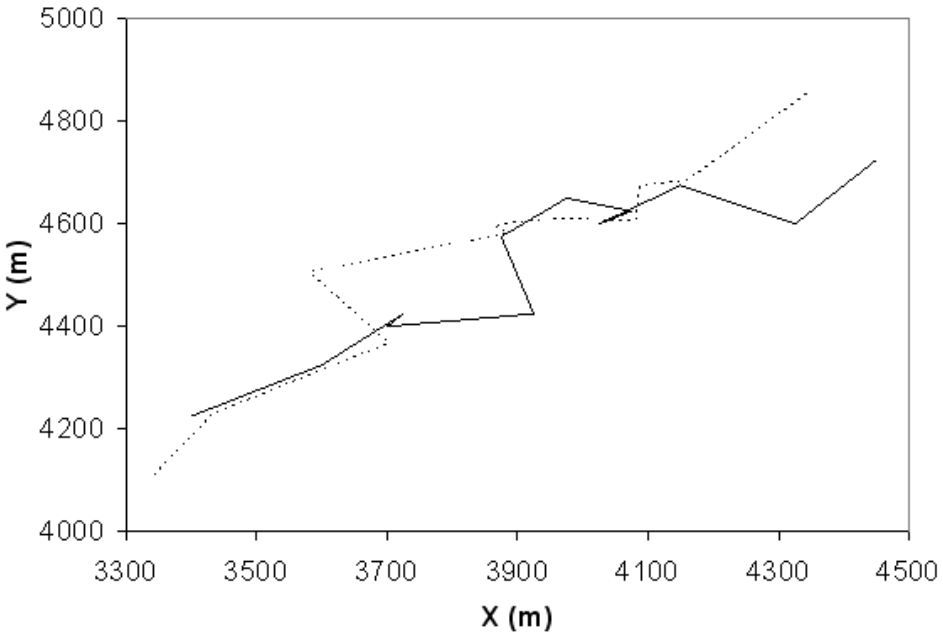

Figure 3.12. ARPS-estimated tornado path (solid) and retrieved vortex path (dotted) for the period from 170 s to 500 s.

3.7 Summary of OSSE Results

The low-order technique was initially tested with two kinds of idealized wind fields: (i) analytically-generated vortices with surrounding broadscale flow, and (ii) ARPS-simulated wind observations of a tornado-like vortex and its near-environment. The technique demonstrated skill in detecting intense vortices, even when embedded within complex flow, as well as in retrieving the vortex wind field on scales greater than or equal to that of the radar grid.

It was found that spurious minima can pose a serious threat to the algorithm's ability to converge to the desired minimum, especially when the first guess model parameters (particularly the location of the vortex center) contain significant error. Boundary minima in $J(x_0, y_0)$ can occur near the edge of the analysis domain, and local minima can occur in other multi-dimensional cross-sections of J due to regions of missing data or deviations of the observed wind pattern from that described by the low-order model. An important special case of such a deviation is the presence of multiple vortices in the data. This local minima problem necessitates the use of multiple first guesses for the location of the vortex and of a multiple-step approach in which much of the larger-scale flow is retrieved and subtracted before a small-scale vortex retrieval is performed. The latter strategy is necessary in cases where a weaker and broader vortex-like circulation is present and provides a better fit to the low-order model than a collocated (real) intense vortex. The most challenging multiple minima problem is the vortex parameter non-uniqueness which occurs when the inner vortex core is not well-resolved. In such cases, a larger, weaker vortex may be retrieved as a stronger, narrower (more tornado-like) vortex or vice versa. This problem was accounted for by requiring

that the retrieved radius of intense vortex winds be “resolvable” in order for a retrieved vortex to be classified as a tornado.

CHAPTER 4: EXPERIMENTS WITH REAL RADAR DATA

Having identified and mitigated weaknesses of the technique in tests with analytical and numerically-simulated vortices, the technique was further tested and refined using real dual-Doppler observations of small-scale vortices from several different radar platforms. In addition, the ability of the technique to detect and characterize larger-scale (> 1 km diameter) vortices such as mesocyclones was examined using both single- and dual-Doppler data.

The first guess model parameter values were set to zero in the real-data tests, except for R (=200 m in the default retrieval configuration and =1000 m in "mesocyclone retrieval mode", introduced later), α and β (=0.7), and x_0 and y_0 (determined, as before, by the locations of the analysis domains).

4.1 WSR-88D/TDWR Observations of 8 May 2003 OKC Tornado

4.1.1 Description of dataset

The technique was tested using real dual-Doppler data from the 8 May 2003 supercell that produced a long-lived F4 tornado in the southern portion of the Oklahoma City, Oklahoma metropolitan area. The tornado remained within the dual-Doppler domain of the KOKC (a Terminal Doppler Weather Radar) and KTLX radars (characteristics of both radars are listed in Table 4.1) throughout its lifetime, during which 0.5° elevation reflectivity and radial velocity scans were performed every ~5 min by KTLX and every ~1 min by KOKC. The tornado damage path and relative locations of KOKC and KTLX are depicted in Figure 4.1. A set of retrieval experiments was

performed using data from five consecutive 0.5° KTLX scans along with one 0.5° KOKC scan taken within ~30-60 s of each KTLX scan. The cross-beam angle in these experiments was least favorable (most acute) when the observed tornado is weakest, thereby presenting a notable challenge to the technique. All velocity data used in the experiments were subjectively de-aliased and quality-controlled by Katherine Donner (M.S. student; see Donner et al. 2007 for details). The proximity of the tornado to both radars (11-26 km) allowed observations to be collected at an azimuthal resolution characteristic of a CASA network. However, the range resolution of the velocity data (150 m and 250 m) is coarser than that for a CASA radar (~50-100 m), and so the retrievals obtained in these experiments are presumably representative of, or somewhat poorer than, those which would have been obtained had the tornado been sampled by a network of CASA radars.

	Doppler Band	**Beamwidth**	**Azimuthal Sampling**	**Range Sampling (Doppler velocity)**
KTLX	S	0.95°	1.0°	250 m
KOKC	C	1.0°	1.0°	150 m

Table 4.1. Selected characteristics of the KOKC and KTLX radars.

4.1.2 Experimental Details

As described in Section 2.3, the first guesses for the vortex center were objectively determined using a set of criteria for identifying regions containing strong rotation (hereafter referred to as the "domain-selection criteria"). A gate-to-gate azimuthal shear criterion of .05 s^{-1} was used, and the radial velocity was required to exceed 25 m s^{-1} in one or both gates. The radius of each analysis domain was set to 1.5

km. In later real-data experiments (presented below), a 2-km domain radius was used in order to better accommodate larger vortices. In these and in most of the real-data experiments following this section, only a single plan position indicator (PPI) scan (not two scans as in the analytical and ARPS experiments) from each radar was used in the retrievals. The tradeoffs associated with using one vs. two scans from each radar are discussed in Section 5.

Similar to the ARPS experiments (Section 3.6), the primary detection criterion in the 8 May 2003 experiments required that $R_{30} > 200$ m, with 200 m being the shorter of the two mean radar sampling intervals. In preliminary experiments with this dataset (not shown), spurious vortices were occasionally retrieved when the real vortex was located near the edge of the analysis domain (see Section 3.5.1). Therefore, in the 8 May 2003 experiments described below, retrievals were rejected if the magnitude of the retrieved vortex wind $\left(=\sqrt{v_r^2+v_\theta^2}\right)$ exceeded 20 m s^{-1} at the edge of the analysis domain. In addition, detections were rejected if $\alpha > 1.0$ in these experiments; this criterion was motivated by the occasional retrieval of spurious vortices having unrealistically large (> 1.0) values of α. Such a rapid decline in v_θ with distance from the vortex center violates the Rayleigh (1916) instability condition and therefore may not be sustainable in actual tornadoes. This hypothesis is supported by high-resolution observational studies of tornadoes (e.g. Wurman and Gill 2000; Lee and Wurman 2005; Wurman and Alexander 2005) which have found that α typically varies between 0.6 and 0.8. Fortunately, the rather ad hoc detection criteria used in the 8 May 2003 and ARPS experiments were replaced in subsequent experiments with the more appropriate criteria described in Section 2.5. One reason this improvement was so critical is that the retrieved α often did

exceed 1.0 in later experiments, presumably due to the vortex solution non-uniqueness problem and not to violation of the Rayleigh instability condition.

4.1.3 Retrieval Results

The technique successfully detected the tornado during all five observational periods (Table 4.2), which together spanned most of the tornado's lifetime. Only a single region was selected by the algorithm for retrievals at each time. No false detections were made. The mean distance between the vortex centers retrieved during each observational period (excluding the last period, during which only one detection was made) ranged from 57 m to 201 m, indicating that the technique was not unduly sensitive to errors in the first guess vortex center.

Retrieval Period	Number of Detections
# 1	5
# 2	4
# 3	4
# 4	3
# 5	1

Table 4.2. Number of tornado detections (out of nine retrievals) made in each of the 8 May 2003 experiments.

Though direct comparison of the mean retrieved vortex centers and R_{30} values to the observed damage path (Figure 4.1) is hindered by several issues, most notably that the analysis domains in these experiments are ~ 100-220 m above the ground and the true R_{30} cannot be reliably inferred from the F-rating contours, the results are nevertheless encouraging. The mean retrieved vortex centers are all very nearly collocated with the

observed tornado damage path. The mean retrieved R_{30} for each of the experiments are (in chronological order) 248 m, 296 m, 318 m, 265 m and 307 m, consistent with the surveyed maximum damage path width of ~ 650 m (NCDC 2010a). The trend of R_{30} is similar to that of the damage path during the first four observational periods, while the fifth estimate is too large.

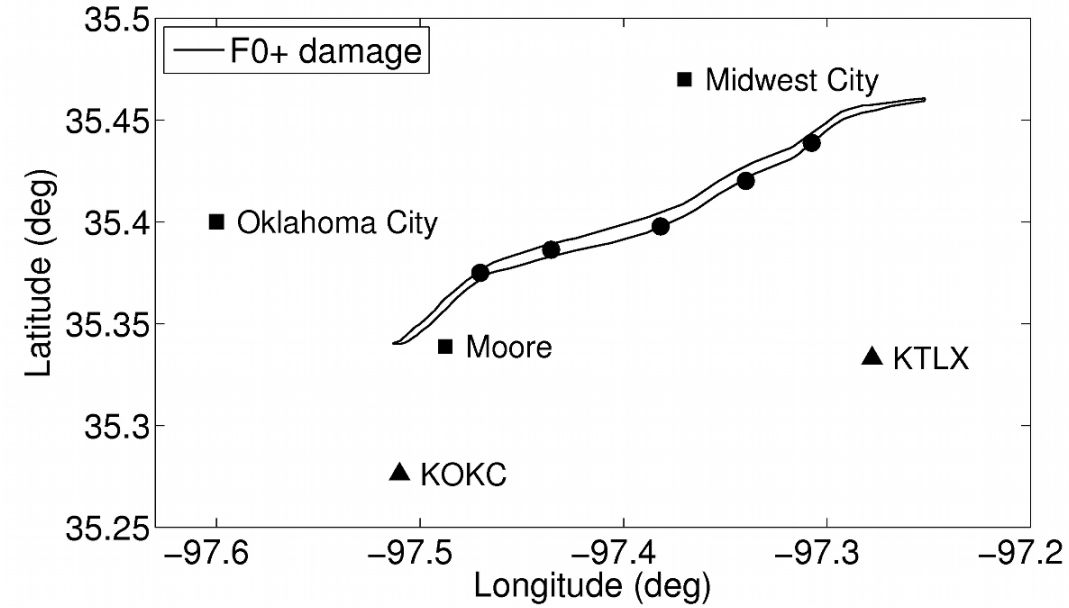

Figure 4.1. Location of the 8 May 2003 tornado damage path (F0+) relative to KTLX and KOKC. Dots indicate the tornado locations retrieved by the technique.

In order to assess how well the low-order model was able to reproduce the complexity of the input radial velocity fields, the radial component of the mean retrieved wind field was compared to the observed radial wind field within the central analysis domain in each experiment for each radar. A representative comparison (retrieval period # 3) is shown in Figure 4.2. Naturally, the low-order model is unable to completely recover the intricate structure of the near-tornado radial wind field. However, the retrieved wind field does reasonably capture the primary structure of the tornado, at least on the scale of the observational data.

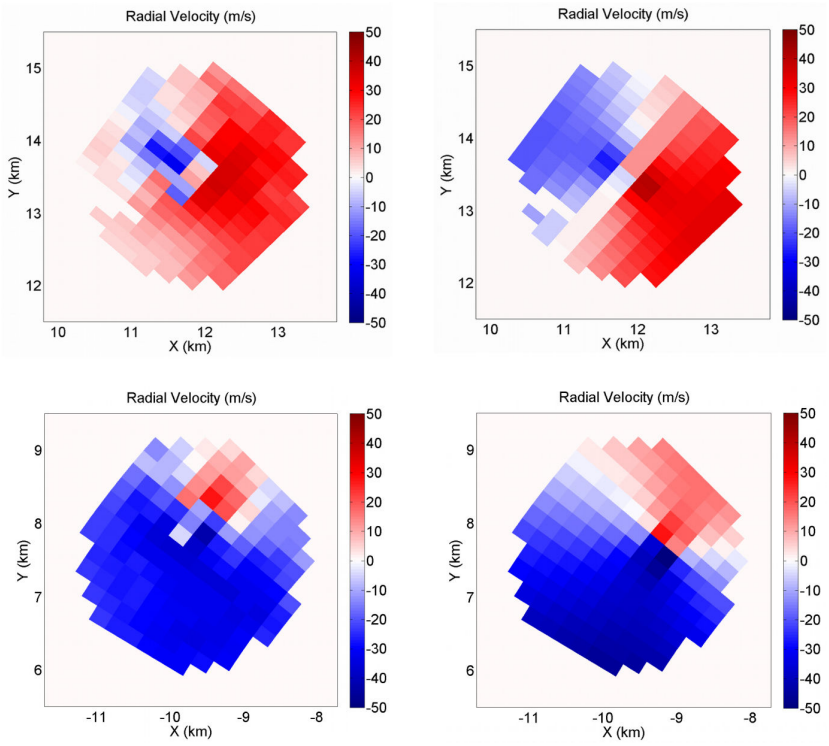

Figure 4.2. KTLX (top panels) and KOKC (bottom panels) observed (left panels) vs. retrieved (right panels) radial velocities.

4.2 SMART Radar Observations of 29 May 2004 Geary, OK Tornado

4.2.1 Description of Dataset

A supercell that spawned a series of tornadoes across Oklahoma during the evening of 29 May 2004 was observed by a pair of Shared Mobile Atmospheric Research and Teaching (SMART; Biggerstaff et al. 2005) radars near Geary and Calumet, OK. The technique was tested using data collected by the two SMART radars (SMART Radar 1, or SR1 and SMART Radar 2, or SR2) and de-aliased and quality-controlled by Kristin Kuhlman. More specifically, the base elevation (0.5°) scans from five consecutive coordinated pairs of volume scans beginning at 0022 Z, 0027 Z, 0033 Z, 0038 Z and

0052 Z were used. The range and azimuthal sampling intervals for both radars were approximately 67 m and 1°, respectively. The half-power beamwidth was about 1.5°. The distance between each of the radars and the analysis domains varied between ~20 km and ~50 km in these tests, yielding azimuthal sampling intervals of between ~350 m and ~850 m. In these and all following experiments, the four-step retrieval procedure described in Section 2.4 was used. Thus, in cases where an intense vortex was preliminarily detected, the center of the analysis domain was relocated to the position of the retrieved vortex, and the radius of the analysis domain (initially 2 km) used for the final vortex retrieval was decreased if the vortex was relatively small.

A very large, 1-2 km diameter tornado produced F-2 damage throughout the experimental period (NCDC 2010b). Several smaller vortices (≤ 1 km core diameter) formed and decayed within the tornado during the SMART radar observing period. These vortices are indicated in the individual radars' wind fields by regions of enhanced shear. However, the strongest measured winds occurred outside of these vortices. Since the smaller-scale vortices are not readily visually discernable from the surrounding mesoscale vortex flow, this is a useful test case for our algorithm. The existence of these smaller vortices is confirmed by the presence of intense shear and reflectivity holes (or "eyes") in higher-resolution Doppler-On-Wheels (DOW; Wurman et al. 1997) observations of this case (selected images available at http://www.cswr.org/dataimages/rotate/geary-summary-2004-0711fp.pdf). Which of these vortices (if any) actually extended to the surface as tornadoes is unknown. However, that is not important here. The goal of these experiments is to verify that the

technique is capable of detecting and characterizing intense small-scale vortices in radar data, especially when they are embedded within a larger-scale vortex.

4.2.2 Retrieval Results

The domain-selection criteria used in these experiments (Section 2.3) required that the difference in radial wind speed between the two radar gates exceed 15 m s^{-1} and that the radial wind speed and reflectivity exceed 15 m s^{-1} and 20 dBZ (respectively) in at least one radar gate within 3 km of the gate pair centroid. These criteria worked well at all five analysis times. All of the small-scale vortices evident within the mesoscale circulation were contained within one or more of the identified regions, and the numbers of identified regions were not prohibitively high, varying between 4 and 12 per analysis time.

The detection threshold V_{det} was set to 20 m s^{-1} in these experiments. In all cases where a detection occurred, the existence of an intense vortex was supported by both the similarity of the retrieved vortex wind field to the residual (observed minus retrieved broadscale) wind field, and the resemblance of the total retrieved wind field to the observed radial velocity fields. Plots of the DOW velocity and reflectivity data further corroborated the existence of these vortices.

Since forecasters must synthesize large amounts of information during severe weather operations, it may be prudent to have vortex detection/characterization algorithms output mean vortex characteristic estimates from each set of detections likely corresponding to the same vortex (e.g. located within 500 m of one another), rather than estimates from each individual retrieval. Thus, the ensemble (calculated over all retrievals passing the detection criteria) means of the most important retrieved vortex

characteristics were computed at each analysis time in these tests (Table 4.3). In order to evaluate how well the mean retrieved vortex characteristics represent the actual vortex in each case, the radial component of the final (not provisional) retrieval most closely approximating the ensemble mean retrieval for each analysis time was plotted and compared to the observed radial velocity field (Figures 4.3-4.7). In all five cases, the broadscale portion of the model, though linear, recovered the larger-scale (parent vortex) circulation sufficiently well that the embedded vortices were salient in the residual flow (see Appendix). The vortex itself was subsequently accurately retrieved, at least on observed scales.

Table 4.3. Means of retrieved vortex characteristics for each set of 29 May 2004 retrievals from SMART-Radar data. Sample sizes (n) are given below each time.

Time (Z)	**Distance from ensemble mean vortex center (m)**	**Movement (m s^{-1})**	**Heading (° clockwise from east)**	**V_T (m s^{-1})**	**V_T^{res} (m s^{-1})**	**V_R (m s^{-1})**	**R (m)**	**R_{20} (m)**	**α**
0022 (n=4)	78	29	-33	28	21	-20	393	555	1.4
0027 (n=17)	81	9	-46	40	20	1	223	519	0.8
0033 (n=18)	80	15	28	62	33	-13	369	845	1.4
0038 (n=9)	133	11	-70	50	20	1	332	684	1.3
0052 (n=29)	90	8	31	73	36	0	264	986	1.0

Table 4.4. Standard deviations of retrieved vortex characteristics for each set of 29 May 2004 retrievals from SMART-Radar data. Asterisked values indicate standard deviations that have been recomputed upon removing an extreme outlier.

Time (Z)	Distance from ensemble mean vortex center (m)	Movement (m s^{-1})	Heading (° clockwise from east)	V_T (m s^{-1})	V_T^{res} (m s^{-1})	V_R (m s^{-1})	R (m)	R_{20} (m)	α
0022 (n=4)	57	5	3	3	3	3	166	133	0.8
0027 (n=17)	101 (55*)	6	26	6	0	2	44	88	0.2
0033 (n=18)	55	6	40 (19*)	7	2	6	69	72	0.4
0038 (n=9)	81	4	27	4	0	1	174	139	0.7
0052 (n=29)	52	4	98	9	2	2	75	87	0.3

Though the "true" values of R_{20}, V_T, and other vortex characteristics cannot be precisely determined (and will not even be well-defined in some cases, e.g. elliptical vortices), the retrieved values of these parameters can be qualitatively evaluated through comparison of the retrieved and observed wind fields. In all five cases, the observed and retrieved total radial velocity fields are reasonably similar to one another, as are the residual and retrieved vortex radial velocity fields. The mean R_{20} is largest for the 0033 Z and 0052 Z analyses, which appear to contain the two largest vortices out of the five analysis times. In addition, the fact that the observed radial velocities in these vortices are stronger than in the other vortices is represented in the higher mean value of V_T^{res} (33 and 36 m s^{-1}, respectively) in these cases. It is also encouraging that the retrievals capture the strong convergence indicated in the radial wind observation fields at 0022 Z (most evident at x = 2.25 km, y = 19 km in Figure 4.3b) and 0033 Z (most evident at x = -33 km, y = 23.5 km in Figure 4.6a).

The standard deviations in the retrieved vortex characteristics were also calculated to quantify the uncertainty in these estimates (Table 4.4). These indicate that while the uncertainty in the retrieved vortex center is small at each analysis time, the uncertainty in the vortex translational velocity was occasionally significant. This is partly because the vortices do not move very far relative to the uncertainty in their initial and final positions (see Section 3.5.5). Using longer inter-scan intervals likely would not improve the (u_v, v_v) retrieval in this case given the long return period between scans (~5 min) and the fact that vortices were continually forming and dissipating in close proximity to each other. The higher temporal resolution afforded by a CASA-like radar system would make this approach to improving (u_v, v_v) more feasible, but at a cost (see Section 5). Table 4.4 also shows that the uncertainty tends to be significantly larger in the vortex model parameters (V_T, α and R) than in the quantities derived from them (e.g. R_{20} and V_T^{res}). Thus, the proposed solution to the vortex solution non-uniqueness problem (Section 2.5) appears to work well in these tests.

As reflected in Table 4.3, α significantly exceeded 1.0 in many of the retrievals. In fact, α exceeded 2.0 in two retrievals and 3.0 in an additional retrieval. In each of those cases, R was significantly greater than the ensemble mean R, while V_T and R_{20} were very close to their ensemble means. Consistent with this result, the retrieved wind fields for cases with $\alpha > 2$ (not shown) were visually quite similar to those for $\alpha \leq 1.0$. These findings indicate that relatively coarse observational resolution was creating solution non-uniqueness in R and α. Since α is evidently highly subject to the same type of multiple minima problem as are R and V_T, it would be imprudent to impose thresholds on α in the detection criteria. In the remaining real-data cases considered in this section, vortices

were better resolved by the observations, and so values of α were much more reasonable (did not exceed 1.4).

Figure 4.3. Clockwise from top left: observed, residual (observed minus retrieved broadscale), retrieved vortex, and retrieved total radial velocity fields at 0022 Z for (a) SR1 and (b) SR2. The axes indicate *x*- and *y*-displacements from the radar.

(a)

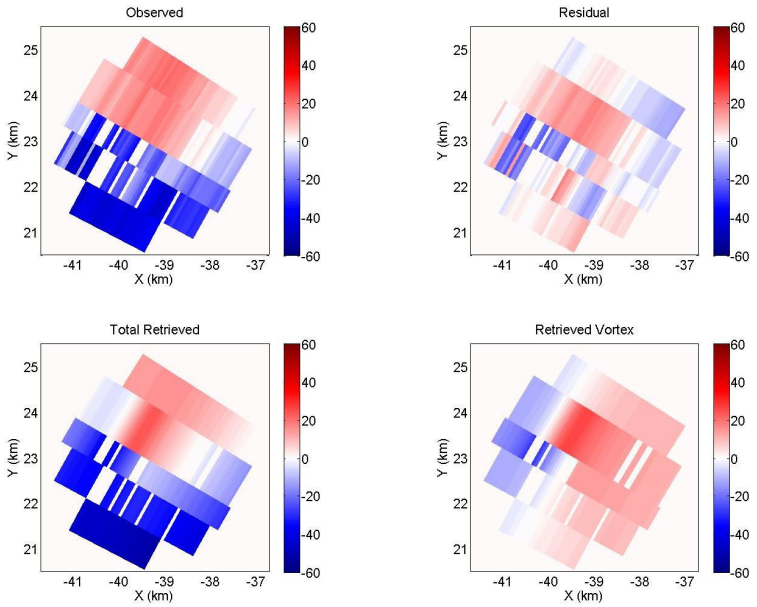

(b)

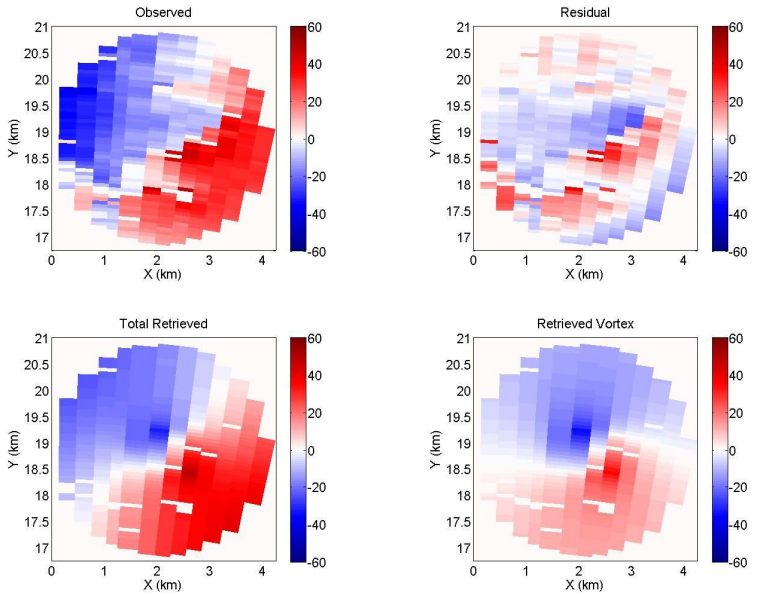

Figure 4.4. Same as Fig. 4.3 except at 0027 Z.

(a)

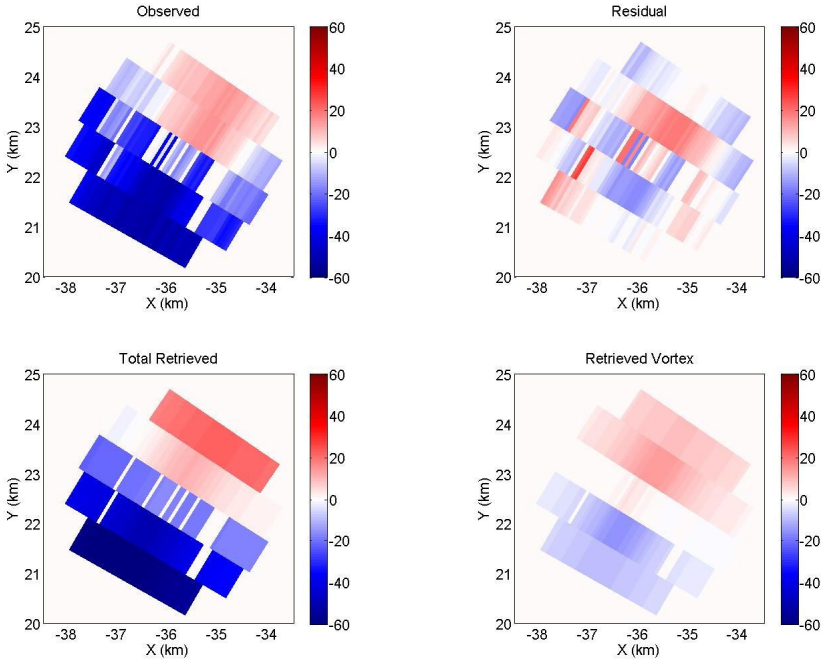

(b)

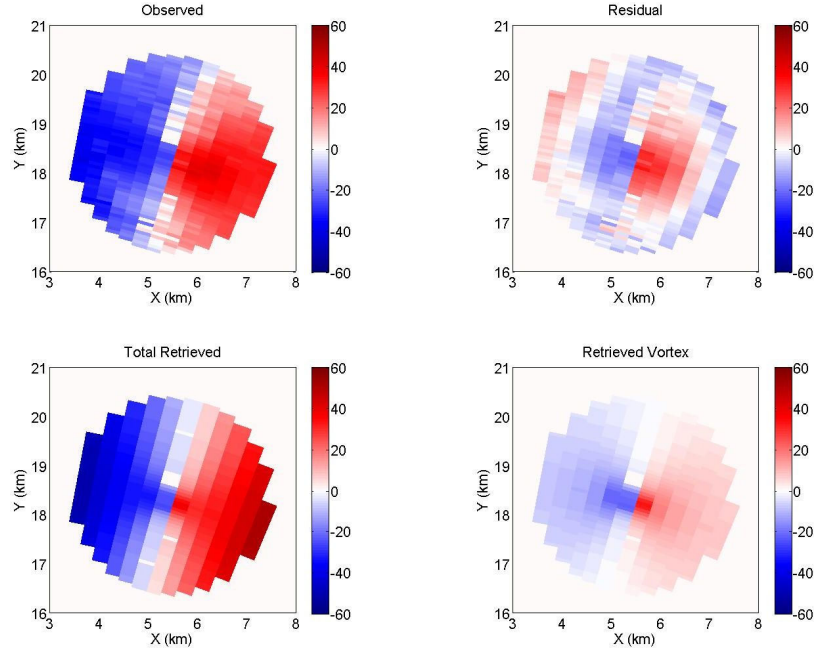

Figure 4.5. Same as Fig. 4.3 except at 0033 Z.

(a)

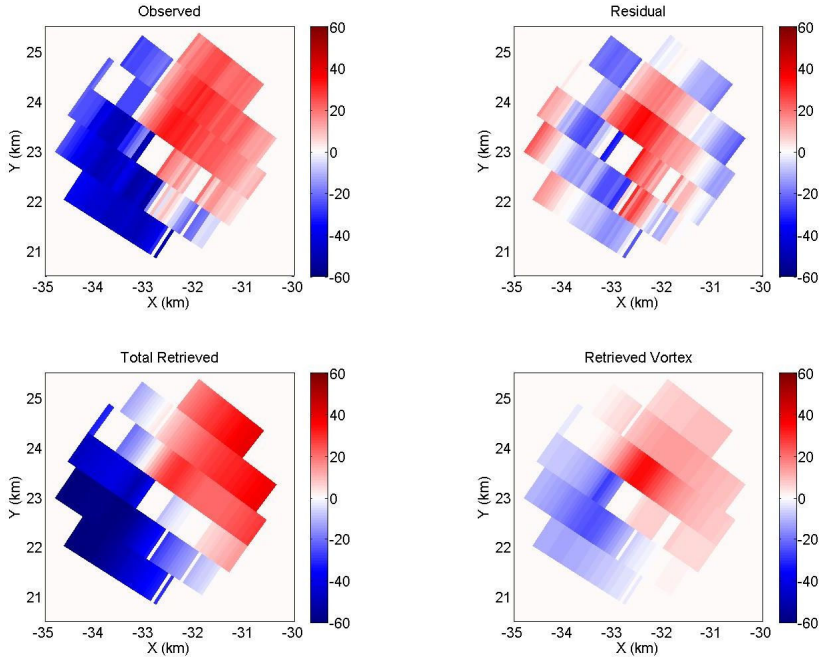

(b)

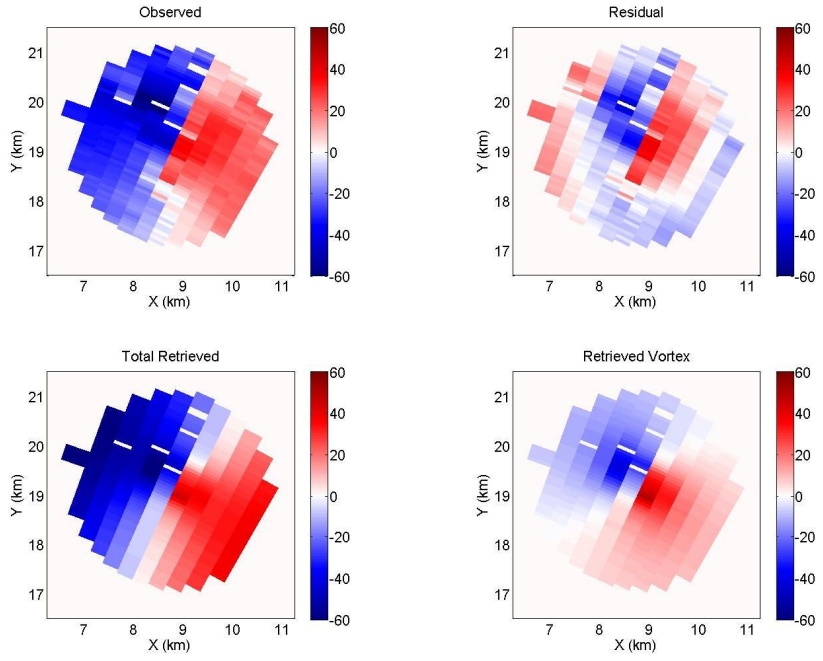

Figure 4.6. Same as Fig. 4.3 except at 0038 Z.

(a)

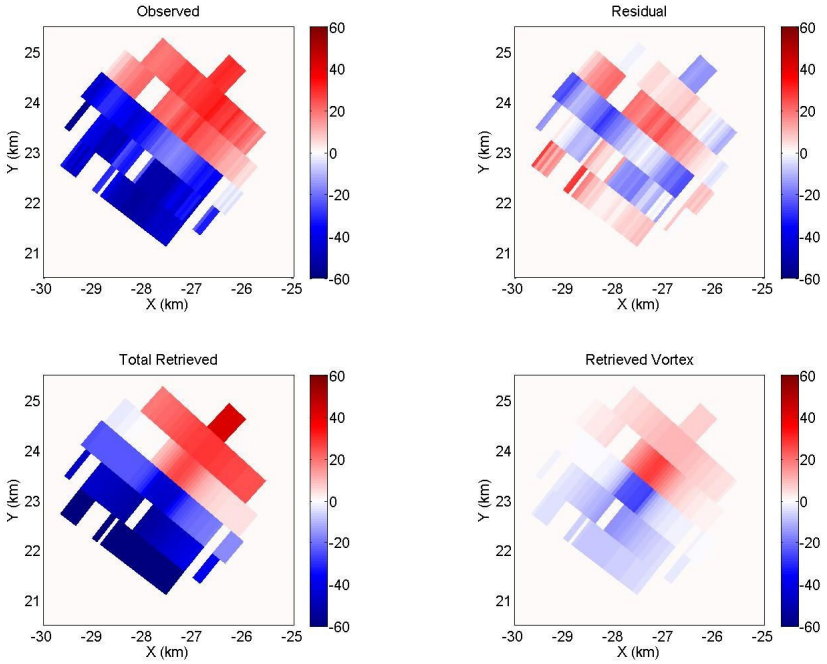

(b)

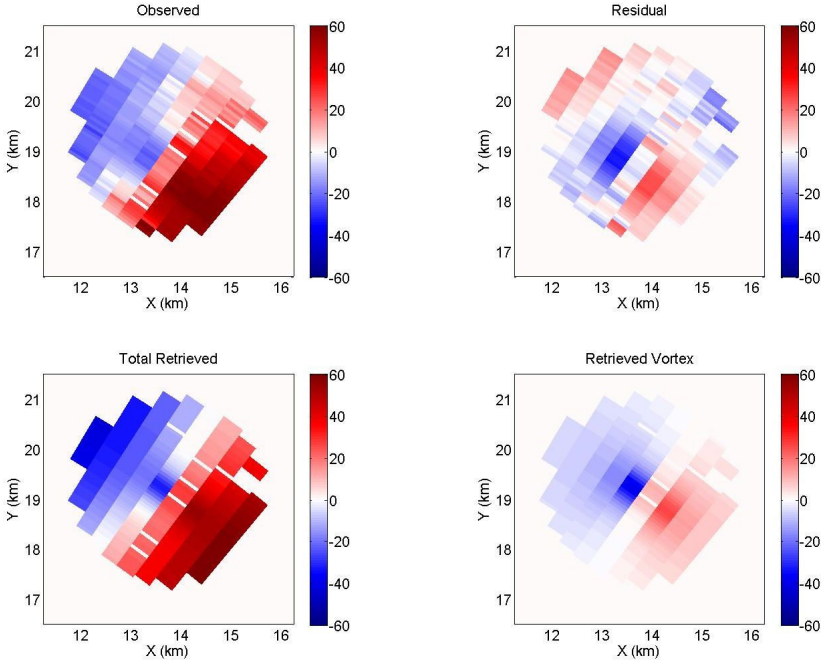

Figure 4.7. Same as Fig. 4.3 except at 0052 Z.

(a)

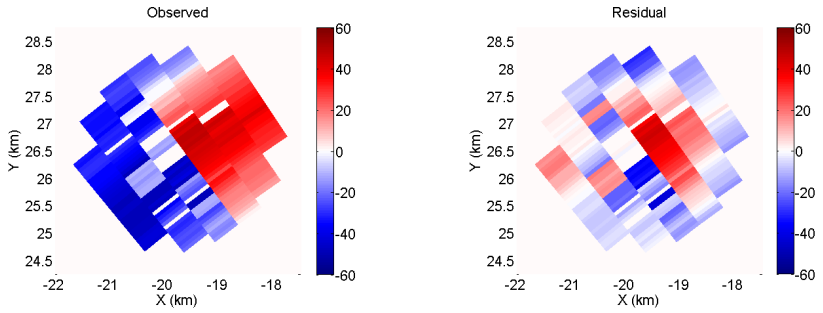

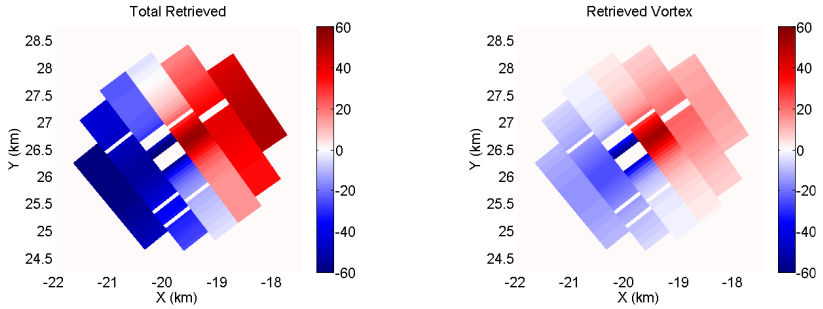

(b)

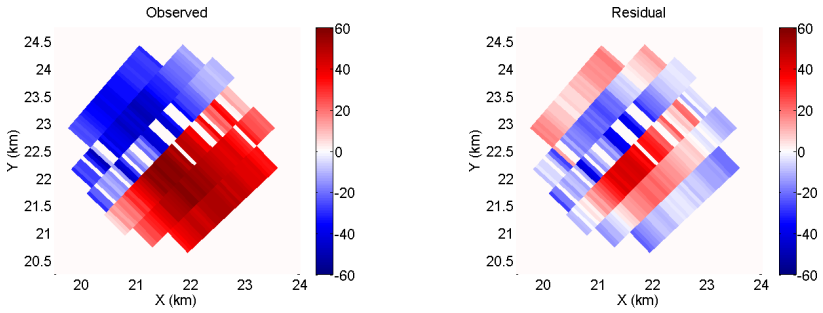

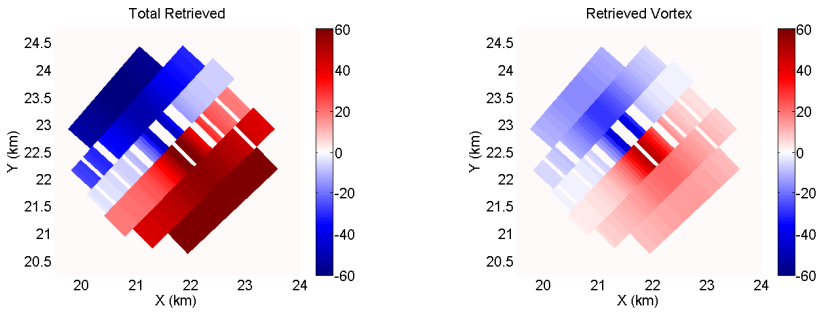

4.3 DOW Observations of 5 June 2001 Attica, KS Tornado

4.3.1 Description of Dataset

The technique was next applied to a dual-DOW dataset of a tornado that occurred near Attica, KS on 5 June 2001. Due to the presence of intervening precipitation, the tornado was not visually observed by the DOW team, and so the precise time period(s) during which the tornado occurred is unknown. The peak intensity of the tornado is also uncertain since no damage survey was performed. The tornado was estimated by a sheriff to be around 100 m in diameter (NCDC 2010c), though it is possible the tornado widened and/or narrowed during times in which it was not observed. The azimuthal sampling interval for both DOW radars averaged less than 0.4° and the radial sampling interval varied between 50 m and 75 m. The azimuthal distance between observations near the tornado averaged around 50 m. The half-power beamwidth was 0.95°.

The technique was applied to a single pair of radial velocity PPIs for seven consecutive coordinated pairs of volume scans performed between 0028 Z and 0035 Z. Each pair of PPIs was selected such that the heights of the radar beams were within 100 m of each other in the vicinity of the circulation associated with the tornado. The heights of the PPIs near the circulation were typically ~ 100-150 m AGL. In all cases, the radars observed the circulation within 10 s of one another.

4.3.2 Retrieval Results

The same domain-selection criteria used in the 29 May 2004 experiments (Section 4.2) were used here, except with the additional requirement that gate-to-gate shear exceed .05 s^{-1}. Without this requirement, the number of identified radar gate pairs would have

been much larger, due partly to the very high observational resolution in these experiments. The resulting additional processing would be highly undesirable during real-time operations. This indicates that the optimal domain-selection criteria are dependent not only on the scales of the vortices to be detected but also on the characteristics of the radar network.

The detection threshold V_{det} was set to 10 m s^{-1} in these experiments, which is half of the value used in the 29 May 2004 experiments. As with the domain-selection criteria, the most appropriate value of V_{det} is dependent upon the radar network and the types of vortices being sought. (In both cases, computational wall clock time must also be considered for operational application; see Section 5). At each of the analysis times, the technique detected the smallest intense vortex that could be subjectively inferred from the observed radial velocity fields. For several of the time periods, the algorithm identified and performed retrievals within regions that, based on visual examination of the radial velocity observations, contained strong shear but no intense vortices. Fortunately, no vortices with resolved tangential winds > 10 m s^{-1} were identified other than those inferred from the radar data. Between two and six regions were identified for each time period except 0032 Z, for which 13 regions were selected for retrievals.

Comparisons of the observed and final retrieved radial wind fields for selected time periods are presented in Figs. 4.8-4.11. Two separate small-scale vortices are apparent at 0028 Z. The more northern vortex is the (possibly developing) tornado. Fortunately, both vortices were detected by the technique (Figs. 4.8 and 4.9). The use of a modifiable (in particular, shrinkable) domain in steps 3 and 4 of the retrieval procedure was critical to detecting the smallest-scale vortex in some cases. This is because the

residual wind field at the end of step 1 was often dominated by a circulation intermediate in size between the smallest vortex and that retrieved (and subtracted) by the broadscale model parameters.

The means and standard deviations of the retrieved tornado characteristics are shown in Tables 4.5 and 4.6. As in the 29 May 2004 experiments, there is little spread in the retrieved vortex center, V_T^{res} and R_n among the detections for each period. Due to the very high resolution afforded by the DOWs, the vortices are better resolved and so there is also less variance in V_T and R. The values and trends in all these vortex characteristics are consistent with the observed radial wind fields. For example, the mean retrieved V_T^{res} for the tornado was 10 m s^{-1}, 11 m s^{-1} and 18 m s^{-1} at 0028 Z, 0031 Z and 0032 Z, respectively. The corresponding mean R and R_{10} were (66 m, 165 m, 75 m) and (167 m, 216 m, 320 m), respectively.

Despite the very short periods between scans used in each experiment, the (u_v, v_v) parameters were retrieved reasonably well (based on visual estimation of the vortex center at consecutive times) when the retrieved vortex had $R < 100$ m. Consistent with the 29 May 2004 experiments, however, the variance in (u_v, v_v) in the present experiments increased when a larger vortex was detected due to the associated difficulty in retrieving the vortex center. Since the larger vortices retrieved in these experiments were relatively well-resolved, the difficulty in retrieving their precise locations may be more attributable to the complexity of the wind field (i.e. violations of the low-order model) than to the finite observational resolution.

Additional retrievals were performed using three different pairs of elevation angles from the 0035 Z volume scans: 0.5° and 1.4°, 1.3° and 4.1°, and 2.0° and 7.5°.

The radar beams in these three experiments intersected roughly 100 m, 280 m and 470 m AGL, respectively, in the vicinity of the tornado. Fortunately, the mean retrieved vortex characteristics (Table 4.7) and retrieved radial wind fields (Figs. 4.12-4.14) at each height were reasonably consistent with the observed Doppler velocity fields.

Table 4.5. Means of retrieved tornado characteristics for selected sets of 5 June 2001 retrievals from DOW radar data. Sample sizes (n) are given below each time.

	Distance from ensemble mean vortex center (m)	**Movement Speed ($m\ s^{-1}$)**	**Heading (0° = east)**	**V_T ($m\ s^{-1}$)**	**V_T^{res} ($m\ s^{-1}$)**	**V_R ($m\ s^{-1}$)**	**R (m)**	**R_{10} (m)**	**α**
0028 Z (n=5)	34	10	-64	26	10	3	66	167	1.0
0031 Z (n=7)	34	11	-67	12	11	0	165	216	0.8
0032 Z (n=16)	15	13	2	35	18	0	76	320	0.9

Table 4.6. Standard deviations of retrieved tornado characteristics for selected sets of 5 June 2001 retrievals from DOW radar data. Sample sizes (n) are given below each time.

	Distance from ensemble mean vortex center (m)	**Movement Speed ($m\ s^{-1}$)**	**Heading (0° = east)**	**V_T ($m\ s^{-1}$)**	**V_T^{res} ($m\ s^{-1}$)**	**V_R ($m\ s^{-1}$)**	**R (m)**	**R_{10} (m)**	**α**
0028 Z (n=5)	18	1	3	26	0	4	14	12	0.1
0031 Z (n=7)	16	4	31	1	2	1	14	54	0.1
0032 Z (n=16)	15	6	22	3	3	1	19	68	0.1

Table 4.7. Means of retrieved tornado characteristics for 5 June 2001 0035 Z retrievals at three different heights. Sample sizes (n) are given below each time.

	Distance from ensemble mean vortex center (m)	**Movement Speed ($m\ s^{-1}$)**	**Heading (0° = east)**	**V_T ($m\ s^{-1}$)**	**V_T^{res} ($m\ s^{-1}$)**	**V_R ($m\ s^{-1}$)**	**R (m)**	**R_{10} (m)**	**α**
100 m AGL (n=3)	41	5	1	16	10	1	134	206	1.1
280 m AGL (n=8)	34	5	-20	21	13	-2	76	155	0.9
470 m AGL (n=4)	64	7	36	16	10	-1	127	199	1.1

Figure 4.8. Clockwise from top left: observed, residual (observed minus retrieved broadscale), retrieved vortex, and retrieved total radial velocity fields at 0028 Z for DOW radars located (a) east and (b) north-northeast of the analysis domain. The axes indicate *x*- and *y*-displacements from the radar.

(a)

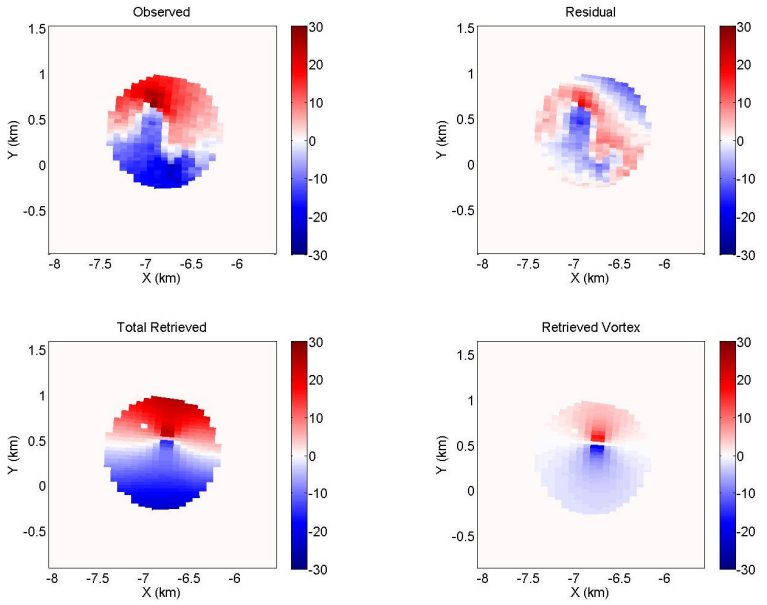

(b)

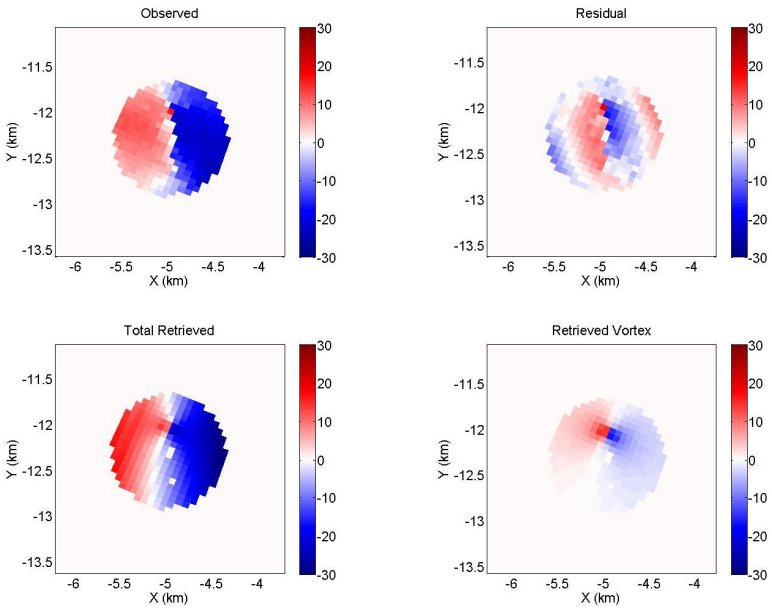

Figure 4.9. Same as Fig. 4.8 except for a different FG vortex center.

(a)

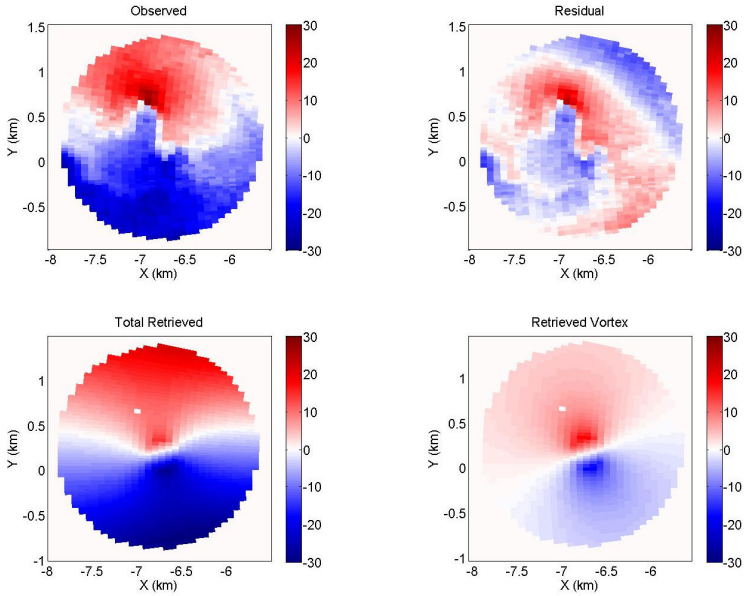

(b)

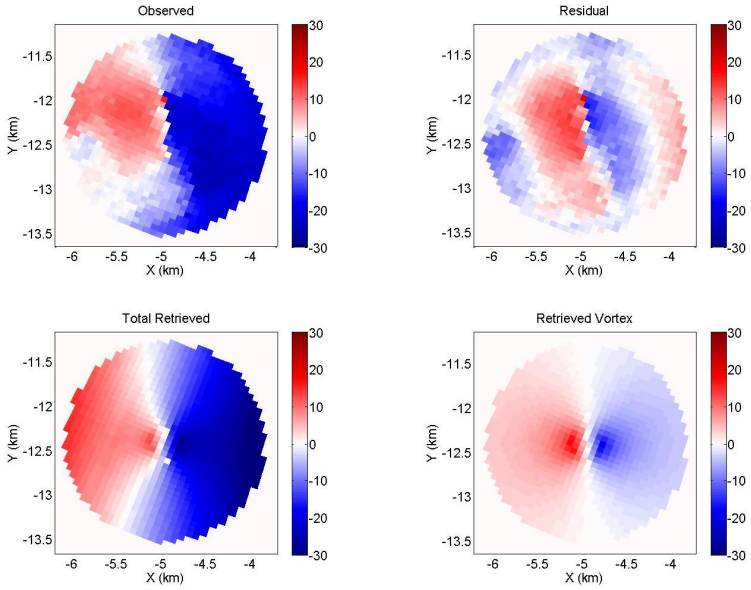

Figure 4.10. Same as Fig. 4.8 except at 0031 Z.

(a)

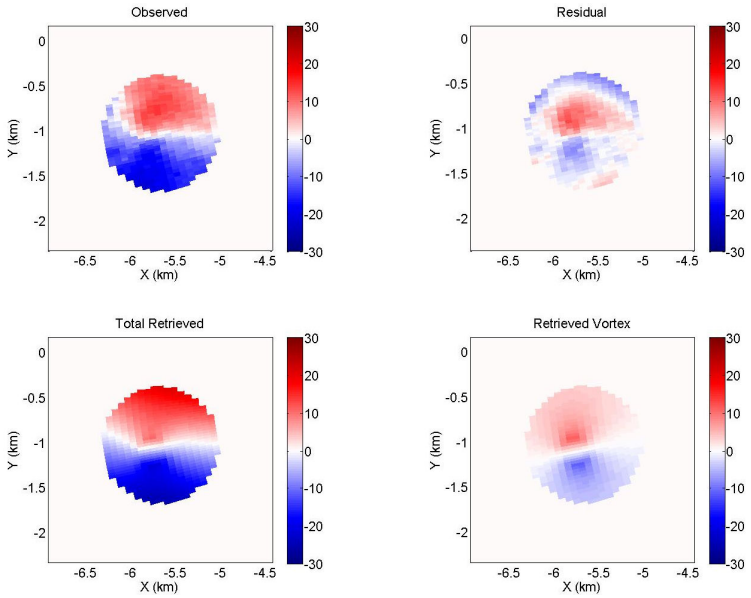

(b)

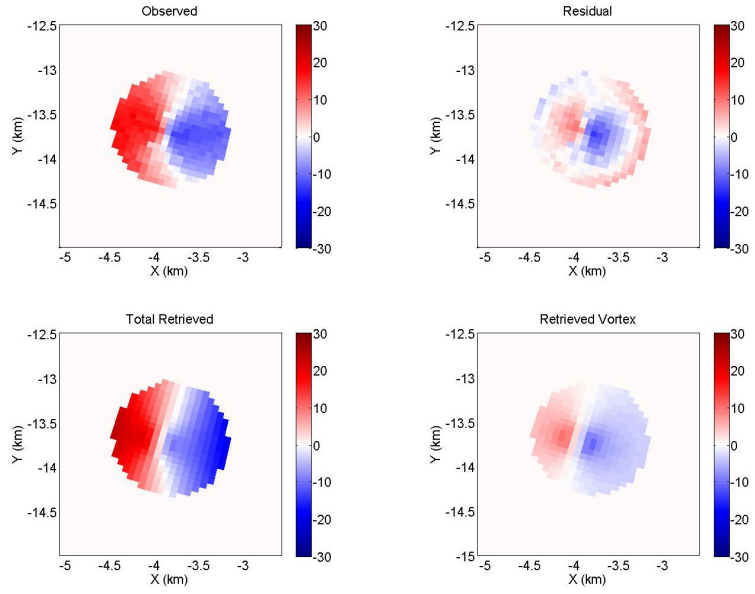

Figure 4.11. Same as Fig. 4.8 except at 0032 Z.

(a)

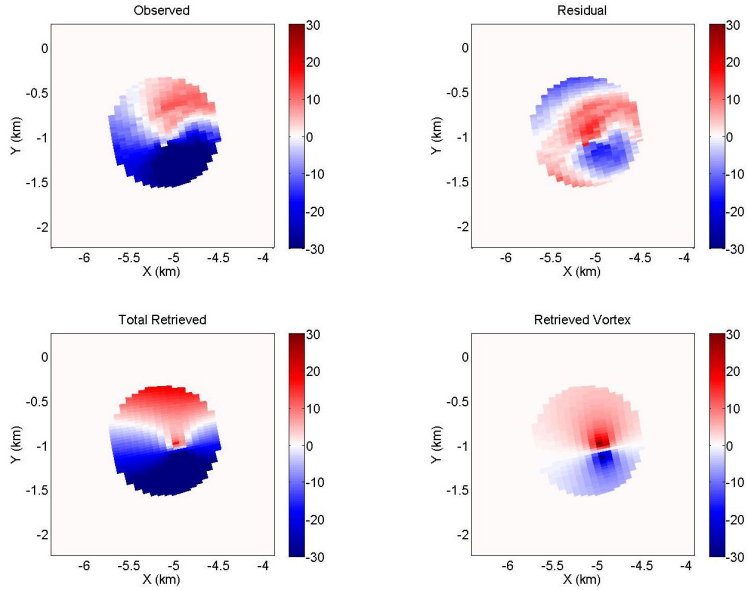

(b)

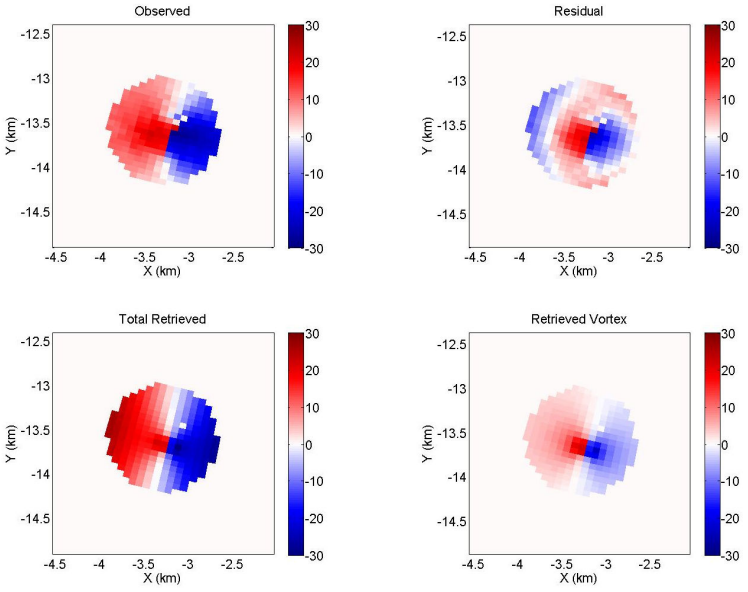

Figure 4.12. Clockwise from top left: observed, residual (observed minus retrieved broadscale), retrieved vortex, and retrieved total radial velocity fields at 0035 Z for DOW radars located (a) east and (b) north-northeast of the analysis domain. The axes indicate *x*- and *y*-displacements from the radar. Elevation angles of (a) 1.4° and (b) 0.5° used.

(a)

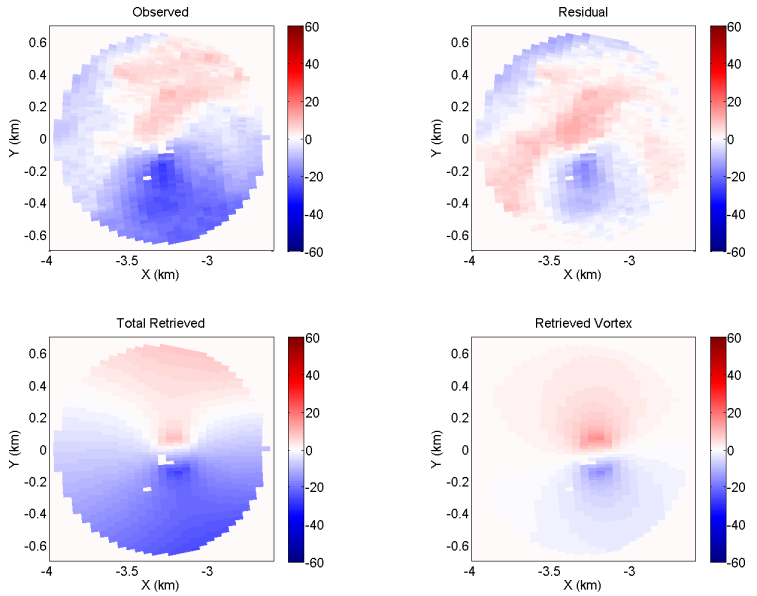

(b)

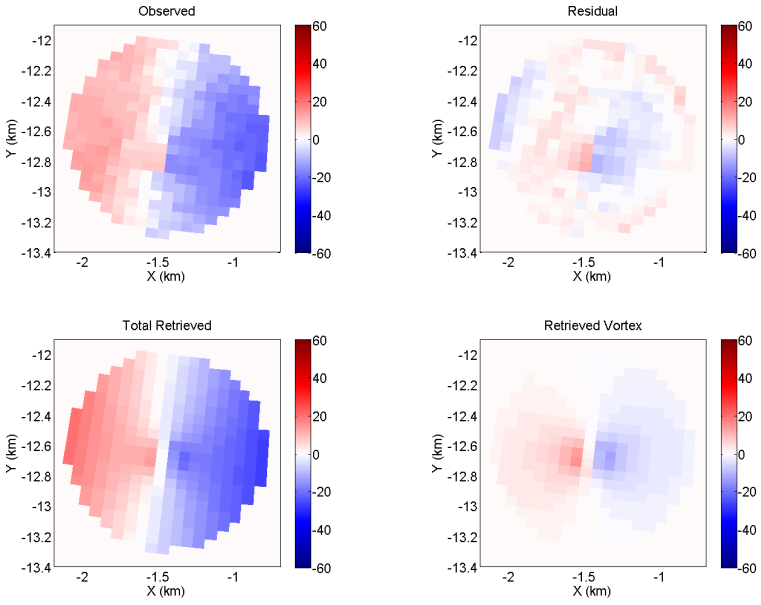

Figure 4.13. Same as Fig. 4.12 except using elevation angles of (a) 4.1° and (b) 1.3°.

(a)

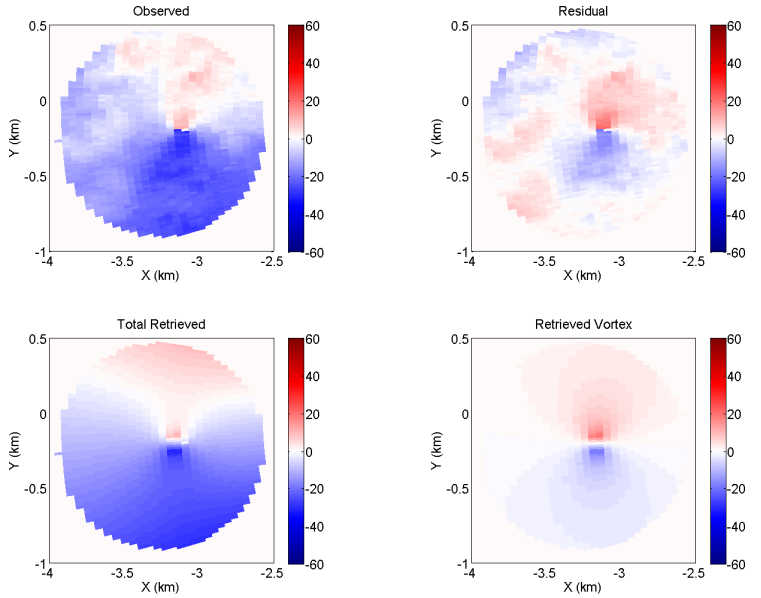

(b)

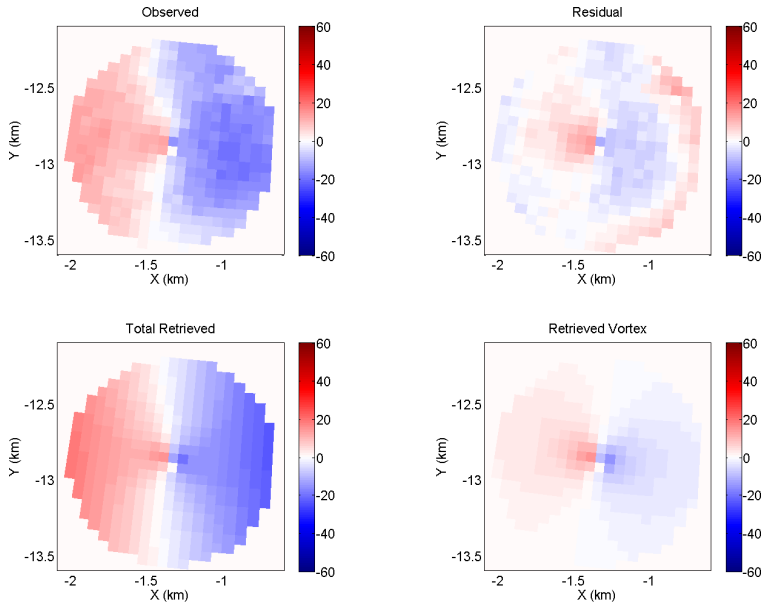

Figure 4.14. Same as Fig. 4.12 except using elevation angles of (a) 7.5° and (b) 2.0°.

(a)

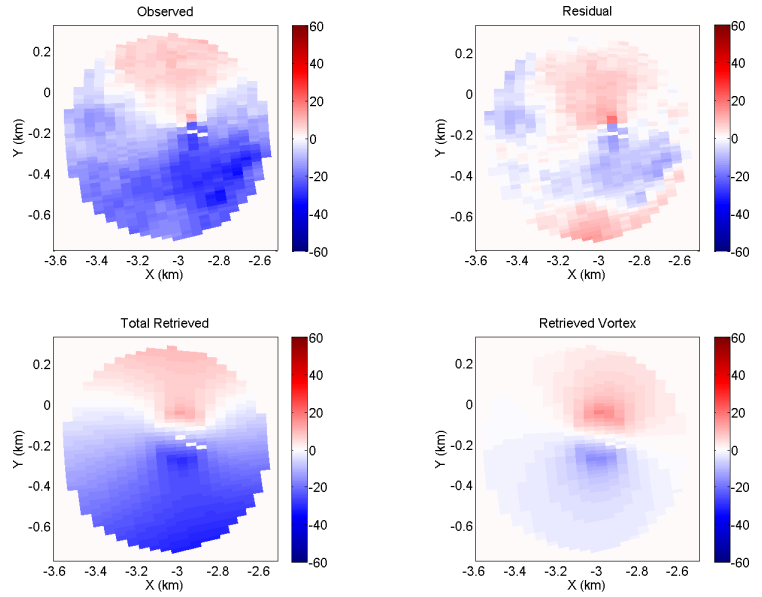

(b)

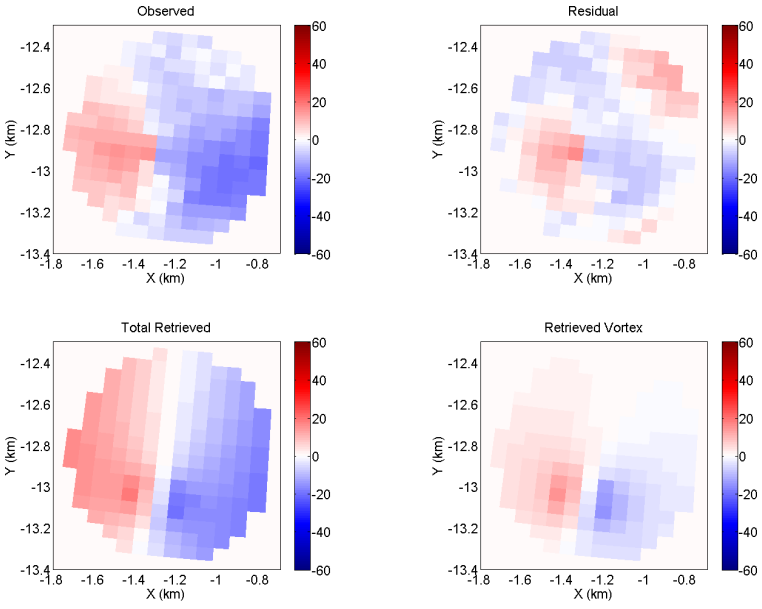

4.4 IP-1 Observations of 10 February 2009 Low-Level Mesocyclone

4.4.1 Description of dataset

A series of supercells developed within the IP-1 CASA testbed on 10 February 2009. The fourth of these storms traveled through the dual-Doppler domain of the KSAO (Chickasha) and KCYR (Cyril) radars (Figure 4.15). Though no tornadoes were reported with this storm, a low-level mesocyclone (LLM) of ~1 km diameter was evident in the radial velocity imagery for several minutes after entering the dual-Doppler lobe. The vortex detection technique was applied to this case to determine whether it could be used for mesocyclone detection. The technique was applied to three pairs of KCYR/KSAO PPI scans collected at 2107 Z, 2110 Z and 2111 Z. Widespread velocity contamination and lack of radar coverage prevented the technique from being applied at 2108 Z and 2109 Z (see Fig. 4.23 for an example of particularly severe velocity contamination from another case). In order to assess the capability of the technique when spurious velocity data are present, no manual velocity editing was performed in the preliminary experiments. In all three sets of retrievals, the 2° KCYR radar scan was used. It would have been desirable to use the 1° KSAO scan in all three cases in order to minimize the vertical spacing between the two radar beams. However, too much spurious velocity data existed within the 1° KSAO scans at 2110 Z and 2111 Z, and so the 2° KSAO scans were used at those times instead. Fortunately, the heights of the two radar beams in the vicinity of the LLM were within several hundred meters of each other at all three times, and the 1° and 2° KSAO radial velocity fields were quite similar to one other. The range and azimuthal sampling intervals and half-power beamwidth for both radars were

(respectively) 96 m, 1° and 1.8°. The tangential sampling intervals near the LLM were ~200 m and ~600 m for KCYR and KSAO, respectively.

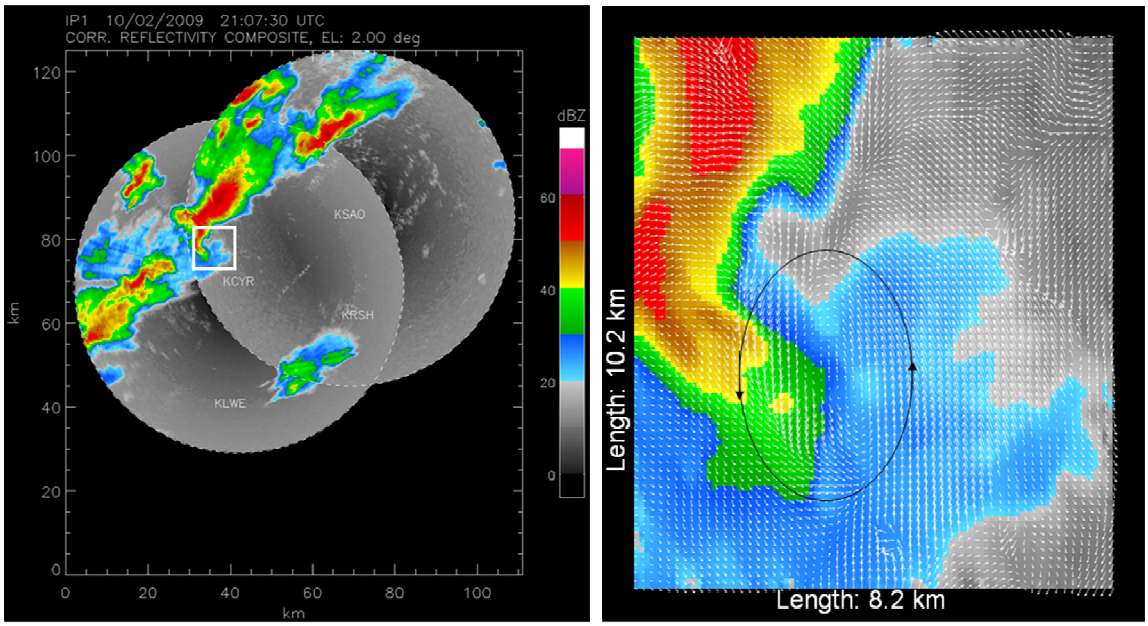

Figure 4.15. (left) Composite reflectivity field within KCYR-KSAO domain at 2107 Z, and (right) zoomed-in view valid at same time over region outlined by white box in top panel with overlaid dual-Doppler analysis (courtesy of V. Chandrasekar).

4.4.2 Retrieval results

Since the LLM appeared to have V_T < 10 m s^{-1} based on visual inspection of the radial velocity fields, the detection threshold V_{det} was set to 5 m s^{-1} in these experiments. For the same reason, the values of n used to determine V_T^{res} (see Section 2.5) were set to 5, 6, 7, 8, 9, 10 and 11 m s^{-1}. A gate-to-gate velocity difference threshold of 10 m s^{-1} was used in the domain-selection criteria. Of the three times at which retrievals were performed, the LLM was only detected at 2107 Z. The ensemble means and standard deviations of selected vortex parameters from the 19 retrievals passing the detection criteria at 2107 Z are shown in Table 4.8. In addition, the 2107 Z retrieval whose vortex

parameter values most closely approximate the ensemble means is plotted alongside the observations (Figure 4.16). The retrieved vortex and total wind fields compare reasonably well to the residual and observed wind fields, respectively. Though the retrieved vortex was typically slightly stronger than the actual vortex on observable scales, the V_T^{res} were, as expected, generally more consistent with the observed radial wind field than were the V_T. The mean R and R_{det} also appear reasonable based on the observations. The relatively small spread in the retrieved vortex locations and vortex size and intensity characteristics would have served to increase confidence in the ensemble mean vortex retrieval in an operational setting. As expected, the vortex translational velocity varies more from retrieval to retrieval than the other vortex characteristics. However, the ensemble mean vortex heading and speed (43° and 18 m s^{-1}) are roughly consistent with estimates calculated from the subjectively-determined vortex locations at 2107 Z and 2108 Z (45° and 12 m s^{-1}).

Table 4.8. Means and standard deviations of retrieved LLM characteristics for 2107 Z 10 February 2009 retrievals from CASA IP-1 data.

	Distance from ensemble mean vortex center (m)	**Movement (m s^{-1})**	**Heading (0° = east)**	**V_T (m s^{-1})**	**V_T^{res} (m s^{-1})**	**V_R (m s^{-1})**	**R (m)**	**R_5 (m)**	**α**
mean	109	18	43	14	8	-7	397	1021	1.1
std dev	61	5	20	2	1	2	69	224	0.2

As mentioned above, the LLM was not detected in any of the 2110 Z or 2111 Z retrievals. Many of the 2110 Z retrievals retrieved a spurious vortex near a short radial

segment of spurious velocity data located ~2 km south of the LLM in the KSAO domain (Figure 4.17). This is because an isolated, spuriously large velocity estimate or a radially-aligned segment of such estimates can create a localized region of high azimuthal shear and thus a minimum in the cost function *J*. Many of the 2111 Z retrievals either placed a spurious vortex near another spurious radial velocity segment located ~ 2 km south of the LLM in the KSAO scan, or retrieved (relatively poorly) what may have been a weak vortex to the north of the LLM (Figure 4.18). Fortunately, no weak or spurious vortices passed the detection criteria at either time. No vortices were retrieved at the location of the LLM at either time, indicating that the failure of the technique to detect the LLM was due not to the detection criteria, but likely (at least in part) to the existence of multiple minima in *J* (many or all of which may have resulted from the spurious velocity data) that prevented the LLM from being retrieved.

In order to determine whether the presence of spurious velocity data prevented the LLM from being detected in the 2110 Z and 2111 Z retrievals, these experiments were repeated using the same first guess vortex centers but with spurious velocity values spatially filtered. More specifically, each of the visually-identified spurious velocity values was set equal to the mean of the velocities of the two azimuthally-adjacent radar gates prior to the retrievals. Filtering the bad velocity data allowed the LLM to be detected in six retrievals at 2110 Z. As was the case with the 2107 Z experiments, the mean retrieved parameters for the LLM at 2110 Z were consistent with the observations (Table 4.9) and the retrieved radial wind field whose vortex parameter values most closely match the ensemble mean compares well with the observed radial wind field (Figure 4.19). Encouragingly, the mean retrieved vortex translational speed and direction

(21 ms^{-1} and 51°) again compare well with subjective estimates (18 ms^{-1} and 53°). However, in one case the technique appears to make a false detection (Figure 4.20). Though the existence of a real vortex at the retrieved vortex location cannot be ruled out based solely on inspection of the KCYR observed and retrieved radial velocity fields, the retrieved KSAO velocity fields match poorly with the observed and residual fields, suggesting that a linear shear feature has been misidentified as an intense vortex.

Table 4.9. Means and standard deviations of retrieved LLM characteristics for 2110 Z 10 February 2009 retrievals from CASA IP-1 data (spurious velocities filtered).

	Distance from ensemble mean vortex center (m)	**Movement ($m\ s^{-1}$)**	**Heading (0° = east)**	**V_T ($m\ s^{-1}$)**	**V_T^{res} ($m\ s^{-1}$)**	**V_R ($m\ s^{-1}$)**	**R (m)**	**R_5 (m)**	**α**
mean	106	21	51	14	5	13	215	587	1.0
std dev	62	4	24	3	1	2	42	166	0.1

Unlike in the 2110 Z experiments, the LLM was not detected at 2111 Z even after filtering spurious velocity data. Two new sets of retrievals were subsequently performed, one using the original velocity data and the other the filtered data, with the first guess vortex center grid centered on the visually-estimated LLM center. A total of 25 (rather than 9) first guesses separated by 250 m (rather than 500 m) in the x- and y-directions were used in order to increase the probability of detecting the LLM. Despite these favorable conditions, the only retrieval to obtain the LLM in each experiment was that with the near-perfect first guess vortex center (the retrieved vortex passed the detection criteria in both cases). This result indicates that the LLM at 2111 Z is indeed associated

with a local minimum in *J*, but that this minimum is highly localized in the cost function space. In other words, the LLM is not dominant enough in the wind field to be reliably retrieved. Inspection of the observed KCYR radial wind field at 2111 Z reveals a large region of suspect velocities east of the LLM (Figure 4.21). Not surprisingly, many of the retrievals in all four sets of 2111 Z experiments produced a vortex along the (presumably spurious) intense linear shear zone in this area. It therefore seems likely that the heavy velocity data contamination at 2111 Z inhibited detection of the LLM.

Figure 4.16. Clockwise from top left: observed, residual (observed minus retrieved broadscale), retrieved vortex, and retrieved total radial velocity fields for the retrieval closest to the ensemble mean at 2107 Z for (a) KCYR and (b) KSAO. The axes indicate x- and y-displacements from the radar.

(a)

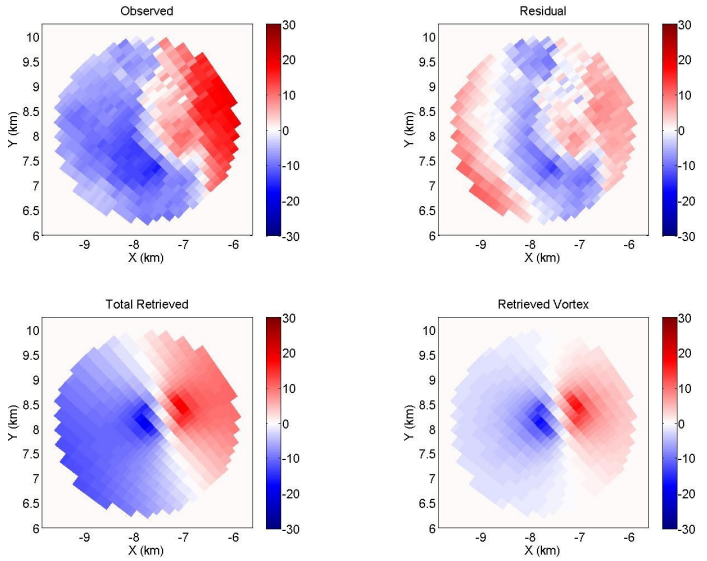

(b)

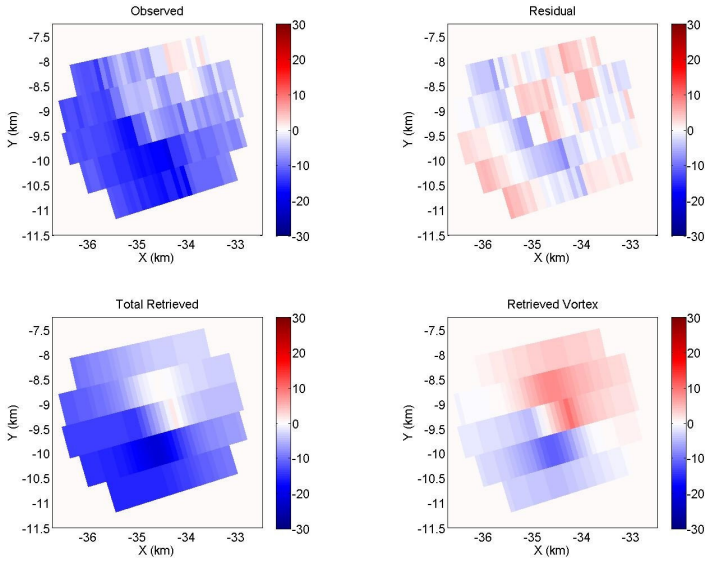

Figure 4.17. Same as Fig. 4.16 except for a spurious retrieval at 2110 Z.

(a)

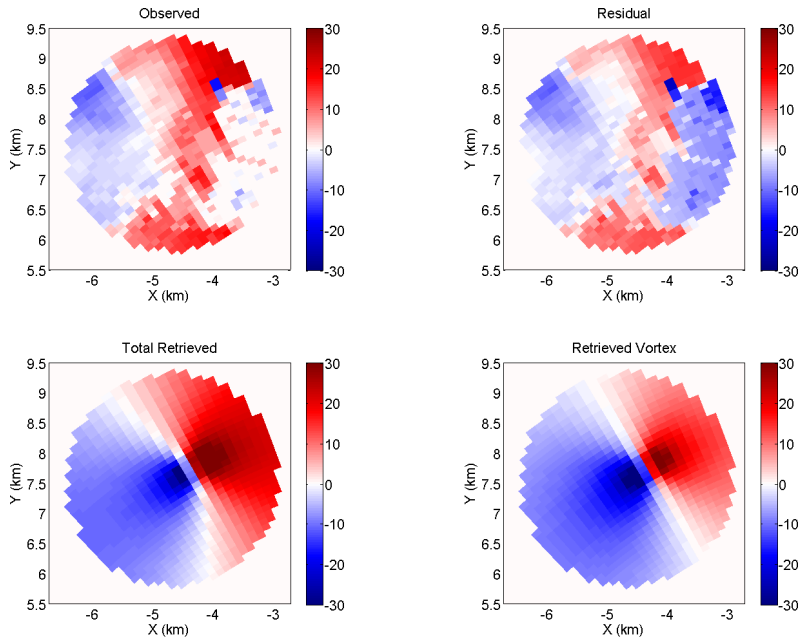

(b)

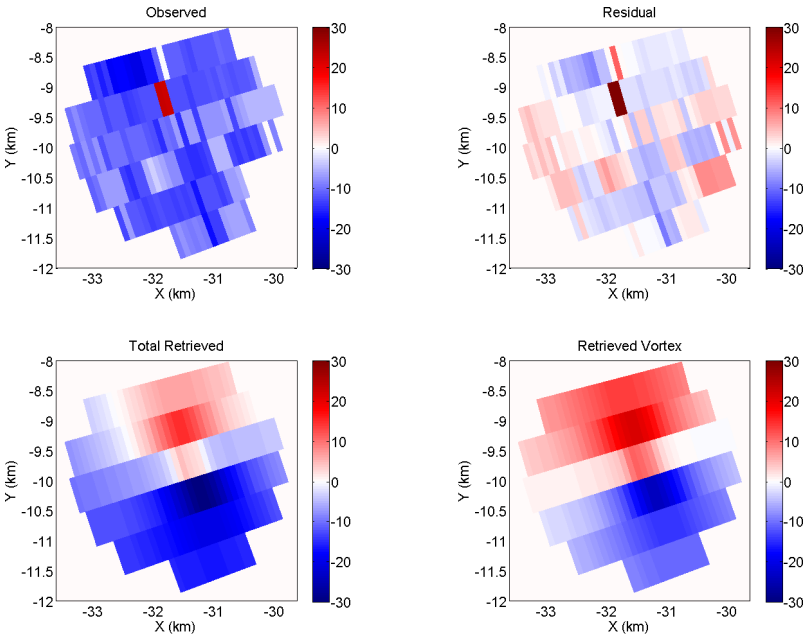

Figure 4.18. Same as Fig. 4.16 except for a retrieval of a weak vortex at 2111 Z.

(a)

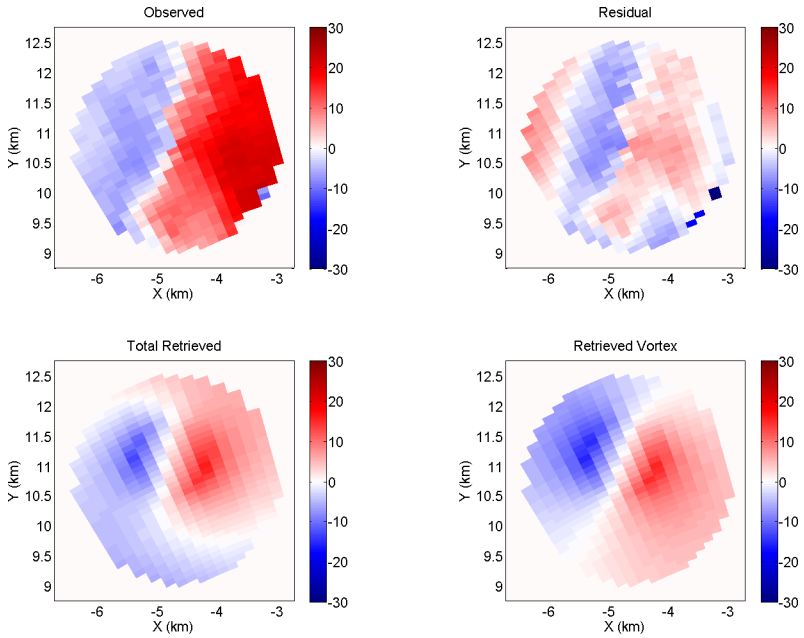

(b)

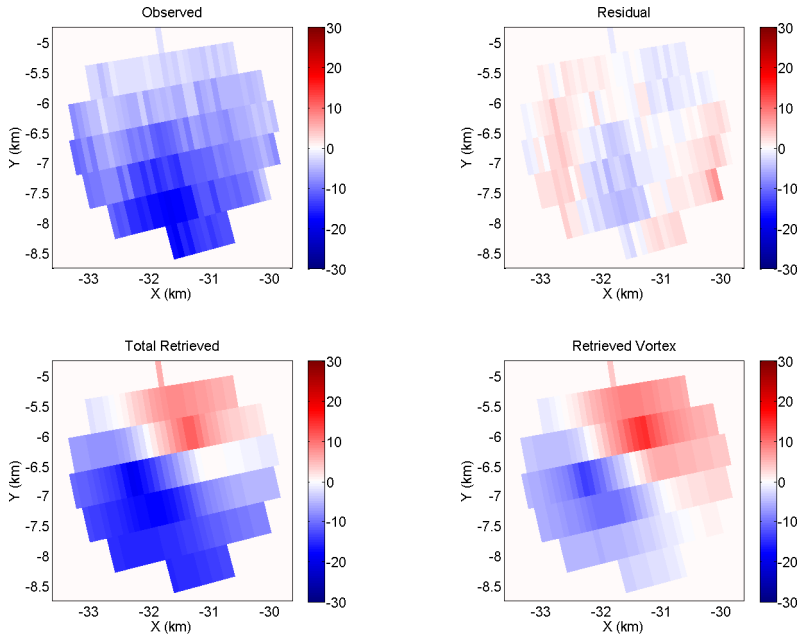

Figure 4.19. Same as Fig. 4.17 but after filtering spurious velocities.

(a)

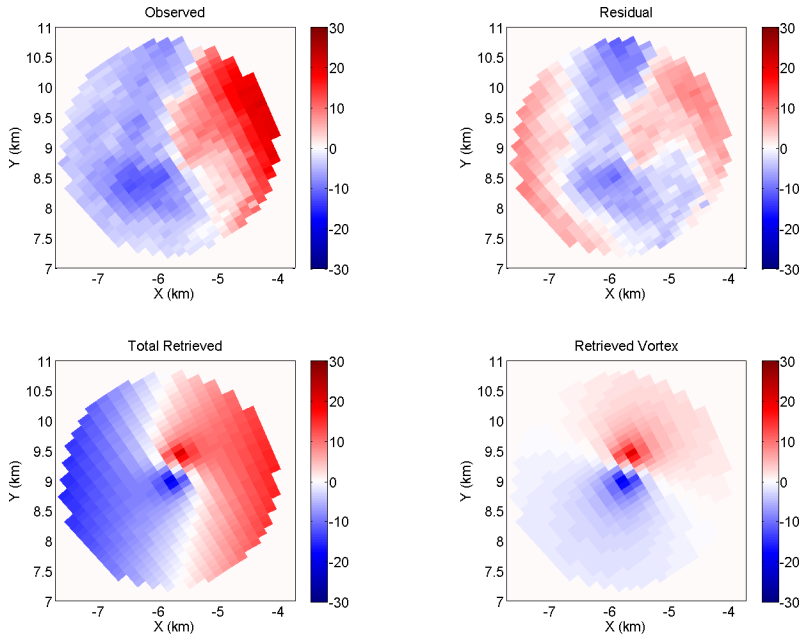

(b)

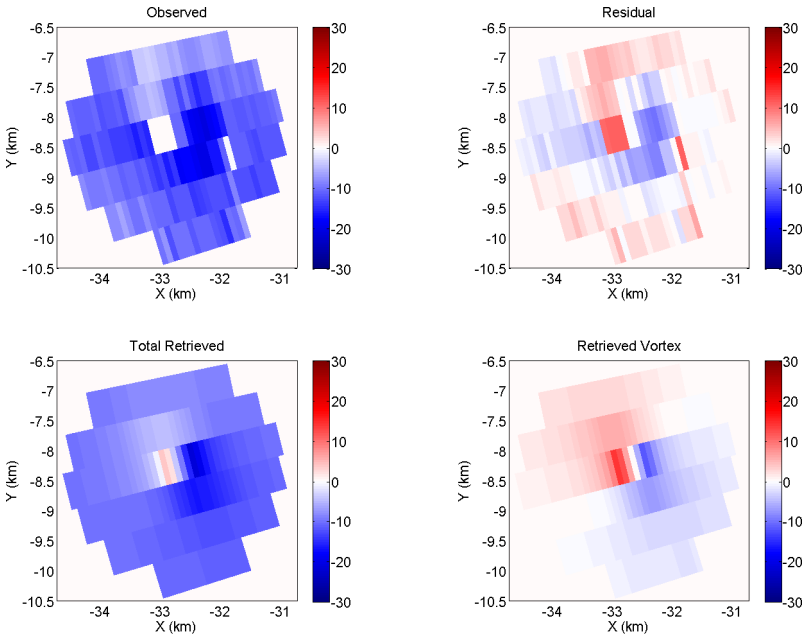

Figure 4.20. Same as Fig. 4.19 but for a false vortex detection.

(a)

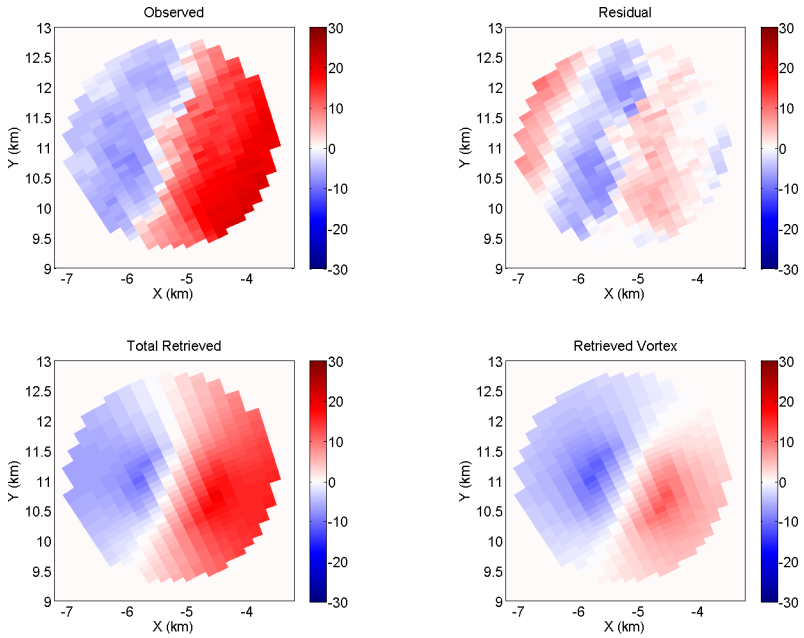

(b)

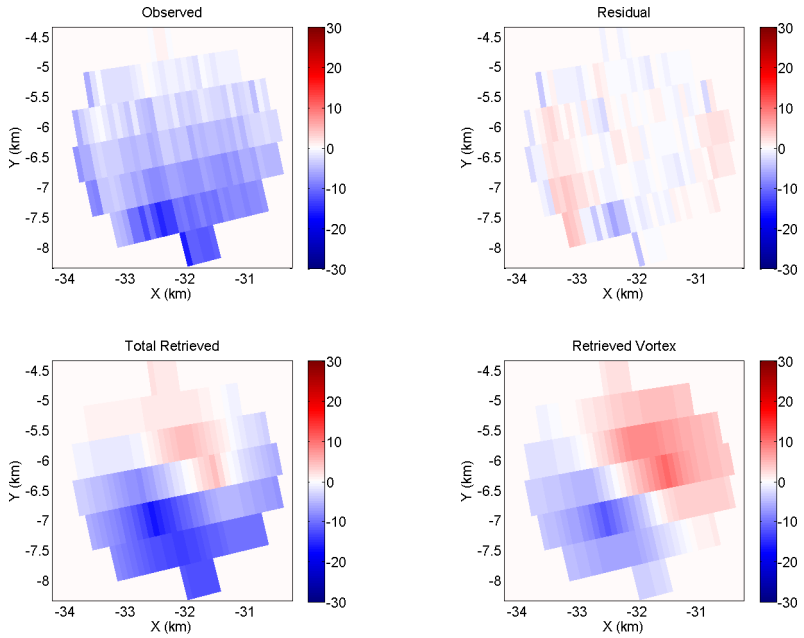

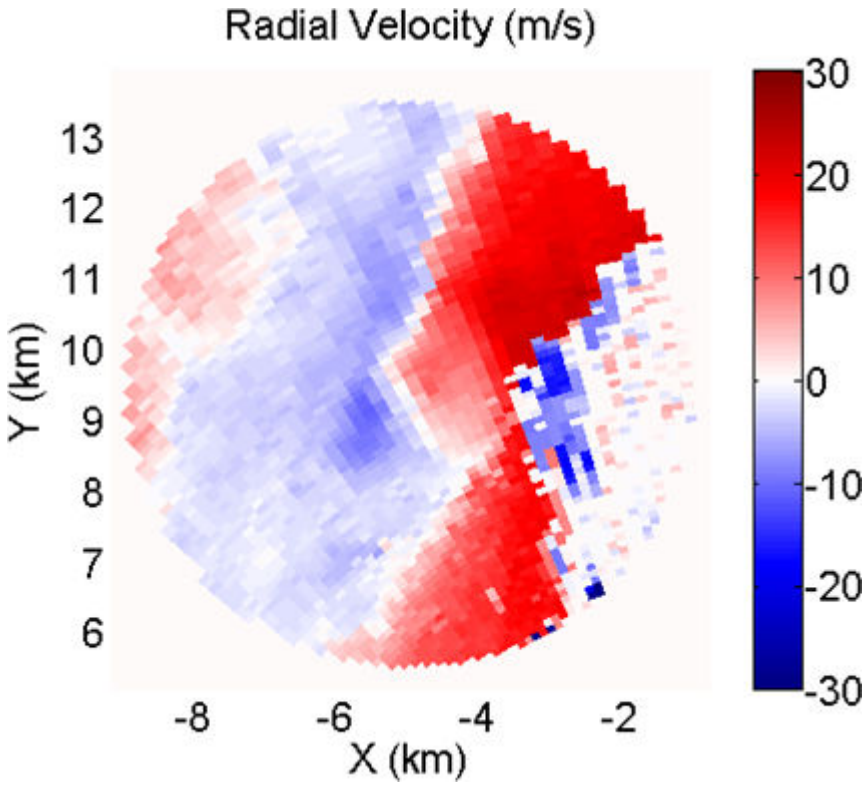

Figure 4.21. Observed KCYR radial velocity field at 2111 Z.

4.4.3 Discussion

Since low-level mesocyclogenesis frequently precedes tornadogenesis (Trapp et al. 2005), real-time detection of low-level mesocyclones may be valuable to the tornado warning process. The experiments above suggest the technique can be made sensitive enough to reliably detect and characterize LLMs, even in cases where they are quite weak compared to the parent mid-level mesocyclone. Furthermore, the technique appears capable of skillfully estimating the size and strength of such vortices. Since LLMs can be weaker than most tornadoes (as exemplified in this case), reliable detection of LLMs may require that the detection threshold V_{det} be set lower than the optimal threshold for tornado-only detection. Unfortunately, adopting less stringent detection criteria may

increase the potential for regions of linear shear or weak rotation to be misidentified as operationally-significant vortices. This appears to have been the case in one of the 2110 Z filtered-data retrievals (Figure 4.20). Thorough examination of the tradeoff between the increase in false detections and the increase in the number of intense vortices correctly identified by the technique is required for the determination of the optimal V_{det} for a given radar network and class(es) of vortices.

As discussed above, bad velocity data likely contributed to the LLM being undetected in the original 2210 Z and 2211 Z experiments. It may therefore be desirable to use multiple pairs of elevation angles within each horizontal analysis domain in order to minimize the probability of bad velocity estimates preventing real vortices from being detected. However, as was the case here, spurious velocity data may be present near the vortex within all of the PPIs (from one or both radars) that are vertically-proximate to the vortex, making detection of the real vortex unlikely. Thus, the technique will often be ineffective in cases where velocity data contamination is widespread near the vortex. Additionally, the existence of spurious velocity data anywhere in the multi-radar domain can increase the number of retrievals that are performed outside of the real vortex regions, thus needlessly increasing computational time. In these experiments, the majority of the regions within which retrievals were performed (a total of 11, 17 and 10 regions were identified by the domain-selection criteria at 2107 Z, 2210 Z and 2211 Z, respectively) contained spurious velocity data and no intense vortices. Velocity data quality control will therefore be critical to the success of the technique in radar networks that are prone to velocity contamination. Fortunately, despite the large number of contaminated velocity values present in every radar scan used in the above experiments,

none of the numerous spurious vortex retrievals passed the detection criteria. The impact of spurious velocity data on the technique's false detection rate thus does not seem to be unduly large.

4.5 IP-1 Observations of 14 May 2009 Anadarko, OK Tornado

4.5.1 Description of dataset

A supercellular EF-2 tornado traveled southward along the east side of Anadarko, OK from 0226 Z to 0244 Z on 14 May 2009, producing a damage path up to 250 yd wide (NCDC 2010d). The tornado occurred within the dual-Doppler KCYR-KSAO domain and was indicated in the radar data by a distinct radial velocity couplet collocated with a hook echo signature (Figure 4.22). Unfortunately, widespread contamination of radar velocity data in and near the tornado (Figure 4.23) required that the data be quality-controlled prior to applying the technique. The velocity contamination was mostly caused by inaccurate ground clutter filtering near the zero-isodop (personal communication, Francesc Junyent). Velocity aliasing also occurred as radial winds exceeded the ~30 ms^{-1} Nyquist velocity. The velocity fields were subsequently manually de-aliased and then objectively filtered by V. Chandrasekar and Nitin Bharadwaj for seven volume scans valid at 1-min intervals from 0228 Z to 0234 Z. Unfortunately, many of the velocity data were unrecoverable, resulting in gaps in the filtered velocity fields near the tornado in the low-level radar scans. This prevented the tornado from being detected in retrievals valid at 0228 Z, 0229 Z, 0230 Z and 0231 Z using the 1°, 2° or 3° scans.

Fortunately, fewer velocity estimates were missing in the last three edited volume scans, thereby allowing the technique to detect the tornado at these times. However, some caution must be taken in interpreting the results. Due to the density of spurious data in/near the tornado and the fact that spatial filters can produce large errors where large gradients are present, it is uncertain to what extent the edited velocity fields represent the true tornadic wind field. Nevertheless, the filtered velocity fields appear reasonably representative of a strong tornado, regardless of how accurately they represent this particular tornado. This is therefore a valuable (albeit non-ideal) test case for the technique, especially since no other dual-Doppler CASA observations of tornadoes have been collected to date.

The 0232 Z, 0233 Z and 0234 Z retrievals were performed using 2° radar scans, yielding an analysis domain height of ~1 km at the tornado, which was located 25-30 km from both radars during this period. Both radars sampled every 96 m in range and 0.5° in azimuth. The radars observed the tornado within 15 s of each other in all three cases. V_{det} was set to 10 m s^{-1} in these experiments, and the domain-selection criteria used gate-to-gate velocity difference and shear thresholds of 15 m s^{-1} and .05 s^{-1}, respectively.

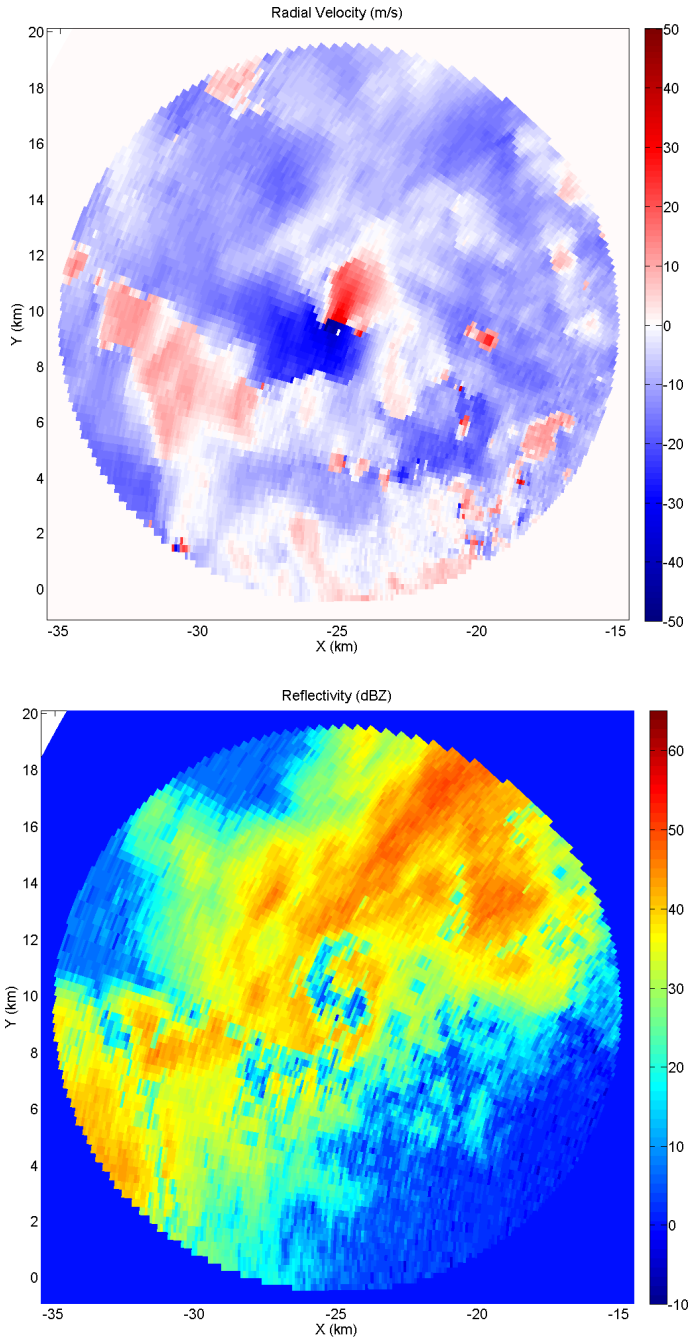

Figure 4.22. KSAO edited radial velocity (top) and reflectivity (bottom) at 0232 Z.

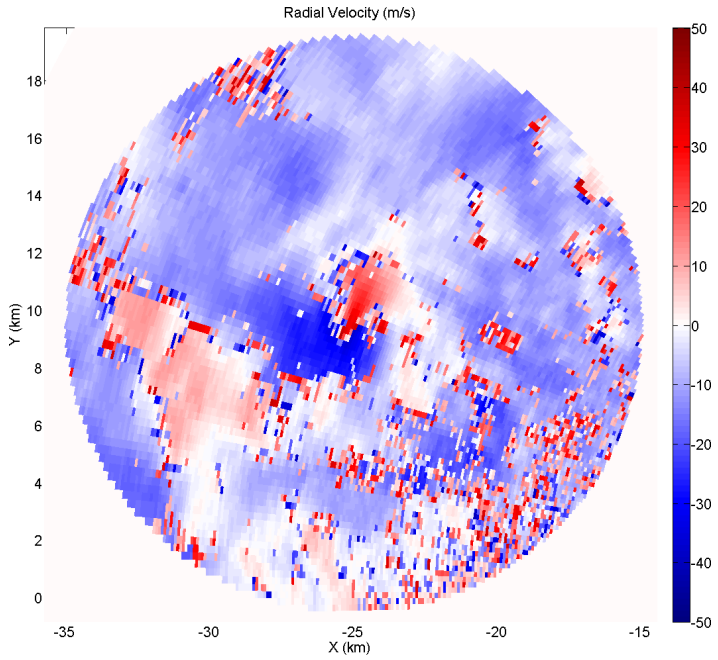

Figure 4.23 KSAO unedited radial velocity at 0232 Z.

4.5.2 Retrieval results

The tornado was detected by 8, 15 and 3 retrievals at 0232 Z, 0233 Z and 0234 Z, respectively. The means and standard deviations of the tornado retrievals are given in Tables 4.10 and 4.11, respectively. As in the previous sections, a representative retrieval is compared to the (edited) observed radial velocity field at each of the retrieval times (Figures 4.24 - 4.26). Verification of the retrieved vortex characteristics is somewhat hindered by the difficulty in visually distinguishing between the tornado and the mesocyclonic flow in the velocity observations. However, the technique does detect a smaller-scale vortex embedded within the surrounding flow at each time, and the retrieved vortex locations and translation velocities are roughly consistent with the velocity observations. In addition, the retrieved R_{30} at each time is broadly consistent

with the surveyed 250 yd damage path. The V_T^{res} is significantly lower than the maximum winds that actually occurred in the tornado. This is not surprising; the azimuthal sampling interval and beamwidth for both radars were ~ 250 m and ~ 1 km (respectively) at the range of the tornado, while the tornado core diameter was presumably < 250 m (that is, narrower than the reported damage path). Nevertheless, the retrieved V_T^{res} and R_{30} are both indicative of a tornado in each case, despite the tornado not being visually obvious in the observed radial wind fields.

In addition to the tornado, several weaker vortices were retrieved in other regions of the dual-Doppler domain. In agreement with the observations, these vortices were significantly less intense than the retrieved tornado (V_T^{res} = 10 m s^{-1} in all cases), and thus would not have unduly diverted forecasters' attention away from the primary region of concern. The total number of retrieval regions identified by the domain-selection criteria were 15, 13 and 3 at 0232 Z, 0233 Z and 0234 Z, respectively.

Table 4.10. Mean retrieved tornado characteristics for three sets of 14 May 2009 retrievals from CASA IP-1 data.

	Distance from ensemble mean vortex center (m)	**Movement Speed (m s^{-1})**	**Heading (0° = east)**	**V_T (m s^{-1})**	**V_T^{res} (m s^{-1})**	**V_R (m s^{-1})**	**R (m)**	**R_{10} (m)**	**R_{30} (m)**	**α**
0232 Z (n=8)	85	15	20	36	28	-17	123	419	172	1.0
0233 Z (n=15)	31	11	3	38	28	0	130	616	171	0.9
0234 Z (n=3)	26	11	-52	33	27	-2	138	555	153	0.9

Table 4.11. Standard deviations of retrieved tornado characteristics for three sets of 14 May 2009 retrievals from CASA IP-1 data.

	Distance from ensemble mean vortex center (m)	**Movement Speed ($m\ s^{-1}$)**	**Heading (0° = east)**	**V_T ($m\ s^{-1}$)**	**V_T^{res} ($m\ s^{-1}$)**	**V_R ($m\ s^{-1}$)**	**R (m)**	**R_{10} (m)**	**R_{30} (m)**	**α**
0232 Z (n=8)	35	2	10	15	5	6	33	140	35	0.2
0233 Z (n=15)	17	1	10	1	3	1	8	59	13	0.0
0234 Z (n=3)	16	2	15	3	3	1	19	22	11	0.0

4.5.3 Discussion

The technique's success in detecting and characterizing the 14 May 2009 tornado is particularly encouraging for two reasons. First, the data were collected by CASA radars, and so there is no question of how representative the dataset is of those that could be collected by CASA-like networks. Second, the tornadic wind field was not unusually large or intense, and the radar sampling geometry was less than ideal, with the tornado occurring 25-30 km from each radar. This test case therefore constitutes the most direct evidence to date that the technique can provide useful guidance during tornado forecasting/warning operations, even when the tornado core is not well-resolved (this will usually be the case even in CASA-like radar networks).

However, this last statement is only valid to the extent that regions of widespread spurious velocity observations can be minimized in CASA-like radar networks. As shown in Fig. 4.23, velocity contamination in the current IP-1 network can be particularly severe near the zero-isodop in regions where ground clutter is filtered. In addition, due to

the relatively large IP-1 radar beamwidth (1.8°) and side lobes, ground clutter may be widespread in all of the low-level radar data. This problem therefore poses a major obstacle to all velocity-based vortex detection algorithms. One way to mitigate the problem is to implement a spatial filter such as that applied to this dataset in real-time. However, doing so introduces a new problem – the modified wind field may not be very representative of the vortex, particularly on smaller scales. Still, this solution is preferable to inputting noisy wind fields to detection techniques, as doing so will often produce an intolerably low POD (new technique) or high FAR (operational techniques). Of course, the best solution is to improve the ground clutter filtering algorithm and, if possible, the radar sampling characteristics so as to minimize the amount of weather signal that is removed. Unfortunately, the latter will often not be feasible because of other tradeoffs; for example, using a larger radar dish in order to achieve a narrower beamwidth would defeat the low-cost radar paradigm.

Figure 4.24. Clockwise from top left: observed, residual (observed minus retrieved broadscale), retrieved vortex, and retrieved total radial velocity fields for the retrieval closest to the ensemble mean at 0232 Z for (a) KCYR and (b) KSAO. The axes indicate x- and y-displacements from the radar.

(a)

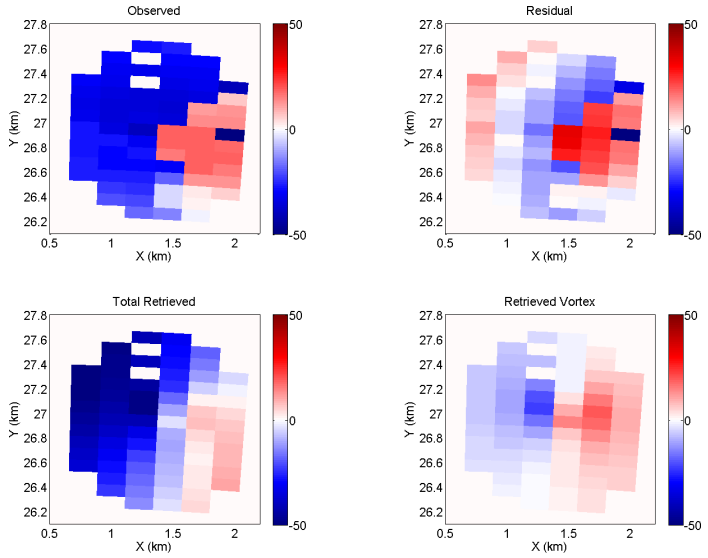

(b)

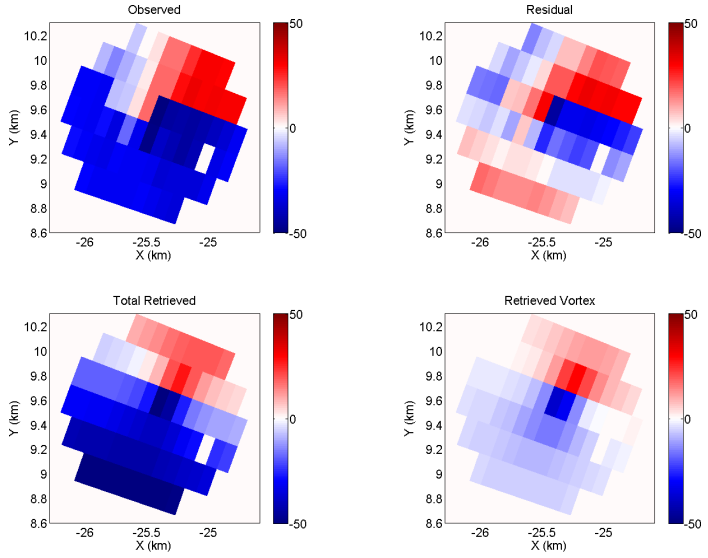

Figure 4.25. Same as Fig. 4.24 except at 0233 Z.

(a)

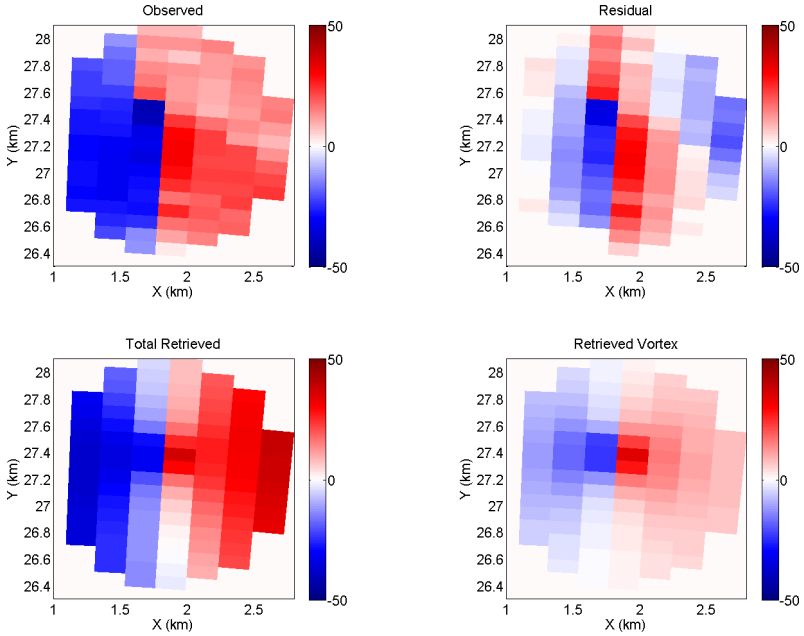

(b)

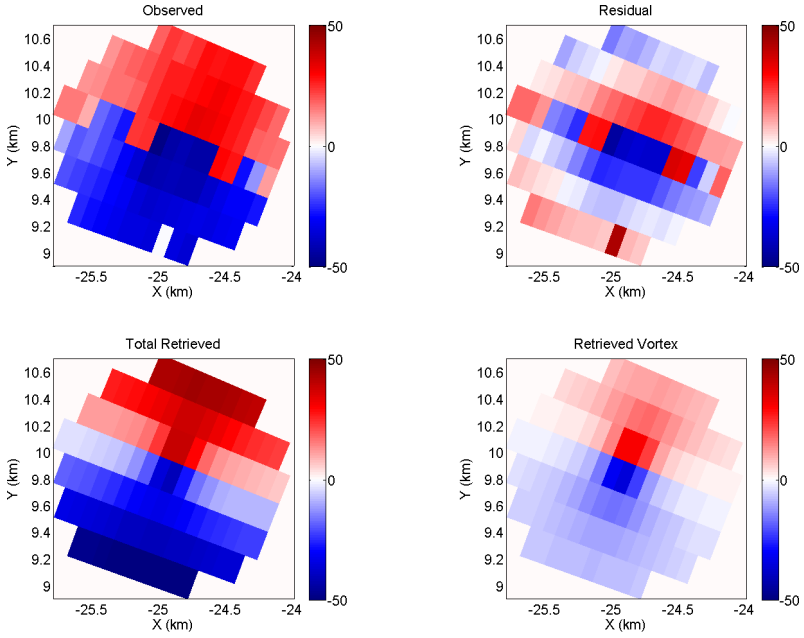

Figure 4.26. Same as Fig. 4.24 except at 0234 Z.

(a)

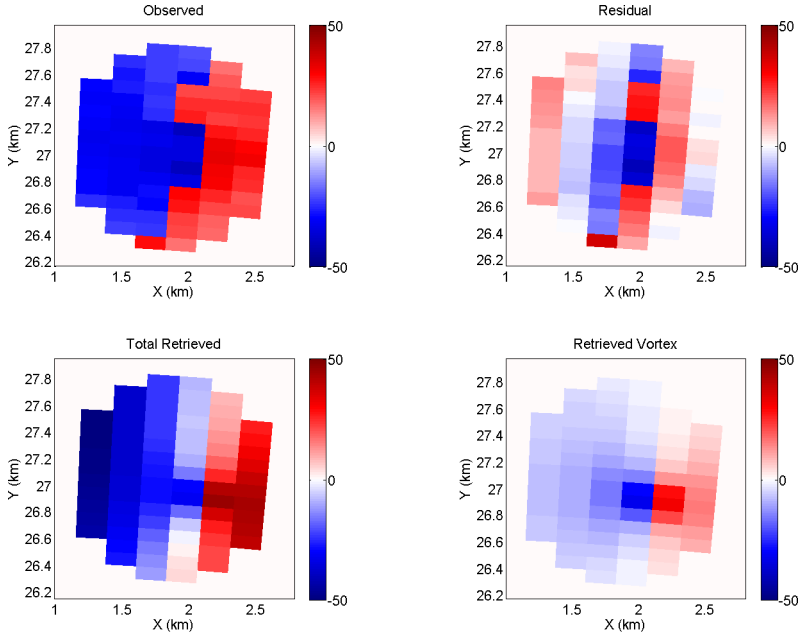

(b)

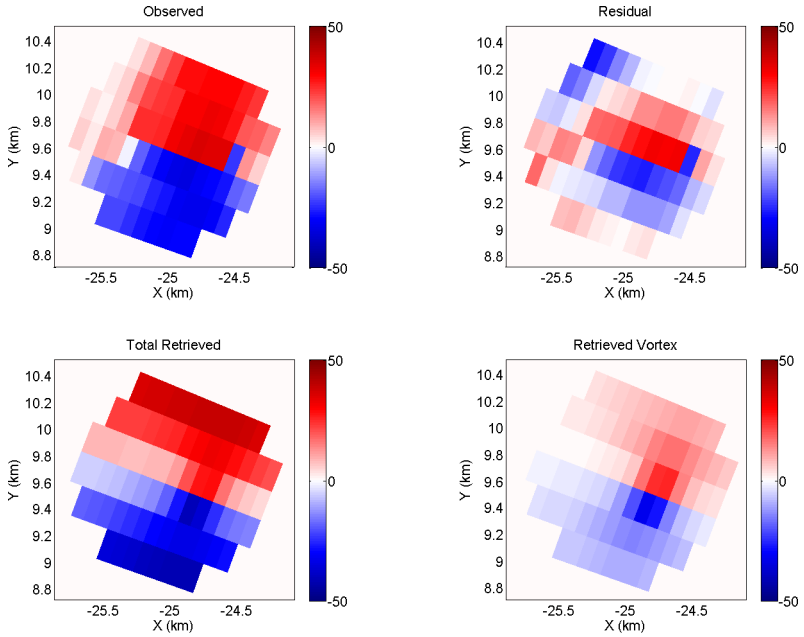

4.6 Retrieving Larger-Scale Vortices

Upon demonstrating the technique's ability to detect and characterize vortices ≤ 1 km in diameter, a logical next step was to apply the technique to larger-scale vortices. Since supercells produce much of the significant severe weather in the U.S., timely detection of mesocyclones is critical to severe weather operations. Though mesocyclones already tend to be quickly detected during severe weather operations (either by objective algorithms or through visual inspection of radial velocity data), the vortex size and strength estimates provided by the new technique may provide valuable additional guidance to forecasters. In addition, the diameter of the largest tornadoes can exceed 1 km. Since tornadoes this large often have high destructive potential, real-time estimates of their size, strength and movement are of critical importance to forecasters.

4.6.1 Mesocyclone retrieval methodology

Since the technique was originally designed primarily to retrieve vortices ≤ 1 km in radius, the algorithm was modified to include a user-selectable "mesocyclone mode" tailored to the retrieval of vortices ~1-3 km in radius. Ideally, this version of the technique would run concurrently with the original version during severe weather operations. The two retrieval modes differ in the vortex parameter first guesses, the sizes of the analysis domains, and the detection criteria. The first guess R is set to 1 km (rather than 200 m) in the mesocyclone retrieval configuration, and the x- and y-spacing between vortex center first guesses is 1500 m (rather than 500 m). The initial analysis domain radius is set to 5 km (rather than 2 km), and the analysis domain in steps #3 and #4 of the retrieval procedure (Section 2.4) is sized such that the vortex radius of $V_T/3$ or 10 m s^{-1}

winds (whichever is larger) adjoins the edge of the domain at the end of the retrieval period. As in the original version of the technique, the modified analysis domain radius is not allowed to exceed that of the initial analysis domain. The V_{det} criterion is set to 20 m s^{-1} (rather than 10 m s^{-1}) since the stronger winds associated with the vortex core are more likely to be observed in larger vortices. In addition, the normalized rms error in each radar's retrieved radial wind within R_{det} of the vortex center (Section 2.5) must be less than 0.75 (rather than 1.0 as in the original technique) for a detection to be made. This ad hoc modification was motivated by poor vortex retrievals in preliminary experiments.

It should be noted that even a 5-km radius analysis domain is not wide enough to encompass larger mesocyclones, the diameters of which can approach 10 km. A third retrieval configuration using an initial analysis domain radius of ~10 km would be required to ensure the detection and characterization of such vortices. Given that smaller-scale vortices are the focus of this study, however, such a configuration was not tested.

4.6.2 Dual-Doppler Retrievals

The 14 May 2009 and 29 May 2004 experiments (Sections 4.5 and 4.2) were repeated using the new mesocyclone retrieval configuration described above. As in the original experiments, the collocation of different-sized vortices posed a significant challenge to the technique. In the new experiments, however, the target vortices themselves contained smaller-scale vortices. Since vortices that are significantly smaller than the analysis domain are not captured by the broadscale model parameters and thus are not subtracted from the observed radial wind field before the vortex retrieval, one

concern was that the retrieved vortices in these experiments would be more representative of the sum of the two vortex wind fields than of the larger vortex alone.

The 14 May 2009 mesocyclone was detected at all three times, and no false detections were made. Visual comparisons of the residual and retrieved vortex wind fields (Figures 4.27-4.29) indicate the tornado had little impact on the retrievals. The mesocyclone is evidently sufficiently dominant in the wind field that minima in J primarily associated with the tornado are unlikely to be reached from a given first guess vortex center. The mean retrieved R, R_{20} and V_T^{res} (Table 4.12) all appear consistent with the observed wind fields.

The results of the 29 May 2004 mesocyclone-mode experiments were similarly encouraging. The tornado was detected at all five times with no false detections made. The mean V_T^{res} and R_{20} (Table 4.13) appear quite consistent with the observations, successfully capturing the expansion of the stronger vortex winds with time (Figures 4.30-4.32). By 0052 Z, the tornado has become large enough for F-2 winds to be detected by the technique, consistent with the surveyed F-2 damage.

Table 4.12. Mean retrieved mesocyclone characteristics for three sets of 14 May 2009 mesocyclone-mode retrievals from CASA IP-1 data.

	Distance from ensemble mean vortex center (m)	**V_T (m s^{-1})**	**V_T^{res} (m s^{-1})**	**V_R (m s^{-1})**	**R (m)**	**R_{20} (m)**	**α**
0232 Z (n=4)	117	36	31	-4	953	1360	1.7
0233 Z (n=6)	99	40	26	7	813	1098	2.2
0234 Z (n=7)	93	38	28	3	947	1428	1.6

Table 4.13. Mean retrieved tornado characteristics for five sets of 29 May 2004 mesocyclone-mode retrievals from SMART-Radar data.

	Distance from ensemble mean vortex center (m)	**V_T (m s^{-1})**	**V_T^{res} (m s^{-1})**	**V_R (m s^{-1})**	**R (m)**	**R_{20} (m)**	**R_{30} (m)**	**R_{40} (m)**	**R_{50} (m)**	**α**
0022 Z (n=3)	154	35	25	-13	1281	1929				1.6
0027 Z (n=9)	137	38	25	-3	1039	1624				1.6
0033 Z (n=13)	168	45	35	-18	920	1637	1242			1.5
0038 Z (n=14)	190	51	29	-7	1161	2067	1691			1.7
0052 Z (n=10)	109	70	50	-2	894	2360	1721	1376	1156	1.3

Figure 4.27. Same as Fig. 4.24 except for mesocyclone-mode retrievals.

(a)

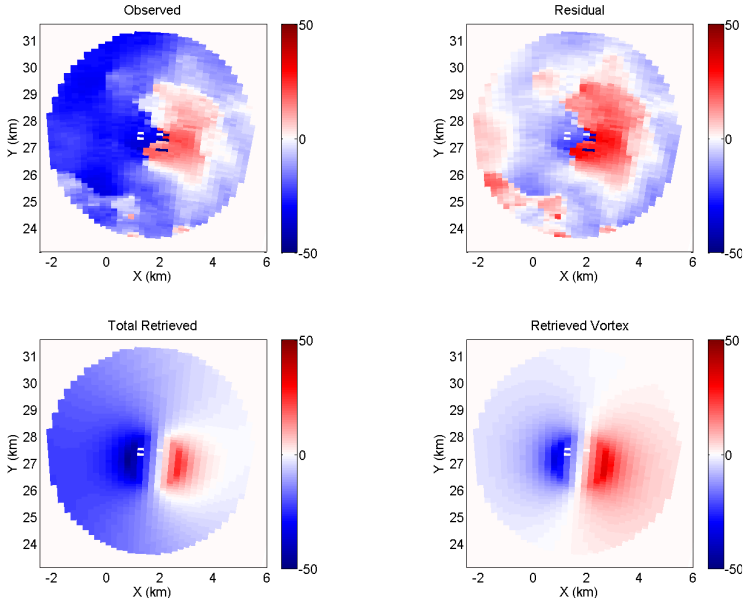

(b)

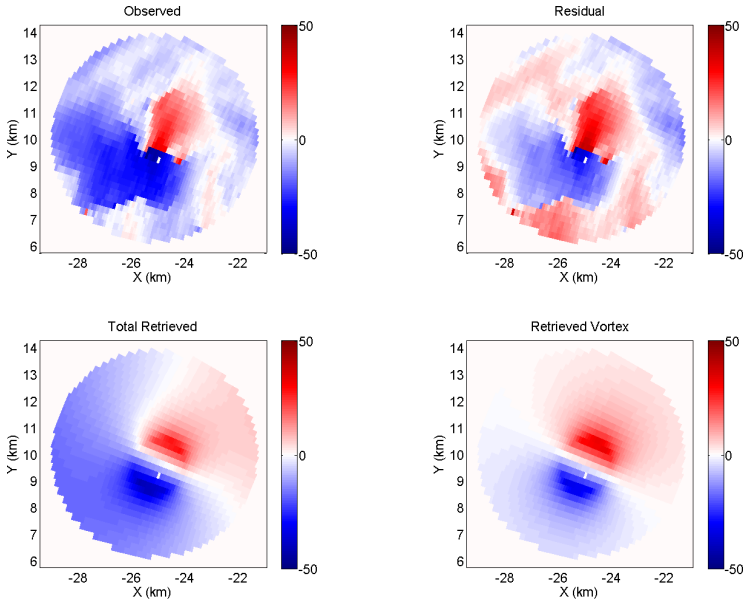

Figure 4.28. Same as Fig. 4.27 except at 0233 Z.

(a)

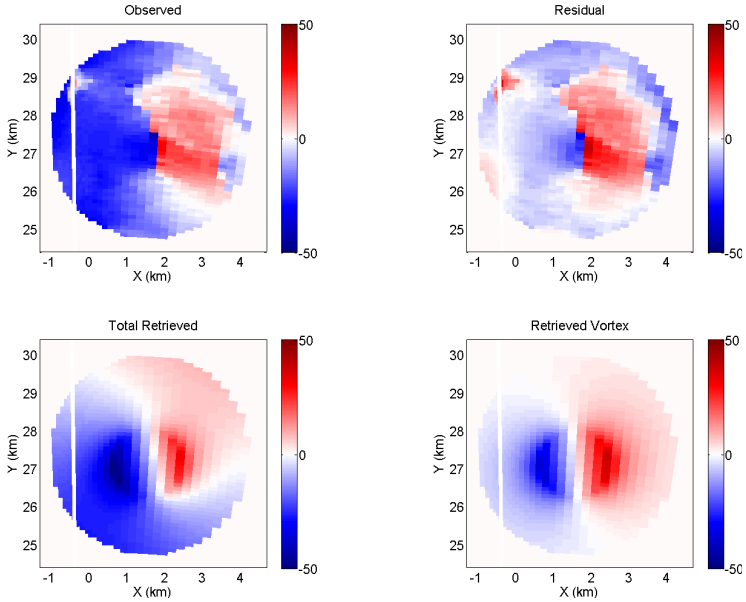

(b)

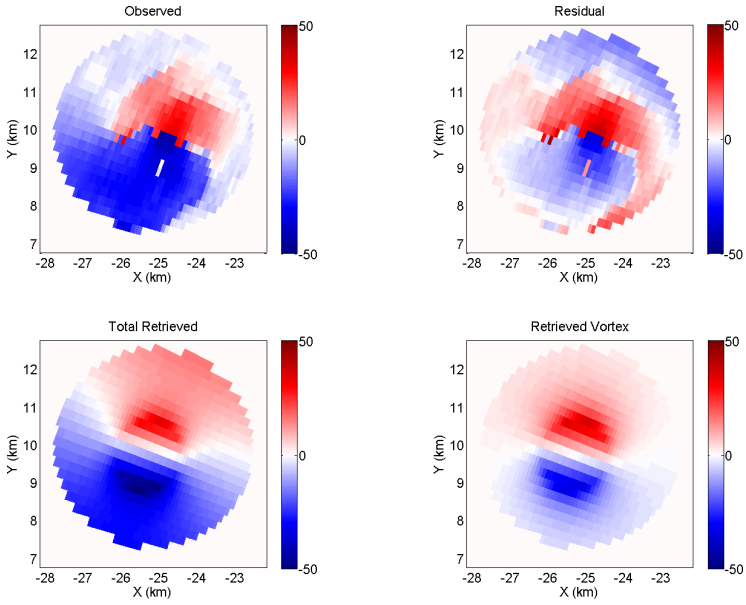

Figure 4.29. Same as Fig. 4.27 except at 0234 Z.

(a)

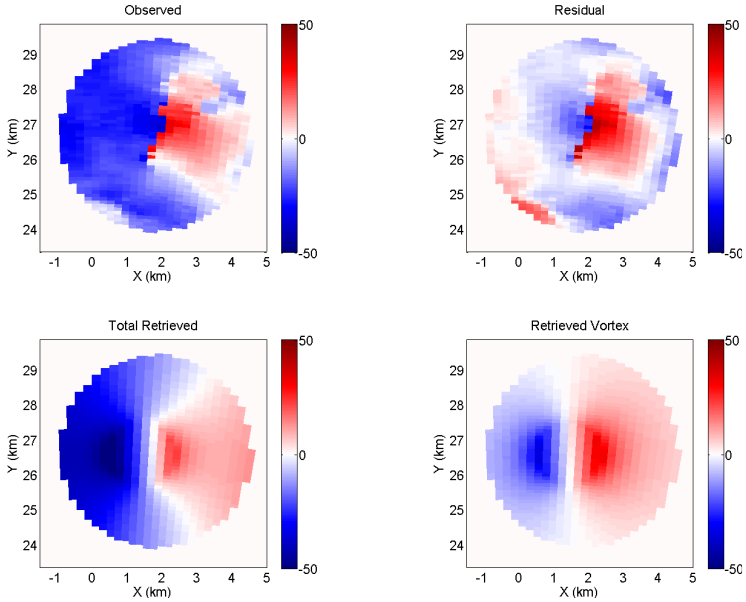

(b)

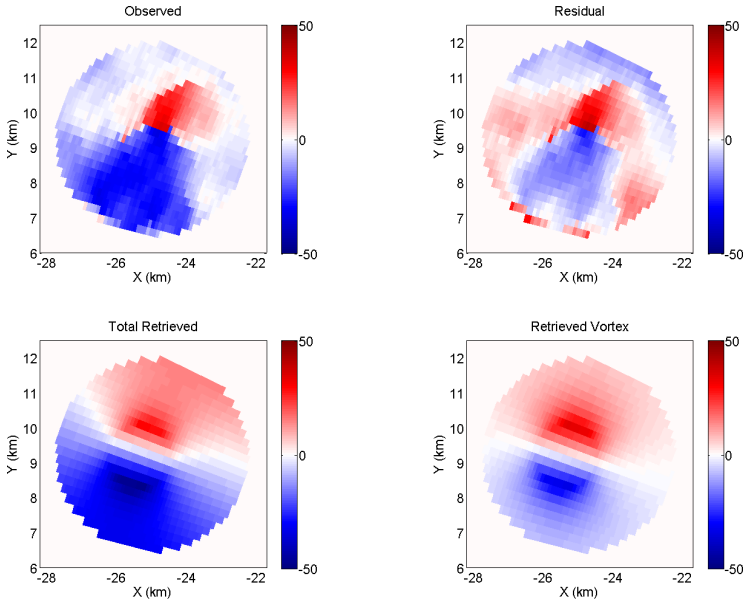

Figure 4.30. Same as Fig. 4.4 except for mesocyclone-mode retrievals.

(a)

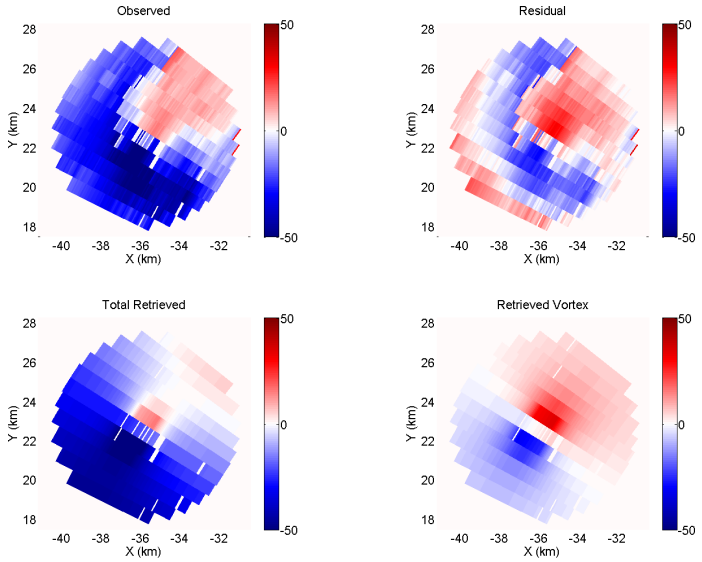

(b)

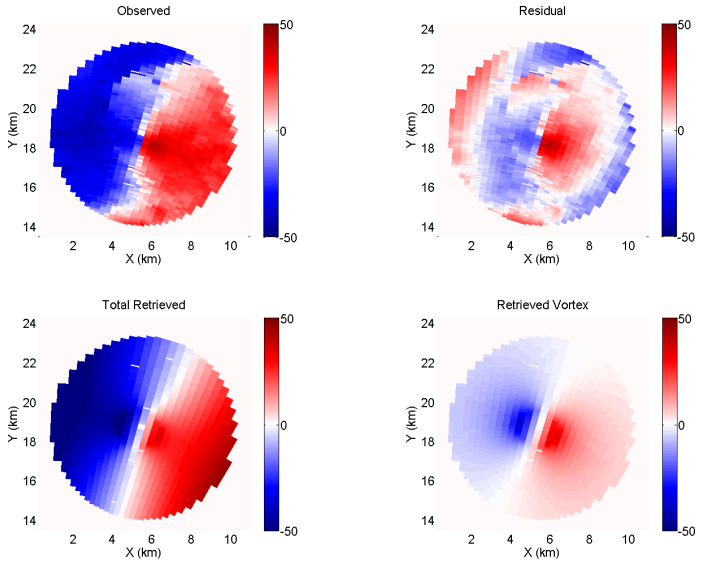

Figure 4.31. Same as Fig. 4.30 except at 0038 Z.

(a)

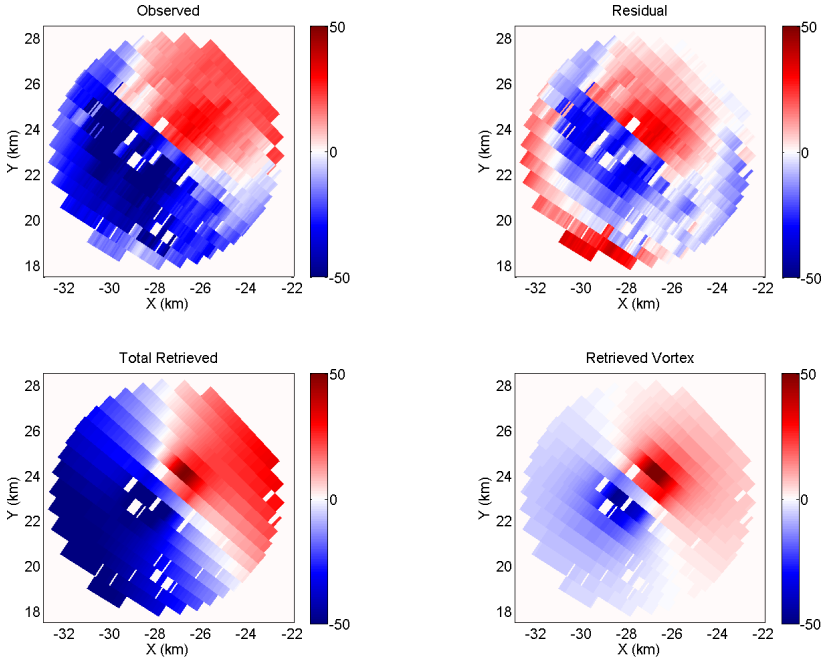

(b)

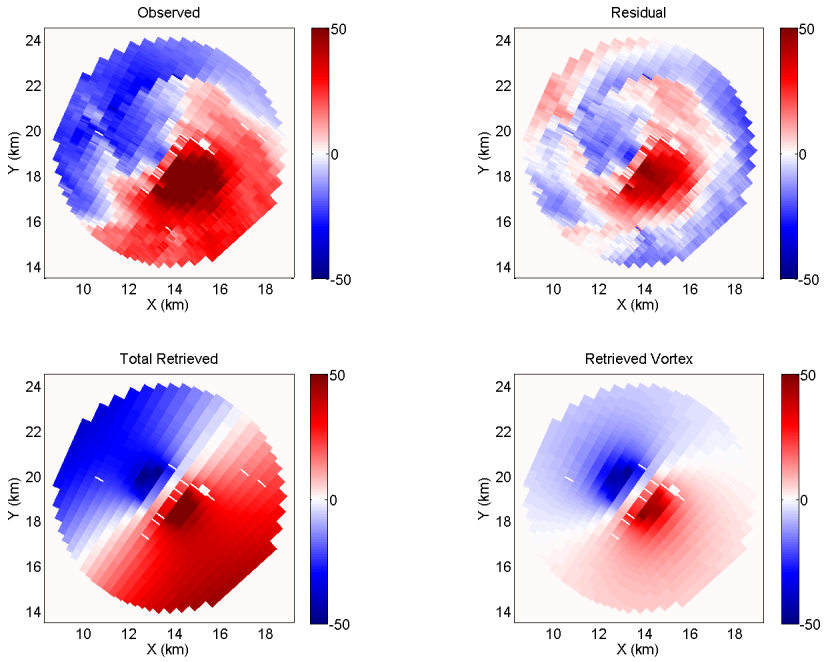

Figure 4.32. Same as Fig. 4.30 except at 0052 Z.

(a)

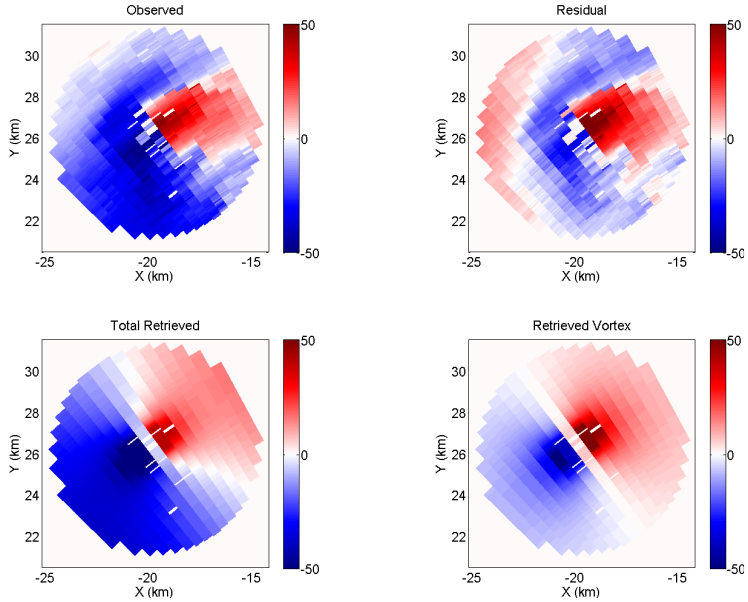

(b)

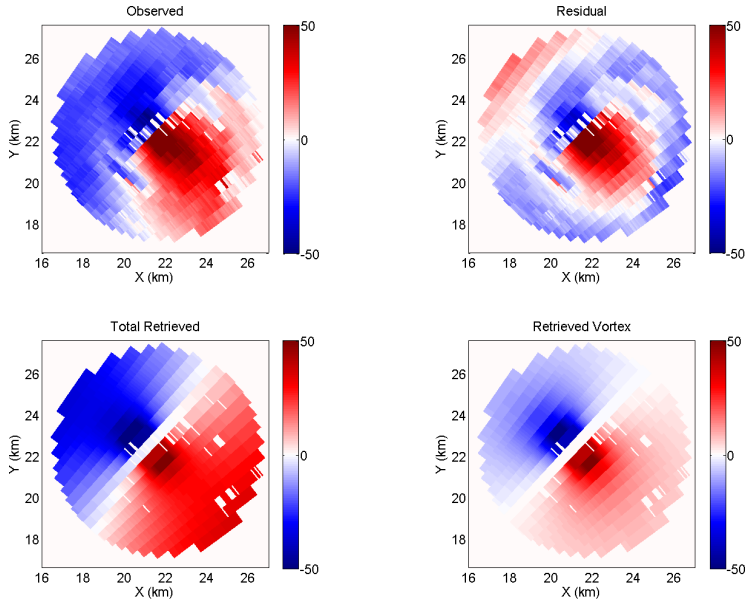

4.6.3 Single-Doppler Retrievals

Having established the appropriateness of the mesocyclone-mode retrieval methodology, the ability of the technique to detect and characterize larger-scale vortices in cases where only single-Doppler data are available was assessed. To do this, the mesocyclone retrievals described in Section 4.6.2 were repeated using data from one radar at a time. The only other modification to the experiments was (necessarily) to remove the requirement that the domain-selection criteria be satisfied by two radars.

The 29 May 2004 tornado was detected at all five times using the SR1 data and at four of the five times using the SR2 data (Tables 4.14 and 4.15). The failure of the 0022 Z SR2 retrievals to detect the mesocyclone is due (at least in part) to the highly complex radial wind field present at this time. In several instances, a highly convergent vortex was retrieved that provided a good match to a large portion of the wind field but not to the vortex itself (Fig. 4.33). Fortunately, no false detections occurred in these or the other retrievals. The retrieved vortex parameters generally did not change significantly from the dual-Doppler experiments, and the retrieved wind fields are still in reasonable agreement with the observations (Figs. 4.34-4.36). However, the mean retrieved V_T^{res} was significantly lower in both the SR2 and (especially) the SR1 0052 Z experiments, despite mean V_T values that were similar to that retrieved in the dual-Doppler 0052 Z experiment. This is because the angular separation criterion for a given V_T^{res} to be obtained (Section 2.5) is much more difficult to satisfy when data are available from only one radar, particularly if vortex winds of that magnitude are not well-resolved. The larger differences that occasionally occurred in the mean retrieved tornado center

between the dual- and single-Doppler experiments are perhaps not surprising given the complexity of the wind field.

Table 4.14. Same as Table 4.13 except for retrievals using data from SR1 only.

	Distance from dual-Doppler vortex center (m)	**V_T (m s^{-1})**	**V_T^{res} (m s^{-1})**	**V_R (m s^{-1})**	**R (m)**	**R_{20} (m)**	**α**
0022 Z (n=1)	282	40	25	-13	1170	2495	0.9
0027 Z (n=2)	218	36	20	-4	949	1555	1.2
0033 Z (n=8)	127	38	27	-21	945	1694	1.2
0038 Z (n=8)	341	49	23	1	1324	2168	1.9
0052 Z (n=7)	700	59	25	2	964	2830	1.0

Table 4.15. Same as Table 4.13 except for retrievals using data from SR2 only.

	Distance from dual-Doppler vortex center (m)	**V_T (m s^{-1})**	**V_T^{res} (m s^{-1})**	**V_R (m s^{-1})**	**R (m)**	**R_{20} (m)**	**α**
0022 Z (n=0)	N/A	N/A	N/A	N/A	N/A	N/A	N/A
0027 Z (n=3)	203	44	20	4	910	2308	1.0
0033 Z (n=6)	1357	55	30	-7	989	2731	1.2
0038 Z (n=8)	1317	53	20	3	1221	3824	0.9
0052 Z (n=4)	243	75	34	1	911	2802	1.2

Fortunately, the 14 May 2009 mesocyclone was detected in all of the single-Doppler experiments, and no false detections were made (Tables 4.16 and 4.17; Figs. 4.37-4.39). More detections were made by the KSAO retrievals, but this is only because more regions proximate to the mesocyclone satisfied the domain-selection criteria in the single-Doppler experiments (as expected). As with the 29 May 2004 experiments, the V_T^{res} are generally lower for the single-Doppler retrievals. The mean retrieved R and V_R in the dual-Doppler experiments appear to split the difference between the two sets of single-Doppler experiments, suggesting that both radars contributed useful velocity information to the dual-Doppler retrievals. This would make sense given that the two radars were roughly equidistant from the mesocyclone.

Table 4.16. Same as Table 4.12 except for retrievals using only data from KCYR.

	Distance from dual-Doppler vortex center (m)	**V_T (m s^{-1})**	**V_T^{res} (m s^{-1})**	**V_R (m s^{-1})**	**R (m)**	**R_{20} (m)**	**α**
0232 Z (n=2)	215	27	23	-1	1193	1444	1.7
0233 Z (n=3)	1234	37	20	0	1327	2027	1.3
0234 Z (n=1)	76	48	20	-4	1179	1921	1.8

Table 4.17. Same as Table 4.12 except for retrievals using only data from KSAO.

	Distance from dual-Doppler vortex center (m)	**V_T (m s^{-1})**	**V_T^{res} (m s^{-1})**	**V_R (m s^{-1})**	**R (m)**	**R_{20} (m)**	**α**
0232 Z (n=8)	212	53	28	-7	570	1847	0.9
0233 Z (n=4)	328	48	28	10	681	1464	1.7
0234 Z (n=9)	423	46	21	8	843	1897	1.0

Figure 4.33. Unsuccessful 0022 Z 29 May 2004 mesocyclone-mode retrieval using data from SR2 only.

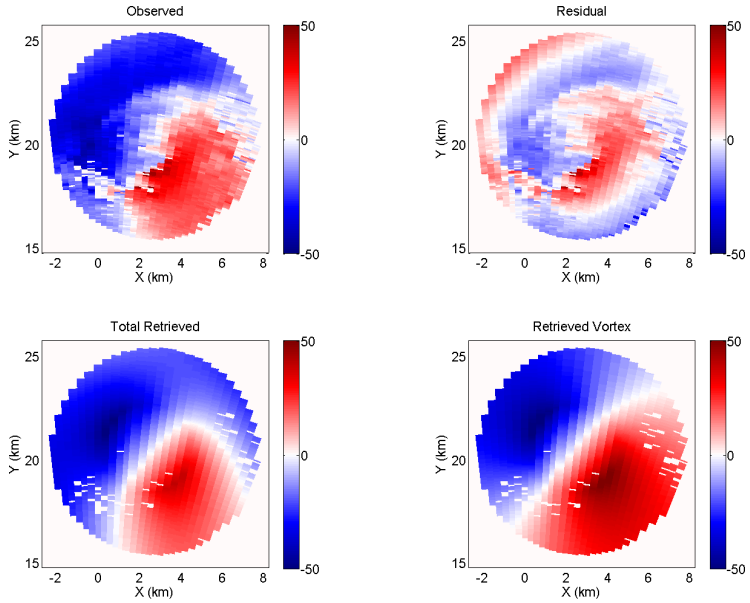

Figure 4.34. Same as Fig. 4.30 but for retrievals using data from SR1 only.

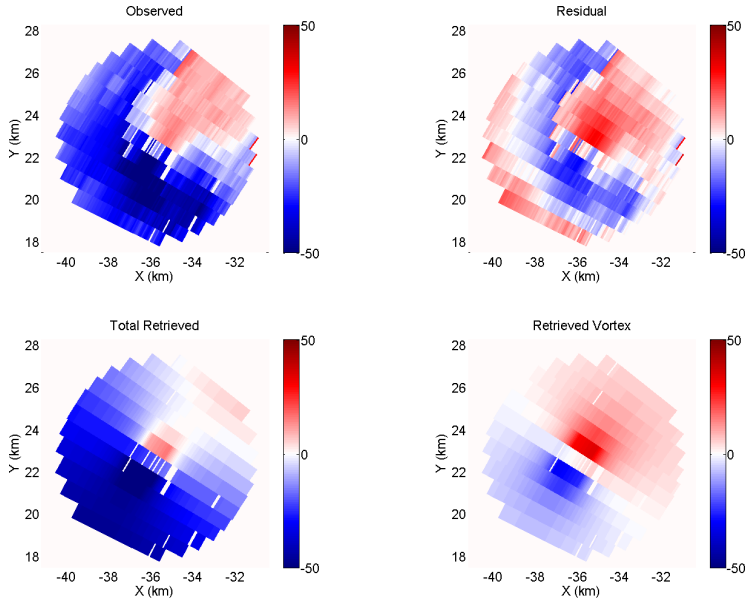

Figure 4.35. Same as Fig. 4.31 but for retrievals using data from SR1 only.

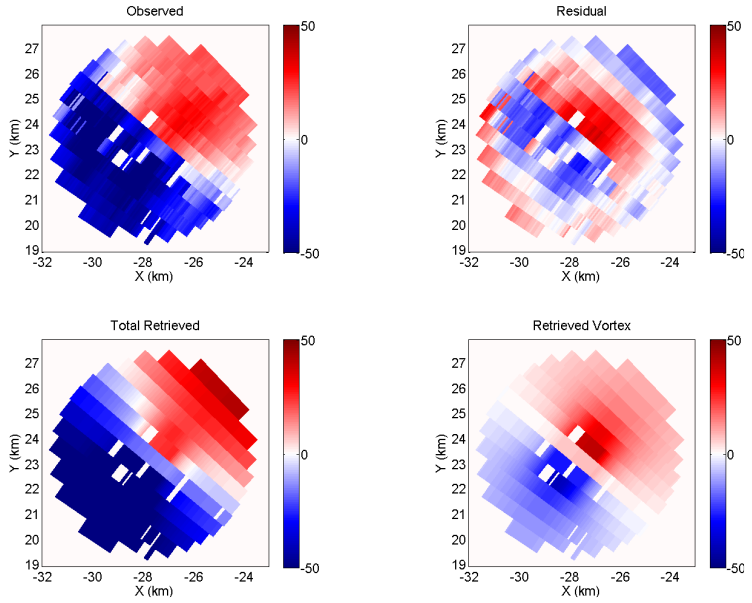

Figure 4.36. Same as Fig. 4.32 but for retrievals using data from SR1 only.

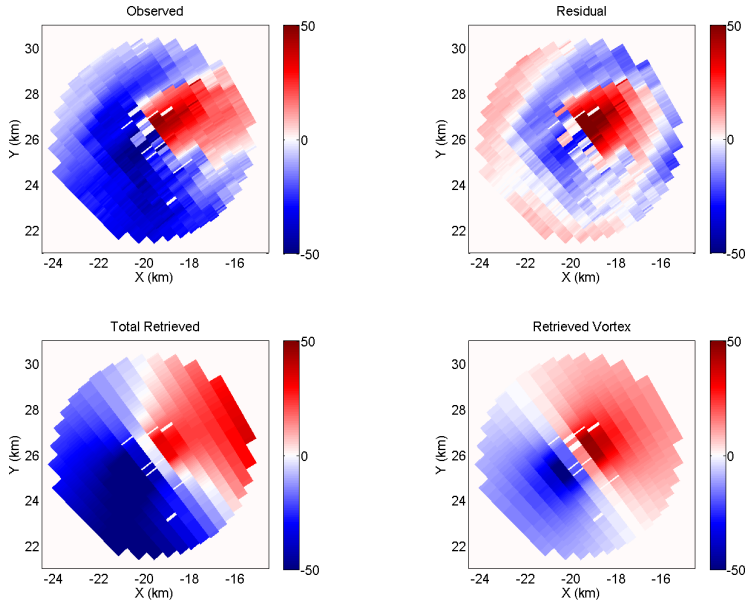

Figure 4.37. Same as Fig. 4.27 but for retrievals using data from KSAO only.

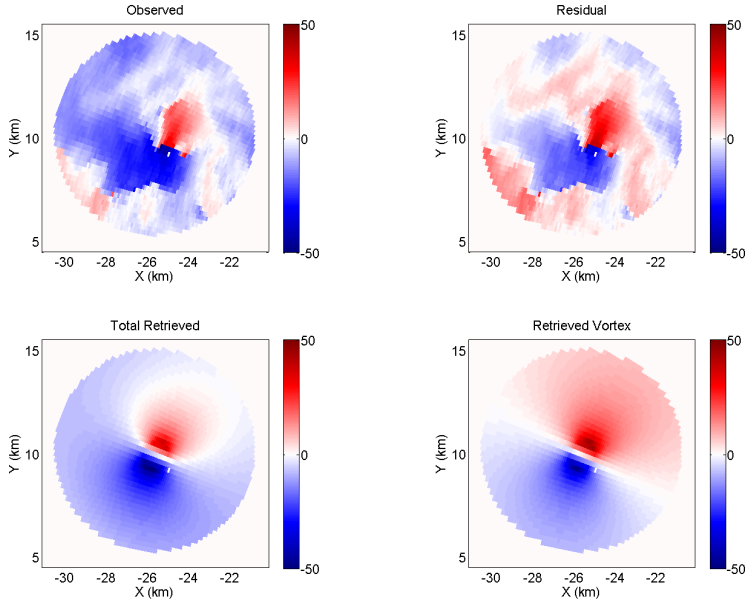

Figure 4.38. Same as Fig. 4.28 but for retrievals using data from KSAO only.

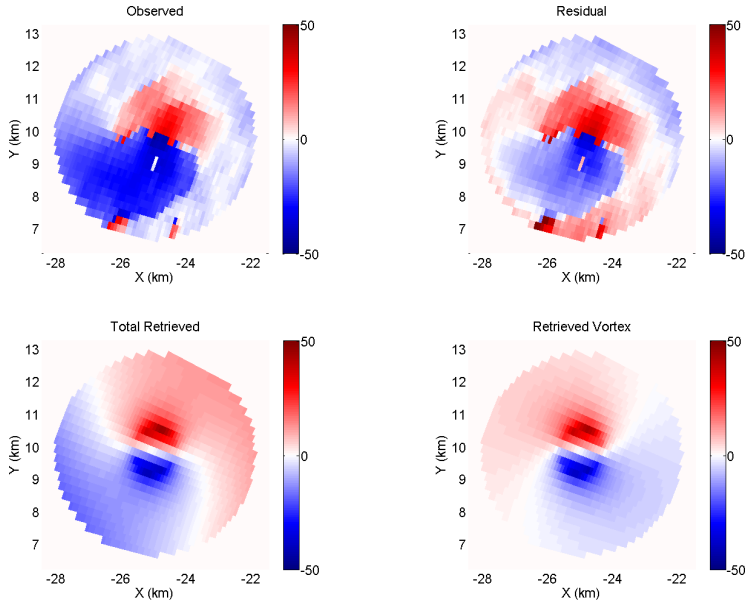

Figure 4.39. Same as Fig. 4.29 but for retrievals using data from KSAO only.

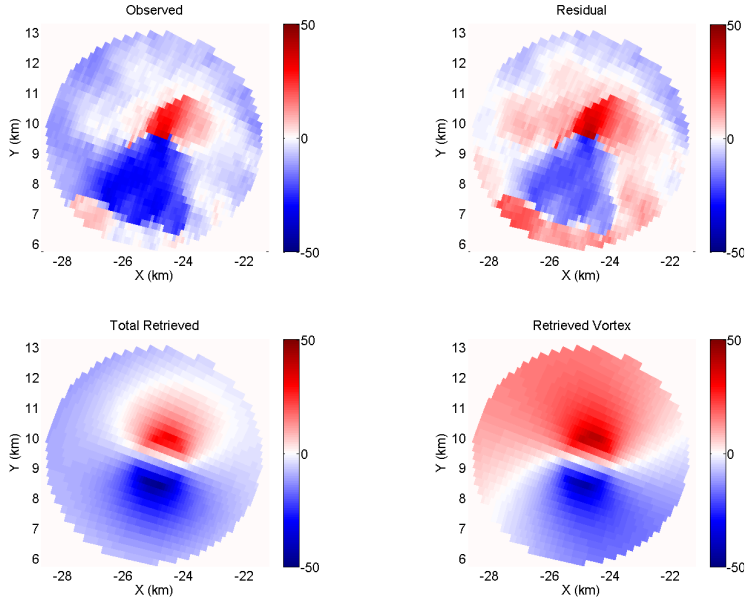

4.6.4 Discussion

The technique appears capable of detecting and characterizing larger-scale vortices such as mesocyclones, even when only single-Doppler data are available. It may therefore be appropriate to run the mesocyclone-retrieval configuration of the technique in real-time on WSR-88D data, at least for shorter radar ranges. This would greatly expand the domain over which the technique could be applied, thus leading to several possible research applications.

Correlating tornadogenesis potential to mesocyclone characteristics has been recognized as a worthwhile research endeavor, but one that requires an extensive dataset that must therefore be algorithmically generated (McGrath et al. 2002). Since this technique is equipped to detect both tornadoes and mesocyclones, it may serve as a valuable tool for the generation of such a mesocyclone-tornado climatology. Such a climatology could lead to the identification of important relationships between mesocyclone size/strength and tornado size/strength or probability of tornadogenesis. Such information would provide valuable guidance during severe weather operations.

Another potential application of the technique is the real-time detection and retrieval of the mesovortices often found in quasi-linear convective systems and commonly associated with severe surface winds. The resulting vortex climatologies could be valuable to the investigation of the relationships between mesovortices and the weak tornadoes often associated with them.

One modification to the vortex characterization criteria is now proposed. In cases where a retrieved vortex contains a smaller vortex whose observed wind field is stronger than that of the parent vortex, the V_T^{res} may actually be more representative of the smaller

vortex. This is because *all* radial wind observations within R_{det} of the retrieved vortex center are currently evaluated when determining V_T^{res}. In the case of large (relative to the observational resolution) vortices, it may therefore be more appropriate to exclude observations located within the vortex core but well away from the radius of maximum winds.

4.7 Sensitivity to First Guess Parameter Values

Experiments with analytically-generated wind fields showed that in cases where the vortex is well-resolved and the true wind field nearly satisfies the low-order model, the retrieved low-order model parameters are not unduly sensitive to their first guess values (Section 3.5.2). However, given that real wind fields are often associated with numerous minima in *J*, even when the vortex is well-resolved, it is possible that real-data retrievals will be particularly sensitive to the first guess wind field in some cases.

In order to preliminarily explore the sensitivity of the technique to the first guess when real wind fields are used, the 5 June 2001 Attica, KS retrievals (Section 4.3) were repeated at 0028 Z, 0031 Z and 0032 Z using different first guesses for the broadscale and/or vortex parameters (Table 4.18). Broadscale parameter first guesses were modified in steps 1 and 3 of the retrieval procedure (Section 2.5), and vortex parameter first guesses were modified in steps 2 and 4. The vortex center and translational velocity parameter first guesses were not varied since these are already determined by the domain-selection criteria and the Gal-Chen pattern translation retrieval, respectively.

Fortunately, using different first guesses for the broadscale parameters did not significantly impact the retrieval results at any of the three times (0028 Z results are

shown in Table 4.19). However, of the six experiments in which the vortex parameter first guesses were modified, the technique failed to detect the tornado in four of the 0028 Z experiments, all six of the 0031 Z experiments, and one of the 0032 Z experiments. In several of the 0028 Z experiments, the weaker, non-tornadic vortex was detected. In many of the retrievals in which no detection was made, the provisional vortex center left the analysis domain during the first few iterations of the minimization algorithm in step # 4 of the retrieval procedure. It therefore appears that initializing the model vortex with a non-zero wind field can lead to unsuitably large gradients of J with respect to the vortex center parameters (and perhaps other vortex parameters as well) unless countermeasures are taken.

The 0028 Z and 0031 Z experiments were therefore repeated upon halving the scaling factors applied to the vortex center parameters in the minimization procedure (Section 2.2) in order to reduce the sensitivity of the retrievals to these parameters. Surprisingly, the tornado was not detected in any of the new 0028 Z experiments, while the non-tornadic vortex was detected as many or more times in each of the new 0028 Z experiments as when the default vortex center parameter scaling factors were used. The tornado was detected in three of the six new 0031 Z experiments (Table 4.20). The larger numbers of detections in both sets of experiments suggest that the scaling of the vortex center parameters should be reduced if non-zero first guesses are used for either of the vortex wind parameters V_T and V_R. However, given that all of the experiments with modified vortex first guesses resulted in fewer tornado detections than in the original experiments, there is so far no apparent advantage to using non-zero first guesses for V_T and V_R in the first place.

The retrieved R and R_{10} indicate the larger vortex within which the tornado was embedded at 0031 Z was retrieved in the experiments with first guess R = 500 m, thus preventing the tornado itself from being detected. The use of the modifiable analysis domain evidently does not ensure that the smallest intense vortex is detected in cases where it is embedded within a larger vortex. The sensitivity to the first guess R in cases where a smaller vortex is embedded within a larger one suggests that the first guesses for the vortex radius as well as the vortex center should be varied in order to maximize the likelihood of detecting all intense vortices. Fortunately, this can be accomplished using the multiple retrieval configuration approach presented in Section 4.6. Sensitivity to the first guess R may also explain the failure of the technique to detect the tornado in most of the 0028 Z experiments. The non-tornadic vortex was only detected in experiments with first guess R=500 m, and the mean retrieved R and R_{10} in these cases were larger than in the experiments in which the tornado was detected. Using multiple retrieval configurations would likely be as helpful in such cases (spatially-separated vortices) as when one vortex is embedded within a larger vortex.

Table 4.18. Sets of first guess parameter values used in sensitivity tests with 5 June 2001 dual-DOW dataset. Broadscale parameter first guesses were modified in tests BS1 and BS2; vortex parameter first guesses were modified in tests V1, V2, V3 and V4; and both broadscale and vortex parameter first guesses were modified in tests BSV1 and BSV2. Asterisks denote values that are unchanged from their default values.

	default	**BS1**	**BS2**	**V1**	**V2**	**V3**	**V4**	**BSV1**	**BSV2**
a, d ($m\ s^{-1}$)	0	10	-10	*	*	*	*	10	-10
b, e (s^{-1})	0	.01	-.01	*	*	*	*	.01	-.01
c, f (s^{-1})	0	.01	-.01	*	*	*	*	.01	-.01
g, h (s^{-1})	0	.01	-.01	*	*	*	*	.01	-.01
u_b , v_b ($m\ s^{-1}$)	0	10	-10	*	*	*	*	10	-10
R (m)	200	*	*	500	50	500	50	500	50
V_R ($m\ s^{-1}$)	0	*	*	10	-10	*	*	10	-10
V_T ($m\ s^{-1}$)	0	*	*	*	*	20	-20	*	*
α, β	0.7	*	*	0.3	1.0	0.3	1.0	0.3	1.0

Table 4.19. Means of retrieved vortex characteristics for 0028 Z experiments using different sets of first guess model parameter values. Sample sizes (n) are given below each time. Italicized rows indicate groups of retrievals in which the non-tornadic vortex was retrieved.

	Distance from default mean vortex center (m)	**Movement Speed ($m\ s^{-1}$)**	**Heading (0° = east)**	**V_T ($m\ s^{-1}$)**	**V_T^{res} ($m\ s^{-1}$)**	**V_R ($m\ s^{-1}$)**	**R (m)**	**R_{10} (m)**	**α**
default (n=5)	-	10	-64	26	10	3	66	167	1.0
default *(n=1)*	-	*8*	*-58*	*18*	*10*	*6*	*174*	*333*	*0.9*
BS1 (n=4)	20	10	-65	26	10	1	58	162	0.9
BS2 (n=6)	6	10	-65	25	10	0	66	156	1.0
V1 *(n=8)*	*18*	*9*	*-57*	*15*	*10*	*4*	*287*	*391*	*1.1*
V2 (n=2)	41	9	-58	16	10	-5	76	147	0.9
V3 *(n=5)*	*56*	*12*	*-52*	*16*	*10*	*4*	*351*	*534*	*1.2*
V4 (n=0)	-	-	-	-	-	-	-	-	-
BSV1 (n=2)	29	10	-65	21	10	2	133	240	1.2
BSV1 *(n=5)*	*74*	*11*	*-65*	*15*	*10*	*4*	*290*	*416*	*1.1*
BSV2 (n=0)	-	-	-	-	-	-	-	-	-

Table 4.20. Means of retrieved vortex characteristics for 0031 Z first guess experiments using halved scaling factors for the vortex center parameters. Sample sizes (n) are given below each time.

	Distance from default mean vortex center (m)	**Movement Speed ($m\ s^{-1}$)**	**Heading (0° = east)**	**V_T ($m\ s^{-1}$)**	**V_T^{res} ($m\ s^{-1}$)**	**V_R ($m\ s^{-1}$)**	**R (m)**	**R_{10} (m)**	**α**
default (n=7)	-	11	-67	12	11	0	165	216	0.8
V1 (n=2)	165	12	-51	14	10	0	312	438	1.1
V2 (n=2)	99	18	-30	85	10	-4	35	334	0.7
V3 (n=6)	142	19	-35	15	10	0	299	427	1.2
V4 (n=0)	-	-	-	-	-	-	-	-	-
BSV1 (n=2)	103	14	-57	14	10	0	245	332	1.1
BSV2 (n=1)	69	22	-31	19	10	-4	238	495	0.9

4.8 Summary of Real Data Experiments

Testing the technique using real radar observations motivated several important modifications of the detection algorithm. First, in order to facilitate real-time operation of the algorithm, a set of selection criteria was developed to reduce the radar domain over which retrievals are performed. The technique was then modified to derive useful quantities such as V_T^{res} and R_{det} from the retrieved vortex model parameters. These derived vortex characteristics were shown to be less susceptible to the vortex solution non-uniqueness problem than the model parameters (e.g. R and V_T) themselves. Next, the technique was modified such that the locations and sizes of the analysis domains are

dynamically adjusted based on preliminary vortex retrievals. This step was found to be critical to the detection of smaller vortices. In order to reduce the false detection rate, especially in the presence of spurious velocity data, a threshold on radial velocity error was introduced to identify and reject retrievals which provide a poor match to the observed velocity field. Finally, a mesocyclone-retrieval configuration was added for the detection and characterization of larger vortices.

The results of the real-data tests were consistent with those of the OSSEs (Section 3) in several ways. The retrieved vortex parameters and wind fields were again generally consistent with the radial velocity observations, indicating that the low-order model, though a highly idealized representation of real convective wind fields, is complex enough to account for much of the radar-resolved flow structure in and near intense vortices, yet not so complex that the multiple minima problem becomes intractable. Also as in the OSSEs, using multiple first guess vortex centers significantly increased the probability of detecting all intense vortices in a given region, and subtracting the retrieved broadscale flow before retrieving the vortex facilitated the detection of vortices embedded within larger-scale vortices.

The real-data tests also illuminated both new weaknesses and capabilities of the technique. The 10 February 2009 experiments demonstrated the technique is capable of detecting and characterizing even "weak" (relative to tornadoes) vortices which may nevertheless be of scientific and operational interest (e.g. they may spawn or contract into tornadoes). However, these and the 14 May 2009 experiments also showed that extensive velocity contamination can prevent important vortices from being retrieved. The results of the single-Doppler mesocyclone-mode experiments suggest the technique

may be capable of detecting and characterizing larger vortices such as mesocyclones in traditional radar networks, thus extending its potential utility to non-CASA-like radar networks.

CHAPTER 5: REAL-TIME IMPLEMENTATION IN CASA RADAR NETWORKS

One of the most significant advantages of the CASA paradigm is the ability of the radars to dynamically adapt their scanning strategy to maximize temporal sampling of important weather features. This distributed collaborative adaptive sensing, or DCAS (McLaughlin et al. 2009), is driven by a group of weather detection and network control algorithms known as the Meteorological Command and Control (MCC; Junyent et al. 2010). The implementation of real-time vortex detection algorithms whose output help drive the DCAS is critical to ensuring that storms containing tornadoes, mesocyclones or mesovortices are scanned at high temporal resolution and (if possible) by multiple radars.

5.1 Optimizing POD, FAR and Computational Time

Successful real-time implementation of any detection technique requires the optimization of three competing variables: POD, FAR and computational time. In order for the presented technique to detect intense vortices in a timely manner, the wall clock time required for the algorithm to operate on the entire multiple-Doppler dataset collected by a single coordinated volume scan should not greatly exceed the volume scan time (60 s for the IP-1 network). However, significant reductions in computational cost may come at the expense of a lower POD. For example, using restrictive domain-selection criteria in order to minimize the number of retrievals performed could result in weaker/smaller tornadoes and mesocyclones being missed. On the other hand, using very loose criteria could delay the output of the algorithm to the point where it becomes irrelevant. In addition to the tradeoff between the POD and computational time, the inverse

relationship between POD and FAR must also be considered. Overly permissive detection criteria could result in an unacceptably high FAR, whereas overly restrictive detection criteria could result in an unacceptably low POD.

Modification of the technique to optimize the tradeoff between the POD, FAR and computational time in any given radar network will require an extensive period of real-time testing and will be largely determined by available computing resources, the sampling characteristics of the radars, the extent of velocity data contamination and aliasing, and the scales of the target vortices. Ideally, the domain-selection procedure and each set of wind retrievals (one set per identified domain) would be run independently of one another, preferably on separate processors. This would reduce the wall clock time of the algorithm by a factor nearly equal to the number of processors, potentially reducing the optimization problem to two variables (POD and FAR) if a sufficient number of processors are available.

There are many components of the technique that could be modified in order to optimize the tradeoffs discussed above. It has already been mentioned that the domain-selection and detection criteria can be made more or less restrictive. For example, both sets of criteria could require that a collocated storm cell be detected by a separate algorithm in the MCC, such as the Storm Cell Identification and Tracking (SCIT) algorithm currently used in IP-1. A larger first guess vortex center grid could be used to increase the POD, but at the expense of greater computational time. Conversely, computational time could be reduced at the expense of the POD by relaxing the convergence criteria in the minimization procedure.

So far, consideration has only been given to vortices within single- or dual-Doppler domains, in which case each of the observing radars contributes data to the domain-selection criteria and velocity retrievals. However, volume scans from three or more radars can overlap within CASA-like networks. In these regions, the domain-selection procedure could be made more or less restrictive by requiring that the criteria be satisfied by all the radars or by at least one pair of radars, respectively. In cases where the wind field is retrieved within an analysis domain observed by three or more radars, options include using data from (1) all the radars simultaneously, (2) one pair of radars at a time, or (3) only the radar pair objectively determined (based on cross-beam angle, radar-vortex ranges, extent of missing data near the vortex and radar sampling characteristics) to best resolve the wind field. Option # 1 is the most susceptible to velocity contamination if real-time filtering is not used, but otherwise may tend to produce more accurate ensemble mean vortex characteristic estimates than option # 2. (The lack of a triple-Doppler vortex dataset has thus far prevented evaluation of the value added by more than two radars. However, it is suspected that the improvement in the wind retrievals would be marginal in most cases.) Option # 2 is the most computationally expensive but should tend to produce the best POD in cases where velocity data contamination is widespread. Option # 3 would likely produce a lower POD than option # 2, especially when velocity contamination is widespread, but would also be less computationally expensive and would (presumably) produce more accurate vortex characteristic estimates. Again, extensive testing would be required to determine which of these options is most suitable for a given radar network.

5.2 Role in Adaptive Scanning

Once the technique is configured to produce acceptable values of POD and FAR in a timely fashion on a CASA-like radar network, it must then be determined what roles the output of the technique will play in driving the DCAS. Figure 5.1 illustrates one possible configuration. There are two types of output from the technique: regions identified as possibly containing intense vortices, and the vortex detections themselves. As mentioned above, the two corresponding components of the algorithm ought to run concurrently. Output from the domain-selection procedure would then be allowed to direct the radar task generator to give greater priority to sector-scanning regions (with two or more radars) identified as possibly containing intense vortices. This would increase the probability that any intense vortices present in those areas are retrieved and detected. Regions in which vortex detections are made would then be assigned still higher observational priority to help ensure that vortex locations and characteristics are continuously tracked over time. Since multiple simultaneous vortex detections may occur during severe weather outbreaks, a vortex ranking system would be required to help ensure the most threatening vortices receive greatest sector-scanning priority. Factors that should be incorporated in such a ranking system include the mean altitude of the analysis domain within which the detection(s) is (are) made (since lower-level detections are more likely to be tornadoes or potential tornado parent cyclones), the mean V_T^{res}, and the number of detections.

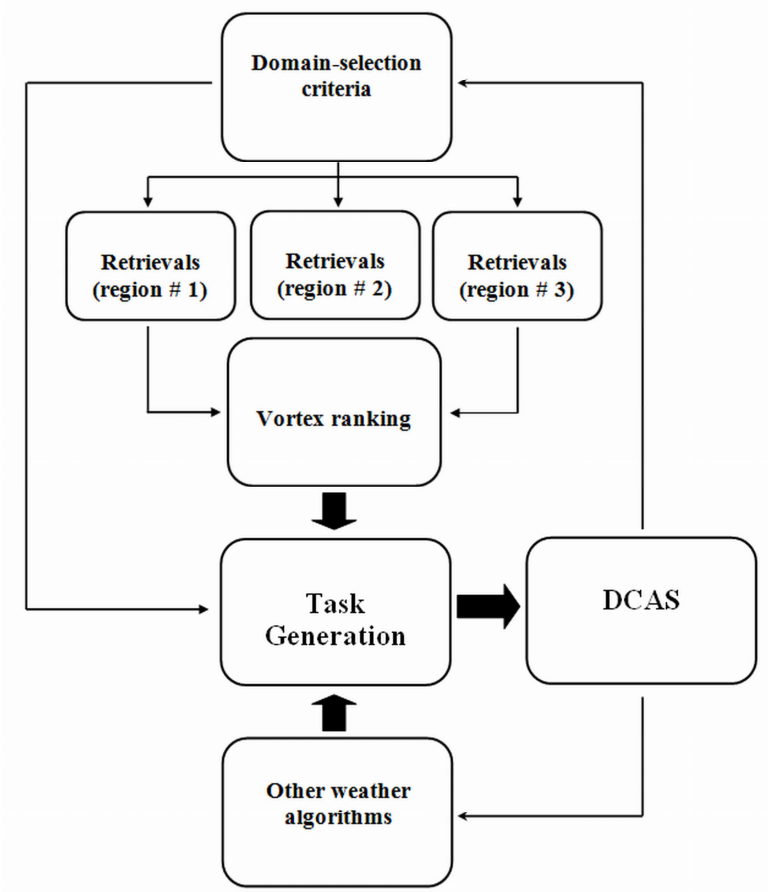

Figure 5.1. Depiction of one possible set of relationships between the vortex detection algorithm and the rest of the MCC.

5.3 Vortex Translation Estimation

The algorithm was configured to use a single pair of scans (one scan per radar) in the real-data experiments presented in Section 4. Due to the small temporal increments between radar scans from the same coordinated volume scan in these experiments, the vortex translational velocity was often poorly retrieved. One obvious potential solution to this problem is to use velocity data from two consecutive volume scans in order to increase the displacement of the vortex center over the course of the analysis window. Unfortunately, this solution would itself produce several new problems, the consequences

of which would generally outweigh the value of the improved translation velocity estimates. Perhaps the most serious consequence of requiring data from consecutive volume scans to perform a single retrieval is that the detection of new vortices would often be delayed. This is because a vortex that appears intense in one volume scan but weak in the previous volume scan (due to rapid intensification and/or increasingly favorable radar sampling) may be retrieved as a weak vortex and therefore undetected. In addition, using more radar scans in the retrieval increases the potential for spurious minima associated with contaminated velocity data. This in turn increases the FAR and decreases the POD.

Fortunately, the use of multiple volume scans in a single retrieval is not required to derive accurate vortex translational velocity estimates. In cases where the vortex center is well-retrieved at two consecutive analysis times (a necessary condition for accurate translational velocity estimation by any method), the translational velocity can simply be computed by dividing the vortex displacement by the difference in analysis times. This approach avoids the temporal "smearing" of the vortex associated with using data valid over a longer duration in a single retrieval and the associated time lag in the retrieved vortex characteristics.

In networks where radars can be directed to scan the same atmospheric volume nearly simultaneously (within a few seconds of one another), it may be advantageous to use a time-independent low-order model in which the broadscale and vortex translational velocity parameters are removed. Omission of these four parameters would speed up the convergence of the minimization algorithm, particularly in cases where these parameters are poorly determined (Sections 3.5.3, 3.5.4).

5.4 Velocity Contamination and Aliasing

In radar networks where velocity contamination is widespread, this technique (and all other velocity-based detection techniques) will be rendered ineffective unless real-time filtering is applied. Similarly, in cases where radial wind speeds exceed the Nyquist velocity of the radar and are not automatically corrected, velocity observations may be highly unrepresentative of the true atmospheric flow, thus defeating the technique. For example, isolated aliased velocities will produce spurious velocity couplets similar to those seen in the experiments with IP-1 data. In addition to causing false detections, the spurious couplets could also introduce minima in J that may prevent minima associated with real vortices from being detected by the minimization procedure. Unfortunately, the potential for velocity aliasing is often significant near severe thunderstorms and tornadoes, and severely aliased wind fields may not be amenable to objective unfolding techniques.

The normalized rms velocity error threshold included in the detection criteria seems to eliminate most false detections, whereas minima in J created by spurious velocities can prevent real vortices from being detected. Thus, most of the impact of spurious velocity data appears to be on the POD. Conversely, the FAR for shear-based detection methods typically increases significantly in the presence of spurious velocities, whereas the detection of true vortices is only threatened when bad velocities occur in or near the vortex circulation.

CHAPTER 6: SUMMARY AND CONCLUSIONS

A new multiple-Doppler technique for the detection and characterization of intense vortices has been developed and tested. The technique utilizes the dense, overlapping Doppler velocity coverage provided by CASA-like radar networks to retrieve important vortex characteristics such as location, size and strength. These characteristics are determined by least-squares fitting the radial wind observations to a low-order model which consists of a broadscale flow (linear shear, linear divergence and a constant velocity field) and modified combined Rankine vortex.

The greatest challenge to the technique is the existence of multiple minima in the cost function that accounts for the discrepancy between the observed and model radial wind fields. These minima result from edge effects (missing data and the bounded analysis domain), velocity data contamination, highly elliptical regions of the cost function surface (solution non-uniqueness), and violations of the idealized low-order model. The detrimental effects of each of these kinds of mimima have been mitigated to varying degrees through modifications to the retrieval procedure and detection criteria.

Experiments with analytical, numerically-simulated and real dual-Doppler observations of intense vortices indicate the technique is capable of retrieving radar-grid-scale features of the observed wind field reasonably well, including the radius of maximum wind and maximum tangential wind in cases where the vortex is well-resolved. In cases where the vortex core is not resolved, but other operationally-useful parameters can be resolved (e.g. radius of 25 m s^{-1} winds), these features are reliably retrieved. The vortex characteristic estimates output by the technique may benefit severe thunderstorm and tornado warning operations and provide vortex climatologies which advance our

understanding of the relationships between tornado size, strength and genesis and the size and strength of tornado parent vortices (low- and mid-level mesocyclones and mesovortices).

Widespread velocity contamination, if present in the data, poses a serious threat to the success of this technique. This is primarily because spurious velocities can prevent nearby vortices from being retrieved. Extensive testing will be required to determine whether the POD of the new technique is competitive with that of other techniques when bad data occur near the vortex. Fortunately, it does not appear that spurious velocity data significantly increase the FAR of this technique. Moreover, the new technique is likely subject to a more acceptable FAR-POD tradeoff (in cases where spurious velocities do not prevent the vortex from being retrieved) than single-Doppler detection methods since the detection criteria make use of a greater number of data points. It is therefore expected that the POD of the new technique will be higher than that of current techniques in cases where bad velocity data do not exist near the vortex, and that the FAR will be lower in general and especially when spurious velocities are present anywhere in the radar domain.

Real-time implementation of this technique within a CASA-like radar network requires extensive testing to optimize the tradeoffs between computational time, POD and FAR. If successful, the output of the technique could be used to help dynamically adapt the radars' scanning strategies so as to increase the probability of all intense vortices being detected throughout their lifetimes. The technique may also be useful for the detection and characterization of larger (> 1 km diameter) vortices in both CASA-like and conventional single-Doppler networks.

REFERENCES

Armijo, L., 1969: A theory for the determination of wind and precipitation velocities with Doppler radars. *J. Atmos. Sci*, **26**, 570–573.

Atkins, N.T., J.M. Arnott, R.W. Przybylinski, R.A. Wolf, and B.D. Ketcham, 2004: Vortex structure and evolution within bow echoes. Part I: Single-Doppler and damage analysis of the 29 June 1998 derecho. *Mon. Wea. Rev.*, **132**, 2224–2242.

Biggerstaff, M.I., L.J. Wicker, J. Guynes, C. Ziegler, J.M. Straka, E.N. Rasmussen, A. Doggett, L.D. Carey, J.L. Schroeder, and C. Weiss, 2005: The Shared Mobile Atmospheric Research and Teaching Radar: A collaboration to enhance research and teaching. *Bull. Amer. Meteor. Soc.*, **86**, 1263–1274.

Bluestein, H. B., W.-C. Lee, M. Bell, C. C. Weiss, and A. L. Pazmany, 2003: Mobile Doppler radar observations of a tornado in a supercell near Bassett, Nebraska, on 5 June 1999. Part II: Tornado-vortex structure. *Mon. Wea. Rev.,* **131**, 2968–2984.

Boccippio, D. J., 1995: A diagnostic analysis of the VVP single-Doppler retrieval technique. *J. Atmos. Oceanic Technol*., **12**, 230-248.

Box, G.E.P, and M.E. Muller, 1958: A note on the generation of random normal deviates. *Ann. Math. Stat*, **29**, 610-611.

Brandes, E.A., 1977: Gust front evolution and tornado genesis as viewed by Doppler radar. *J. Appl. Meteor.*, **16**, 333–338.

——, E., 1981: Fine structure of the Del City-Edmond tornadic mesocirculation. *Mon. Wea. Rev.*, **109**, 635-647.

——, E., 1984: Vertical vorticity generation and mesocyclone sustenance in tornadic thunderstorms: The observational evidence. *Mon. Wea. Rev*., **112**, 2253-2269.

Brotzge, J., and S. Erickson, 2010: Tornadoes without NWS warning. *Wea. Forecasting*, **25**, 159–172.

——, J., K. Hondl, B. Philips, L. Lemon, E.J. Bass, D. Rude, and D.L. Andra, 2010: Evaluation of distributed collaborative adaptive sensing for detection of low-level circulations and implications for severe weather warning operations. *Wea. Forecasting*, **25**, 173–189.

Browning, K. A., and R. Wexler, 1968: A determination of the kinematic properties of a wind field using Doppler radar. *J. Appl. Meteor*., **7**, 105–113.

Caton, P.A.F., 1963: Wind measurement by Doppler radar. *Meteor. Mag*., **92**, 213-222.

Caya, D., and I. Zawadzki, 1992: VAD analysis of nonlinear wind fields. *J. Atmos. Oceanic Technol*., **9**, 575-587.

——, S. Laroche, I. Zawadzki, and T. Montmerle, 2002: Using single-Doppler data to obtain a mesoscale environmental field. *J. Atmos. Oceanic. Technol*., **19**, 21-36.

Chong, M., and J. Testud, 1983: Three-dimensional wind field analysis from dual-Doppler radar data. Part III: The boundary condition: An optimum determination based on a variational concept. *J. Appl. Meteor.*, **22**, 1227–1241.

Diss, S., P. Arnaud, E. Moreau, and J. Lavabre, 2009: X-band radar coupled with a GR3H rain-flow model in mountainous areas for flood prediction. Preprints, *34th Conf. on Radar Meteorology*, Williamsburg, VA, Amer. Meteor. Soc.

Donner, K. M., 2007: High-resolution dual-Doppler analysis of two tornadic thunderstorms using a new formulation of advection correction. Master's thesis, School of Meteorology, University of Oklahoma, Norman, OK, 176 pp.

Doswell, C.A., H.E. Brooks, and M.P. Kay, 2005: Climatological estimates of daily local nontornadic severe thunderstorm probability for the United States. *Wea. Forecasting*, **20**, 577–595.

Easterbrook, C. C., 1975: Estimating horizontal wind fields by two dimensional curve fitting of single-Doppler radar measurements. Preprints, *16th Radar Meteorology Conf*., Houston, TX, Amer. Meteor. Soc., 214-219.

Fletcher, R., and C.M. Reeves, 1964: Function minimization by conjugate-gradients. *Computer J.,* **7**, 149-153.

Gal-Chen, T., 1982: Errors in fixed and moving frames of reference: Applications for conventional and Doppler radar analysis. *J. Atmos. Sci.*, **39**, 2279–2300.

Gamache, J . F., F. Roux, and F. D. Marks, 1991: Comparison of three methods to deduce three-dimensional wind fields in a hurricane with airborne Doppler radar. Preprints, *25th Int. Conf. on Radar Meteorology*, Paris, Amer. Meteor. Soc., 462-465.

Gao, J.-D., M. Xue, A. Shapiro, and K. K. Droegemeier, 1999: A variational method for the analysis of three-dimensional wind fields from two Doppler radars. *Mon. Wea. Rev.*, **127,** 2128-2142.

——, M. Xue, K. Brewster, and K. K. Droegemeier, 2004: A three-dimensional variational data analysis method with recursive filter for Doppler radars. *J. Atmos. Oceanic Technol*., **21**, 457-469.

Heymsfield, G.M., 1978: Kinematic and dynamic aspects of the Harrah tornadic storm analyzed from dual-Doppler radar data. *Mon. Wea. Rev.*, **106**, 233–254.

Junyent, F., V. Chandrasekar, D. McLaughlin, E. Insanic, and N. Bharadwaj, 2010: The CASA Integrated Project 1 networked radar system. *J. Atmos. Oceanic Technol.*, **27**, 61–78.

Kapitza, H., 1991: Numerical experiments with the adjoint of a non-hydrostatic mesoscale model. *Mon. Wea. Rev*., **119**, 2993-3011.

Lee, W.C., and F.D. Marks, 2000: Tropical cyclone kinematic structure retrieved from single-Doppler radar observations. Part II: The GBVTD-simplex center finding algorithm. *Mon. Wea. Rev.*, **128**, 1925–1936.

——, and J. Wurman, 2005: Diagnosed three-dimensional axisymmetric structure of the Mulhall tornado on 3 May 1999. *J. Atmos. Sci.*, **62**, 2373-2393.

——, F. D. Marks, Jr., and R. E. Carbone, 1994: Velocity Track Display – A technique to extract real-time tropical cyclone circulations using a single airborne Doppler radar. *J. Atmos. Oceanic Technol.*, **11**, 337–356.

——, J.-D. Jou, P.-L. Chang, and S.-M. Deng, 1999: Tropical cyclone kinematic structure retrieved from single Doppler radar observations. Part I: Interpretation of Doppler velocity patterns and the GBVTD technique. *Mon. Wea. Rev.,* **127**, 2419-2439.

Lhermitte, R. M., and D. Atlas, 1962: Precipitation motion by pulse Doppler. Preprints, *Ninth Weather Radar Conf*., Kansas City, MO, Amer. Meteor. Soc., 218-223.

Liou, Y.-C., T.-C. Chen Wang, W.-C. Lee, and Y.-J. Chang, 2006: The retrieval of asymmetric tropical cyclone structures using Doppler radar simulations and observations with the Extended GBVTD technique. *Mon. Wea. Rev.*, **134**, 1140-1160.

Liu, S., M. Xue, and Q. Xu, 2007: Using wavelet analysis to detect tornadoes from Doppler radar radial-velocity observations. *J. Atmos. Ocean Tech.*, **24,** 344-359.

Lugt, H. J., 1979: The dilemma of defining a vortex. *Recent Developments in Theoretical and Experimental Fluid Mechanics*, U. Mueller, K. G. Riesner and B. Schmidt, Eds., Springer-Verlag, 309–321.

Maddox, R. A., Zhang, J., Gourley, J. J., and Howard, K. W., 2002: Weather radar coverage over the contiguous United States. *Wea. Forecasting*, **17**, 927-934.

Maesaka, T., Maki, M., Iwanami, K., Misumi, R., and Shimizu, S., 2007: Real-time wind field retrieval system by using X-band radar network around Tokyo metropolitan

area. Preprints, *33rd Radar Meteorology Conf.*, Cairns, Australia. Amer. Metr. Soc.

Markowski, P., E. Rasmussen, J. Straka, R. Davies-Jones, Y. Richardson, and R.J. Trapp, 2008: Vortex lines within low-level mesocyclones obtained from pseudo-dual-Doppler radar observations. *Mon. Wea. Rev.*, **136**, 3513–3535.

Marks, F. D., and R. A. Houze, 1984: Airborne Doppler radar observations in Hurricane Debby. *Bull. Amer. Meteor. Soc.,* **65**, 569–582.

Marzban, C. and G. J. Stumpf, 1996: A neural network for tornado prediction based on Doppler radar-derived attributes. *J. Appl. Meteor.*, **35**, 617–626.

McGrath, K.M., T.A. Jones, and J.T. Snow, 2002: Increasing the usefulness of a mesocyclone climatology. Preprints, *21st Conf. on Severe Local Storms*, San Antonio, Texas. Amer. Meteor. Soc.

McLaughlin, D., and Coauthors, 2009: Short-wavelength technology and the potential for distributed networks of small radar systems. *Bull. Amer. Meteor. Soc*., **90**, 1797–1817.

Mewes, J. J., and A. Shapiro, 2002: Use of the vorticity equation in dual-Doppler analysis of the vertical velocity field. *J. Atmos. Oceanic Technol*., **19**, 543–567.

Mitchell, E. D., 1995: An enhanced NSSL tornado detection algorithm. Preprints, *27th Conf. on Radar Meteorology*, Vail, CO, Amer. Meteor. Soc., 406–408.

——, Vasiloff, S. V., Stumpf, J. G., Witt, A., Eilts, M. D., Johnson, J. T., and K. W. Thomas, 1998: The National Severe Storms Laboratory Tornado Detection Algorithm. *Wea. Forecasting*, **13**, 352–366.

Moeng, C.-H. and J. C. Wyngaard, 1989: Evaluation of turbulent transport and dissipation closures in second-order modeling. *J. Atmos. Sci.,* **46**, 2311-2330.

NOAA, NWS Budgets Set for FY 04. NOAA's NWS Focus February 10, 2004, National Weather Service, nws.noaa.gov, accessed May 2006.

National Climatic Data Center, cited 2010a: Storm Events Database. [Available online at http://www4.ncdc.noaa.gov/cgi-win/wwcgi.dll?wwevent~ShowEvent~511468.]

National Climatic Data Center, cited 2010b: Storm Events Database. [Available online at http://www4.ncdc.noaa.gov/cgi-win/wwcgi.dll?wwevent~ShowEvent~551065.]

National Climatic Data Center, cited 2010c: Storm Events Database. [Available online at http://www4.ncdc.noaa.gov/cgi-win/wwcgi.dll?wwevent~ShowEvent~.]

National Climatic Data Center, cited 2010d: Storm Events Database. [Available online at http://www4.ncdc.noaa.gov/cgiwin/wwcgi.dll?wwevent~ShowEvent~761954.]

National Weather Service, cited 2010: New Hail Criteria. [Available online at http://www.wrh.noaa.gov/psr/pns/2009/April/NewHailCriteria.php?wfo=psr.]

O'Brien, J. J., 1970: Alternative solutions to the classical vertical velocity problem. *J. Appl. Meteor*., **9**, 197–203.

Pedersen, L., N. E. Jensen, and H. Madsen, 2007: Network architecture for small X-band weather radars—Test bed for automatic inter-calibration and nowcasting. Preprints, *33rd Radar Meteorology Conf*., Cairns, Australia. Amer. Meteor. Soc.

Polak, E. And G. Ribiere, 1969: Note sur la convergence de methods de directions conjuguees. *Rev. Franc. Informat. Rech. Operationnelle*, **16**, 35-43.

Ray, P. S., R. J. Doviak, G. B. Walker, D. Sirmans, J. Carter, and B. Bumgarner, 1975: Dual-Doppler observations of a tornadic storm. *J. Appl. Meteor*., **14**, 1521–1530.

——, B. C. Johnson, K. W. Johnson, J. S. Bradberry, J. J. Stephens, K. K. Wagner, R. B. Wilhelmson, and J. B. Klemp, 1981: The morphology of several tornadic storms on 20 May 1977. *J. Atmos. Sci*., **38**, 1643-1663.

Rayleigh, Lord (J. W. Strutt), 1916: On the dynamics of revolving flows. *Proc. Roy. Soc. London*, **A93**, 148-154.

Rinehart, R. E., 1979: Internal storm motions from a single non-Doppler weather radar. NCAR/TN-146 + STR, 262 pp.

Roux, F., and F. D. Marks, 1996: Extended velocity track display (EVTD): An improved processing method for Doppler radar observations of tropical cyclones. *J. Atmos. Oceanic Technol.*, **13**, 875–899.

Shapiro, A. and J. Mewes, 1999: New formulations of dual-Doppler wind analysis. *J. Atmos. Oceanic Technol*., **16**, 782–792.

Smith, T. M., and K. L. Elmore, 2004: The use of radial velocity derivatives to diagnose rotation and divergence. Preprints, *11th Conf. on Aviation, Range and Aerospace*, Hyannis, MA, Amer. Meteor. Soc.

Stumpf, J. G., Witt, A., Mitchell, E. D., Spencer, P. L., Johnson, J. T., Eilts, M. D., Thomas, K. W., and D. W. Burgess, 1998: The National Severe Storms Laboratory Mesocyclone Detection Algorithm for the WSR-88D. *Wea. Forecasting*, **13**, 304-326.

Sun, J., and N. A. Crook, 1994: Wind and thermodynamic retrieval from single-Doppler measurements of a gust front observed during Phoenix II. *Mon. Wea. Rev.*, **122**, 1075–1091.

——, and ——, 1996: Comparison of thermodynamic retrieval by the adjoint method with the traditional retrieval method. *Mon. Wea. Rev.*, **124**, 308–324.

——, and ——, 2001: Real-time low-level wind and temperature analysis using single WSR-88D data. *Wea. Forecasting,* **16**, 117–132.

——, D. W. Flicker, and D. K. Lilly, 1991: Recovery of three-dimensional wind and temperature fields from simulated Doppler radar data. *J. Atmos. Sci.,* **48**, 876–890.

Taylor, G. I., 1938: The spectrum of turbulence. *Proc. Roy. Soc. London*, **A164**, 476–490.

Trapp, R.J., G.J. Stumpf, and K.L. Manross, 2005: A reassessment of the percentage of tornadic mesocyclones. *Wea. Forecasting*, **20**, 680–687.

Waldteufel, P., and H. Corbin, 1979: On the analysis of single Doppler radar data. *J. Appl. Meteor*., **18**, 532–542.

Wang, Y., T.Y. Yu, M. Yeary, A. Shapiro, S. Nemati, M. Foster, D.L. Andra, and M. Jain, 2008: Tornado detection using a neuro–fuzzy system to integrate shear and spectral signatures. *J. Atmos. Oceanic Technol.*, **25**, 1136–1148.

Wang, Z., K. K. Droegemeier, L. White, and I. M. Navon, 1997: Application of a new adjoint Newton algorithm to the 3D ARPS storm-scale model using simulated data. *Mon. Wea. Rev.,* **125**, 2460-2478.

Wicker, L. J., and R. B. Wilhelmson, 1995: Simulation and analysis of tornado development and decay within a three-dimensional supercell thunderstorm. *J. Atmos Sci*., **52**, 2675–2703.

Wood, V.T., D.C. Dowell, and R.A. Brown, 2004: Simulated WSR-88D measurements of a tornado having a weak reflectivity center. Preprints, *22nd Conf. on Severe Local Storms*, Hyannic, MA, Amer. Meteor. Soc.

Wurman, J., and S. Gill, 2000: Finescale radar observations of the Dimmitt, Texas (2 June 1995), tornado. *Mon. Wea. Rev*., **128**, 2135-2164.

——, and C. R. Alexander, 2005: The 30 May 1998 Spencer, South Dakota, Storm. Part II: Comparison of observed damage and radar-derived winds in the tornadoes. *Mon. Wea. Rev*., **133**, 97–119.

——, J. Straka, E. Rasmussen, M. Randall, and A. Zahrai, 1997: Design and deployment of a portable, pencil-beam, pulsed, 3-cm Doppler radar. *J. Atmos. Oceanic Technol*., **14**, 1502-1512.

——, Y. Richardson, C. Alexander, S. Weygandt, and P.-F. Zhang, 2007a: Dual-Doppler and single-Doppler analysis of a tornadic storm undergoing mergers and repeated tornadogenesis. *Mon. Wea. Rev*., **135**, 736–758.

——, Y. Richardson, C. Alexander, S. Weygandt, and P.-F. Zhang, 2007b: Dual-Doppler analysis of winds and vorticity budget terms near a tornado. *Mon. Wea. Rev*., **135**, 2392-2405.

Xue, M., K. K. Droegemeier, V. Wong, A. Shapiro, K. Brewster, F. Carr, D. Weber, Y. Liu, and D. Wang, 2001: The Advanced Regional Prediction System (ARPS) – A multi-scale nonhydrostatic atmospheric simulation and prediction tool. Part II: Model physics and applications. *Meteor. Atmos. Phys*., **76**, 143-165.

——, S. Liu, and T.Y. Yu, 2007: Variational analysis of oversampled dual-Doppler radial velocity data and application to the analysis of tornado circulations. *J. Atmos. Oceanic Technol.*, **24**, 403–414.

Zawadzki, I.I., 1973: Statistical properties of precipitation patterns. *J. Appl. Meteor*., **12**, 459-472.

APPENDIX: DERIVATION OF LOW-ORDER MODEL

The Cartesian components of the linear flow fields (broadscale flow) are given by

$$\begin{aligned} V_x &= a + b(y - v_t t) + c\,(x - u_t t) + gz, \\ V_y &= d + e(x - u_t t) + f\,(y - v_t t) + hz, \end{aligned} \tag{A1}$$

where a, d are constant flow components, b, e are shear parameters, c, f are divergence parameters, u_t, v_t are the translational velocity components of the broadscale fields, and t is time. It can be noted that (A1) implicitly makes provision for a broadscale vortex since the Cartesian representation of a solid body vortex is $u = -\Omega y,\ v = \Omega x,$ where Ω is the (constant) vortex angular velocity. This broadscale vortex description is independent of the small-scale vortex model to be described next.

In a local cylindrical coordinate system centered on and translating with the modified combined Rankine vortex, the azimuthal velocity field v_θ and radial velocity field v_r are given by:

$$v_\theta = \begin{cases} \dfrac{r}{R} V_T, & r < R, \\ \dfrac{R^\alpha}{r^\alpha} V_T, & r \geq R, \end{cases} \qquad v_r = \begin{cases} \dfrac{r}{R} V_R, & r < R, \\ \dfrac{R^\beta}{r^\beta} V_R, & r \geq R, \end{cases} \tag{A2}$$

where

$$r = \sqrt{(x - x_0 - u_v t)^2 + (y - y_0 - v_v t)^2}\ ,$$

is the distance of a given (x, y) coordinate from the center of the vortex at time t. The vortex is described by nine parameters: initial vortex center location (x_0, y_0), vortex translational velocity (u_v, v_v), radius of maximum wind R, maximum tangential velocity

V_T, maximum radial velocity V_R, and the radial decay rates α, β of the tangential and radial wind components. The model parameters are listed in Table 2.1.

To facilitate calculation of the radial (with respect to a radar) component of the model wind fields, the Cartesian components of the model wind fields are first obtained and then the radial component is extracted. Toward that end, the velocity **V** of the MCRV can be expressed in vortex-centered cylindrical coordinates (not radar coordinates) as the sum of its radial and tangential components, $\mathbf{V} = v_r \hat{r} + v_\theta \hat{\theta}$, where $\hat{r}$ and $\hat{\theta}$ are the unit vectors in the radial and azimuthal directions in the vortex cylindrical coordinate system, respectively. Figure A.1 depicts the relationship between the Cartesian and vortex coordinate systems. The Cartesian components of **V** are computed as:

$$u = \hat{i} \cdot \mathbf{V} = v_r \cos\theta - v_\theta \sin\theta, \quad v = \hat{j} \cdot \mathbf{V} = v_r \sin\theta + v_\theta \cos\theta \ . \tag{A3}$$

Formulae for $cos\theta$ and $sin\theta$ at arbitrary time t follow immediately from Fig. A.1:

$$\cos\theta = \frac{x - x_0 - u_v t}{r}, \qquad \sin\theta = \frac{y - y_0 - v_v t}{r}.$$

Substituting these into (A3) yields

$$u = \frac{x - x_0 - u_v t}{r} v_r - \frac{y - y_0 - v_v t}{r} v_\theta, \quad v = \frac{y - y_0 - v_v t}{r} v_r + \frac{x - x_0 - u_v t}{r} v_\theta.$$

Substituting for v_r, v_θ from (A2) and adding the linear flow fields (A1) produces the Cartesian representation of the full model wind field:

$$u = \begin{cases} a + b(y - v_t t) + c(x - u_t t) + gz + \dfrac{V_R}{R}(x - x_0 - u_v t) - \dfrac{V_T}{R}(y - y_0 - v_v t), & r < R, \\ a + b(y - v_t t) + c(x - u_t t) + hz + \dfrac{R^\beta V_R (x - x_0 - u_v t)}{r^{\beta+1}} - \dfrac{R^\alpha V_T (y - y_0 - v_v t)}{r^{\alpha+1}}, & r \geq R, \end{cases}$$

$$v = \begin{cases} v = d + e(x - u_t t) + f(y - v_t t) + gz + \dfrac{V_R}{R}(y - y_0 - v_v t) + \dfrac{V_T}{R}(x - x_0 - u_v t), & r < R, \\ \quad = d + e(x - u_t t) + f(y - v_t t) + hz + \dfrac{R^{\beta} V_R (y - y_0 - v_v t)}{r^{\beta+1}} + \dfrac{R^{\alpha} V_T (x - x_0 - u_v t)}{r^{\alpha+1}}, & r \geq R. \end{cases}$$

Finally, solving for the radial component of the total velocity yields the model Doppler radar velocity, V_r^{mod}:

$$V_r^{mod} = \begin{cases} \cos\phi_n \sin\theta_n \left[a + b(y - v_b t) + c(x - u_b t) + gz + \dfrac{V_R}{R}(x - x_0 - u_v t) - \dfrac{V_T}{R}(y - y_0 - v_v t) \right] + \\ \quad \cos\phi_n \cos\theta_n \left[d + e(x - u_b t) + f(y - v_b t) + hz + \dfrac{V_R}{R}(y - y_0 - v_v t) + \dfrac{V_T}{R}(x - x_0 - u_v t) \right] \\ \quad r < R, \\ = \cos\phi_n \sin\theta_n \left[a + b(y - v_b t) + c(x - u_b t) + gz + \dfrac{R^{\beta} V_R (x - x_0 - u_v t)}{r^{\beta+1}} - \dfrac{R^{\alpha} V_T (y - y_0 - v_v t)}{r^{\alpha+1}} \right] + \\ \quad \cos\phi_n \cos\theta_n \left[d + e(x - u_b t) + f(y - v_b t) + hz + \dfrac{R^{\beta} V_R (y - y_0 - v_v t)}{r^{\beta+1}} + \dfrac{R^{\alpha} V_T (x - x_0 - u_v t)}{r^{\alpha+1}} \right] \\ \quad r \geq R. \end{cases}$$

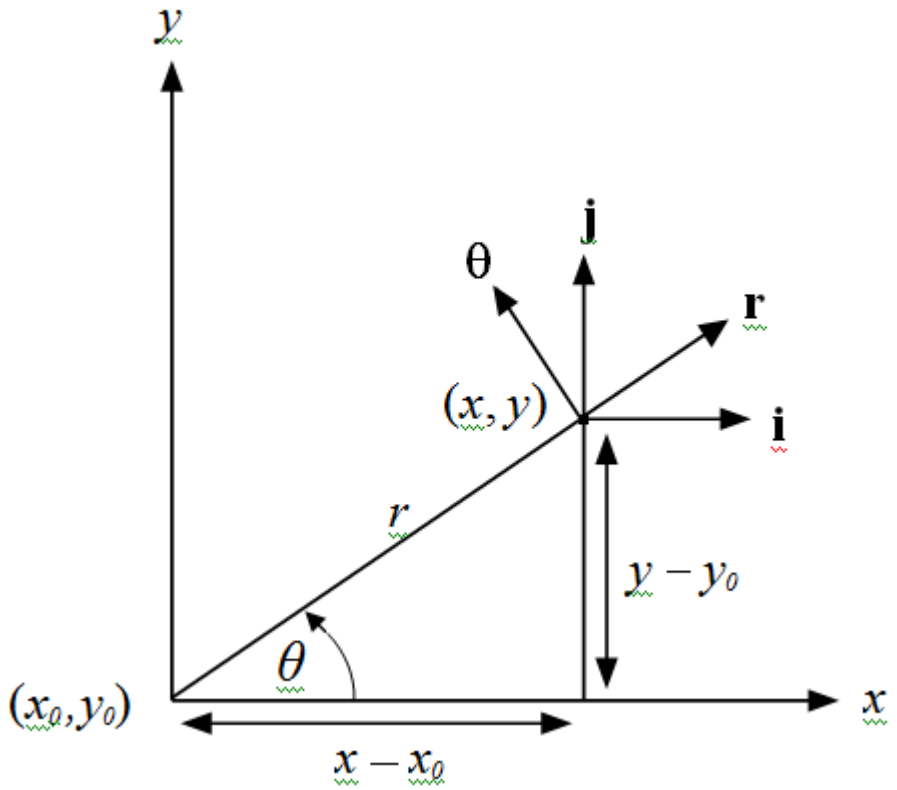

Figure A.1. Cartesian and cylindrical (vortex) coordinate systems defining model broadscale and vortex flows, respectively at $t = 0$. The vortex is initially located at x_0, y_0.